NANYANG TECHNOLOGICAL UNIVERSITY
SINGAPORE

DEVELOPMENT OF SCHLIEREN-IMAGE BASED FLOW DIAGNOSTICS AND ANALYSIS FOR SUPERSONIC JET FLOWS

LIM HAOXIANG DESMOND

SCHOOL OF MECHANICAL AND AEROSPACE ENGINEERING

2020

DEVELOPMENT OF SCHLIEREN-IMAGE BASED FLOW DIAGNOSTICS AND ANALYSIS FOR SUPERSONIC JET FLOWS

LIM HAOXIANG DESMOND

School of Mechanical and Aerospace Engineering

A thesis submitted to the Nanyang Technological University
in partial fulfilment of the requirement for the degree of
Doctor of Philosophy

2020

Statement of Originality

I hereby certify that the work embodied in this thesis is the result of original research, is free of plagiarised materials, and has not been submitted for a higher degree to any other University or Institution.

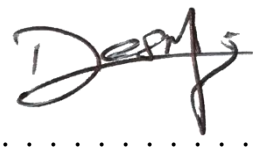

28 Dec 2019
. . . . . .
Date

. . . . . .
Lim Haoxiang Desmond

Supervisor Declaration Statement

I have reviewed the content and presentation style of this thesis and declare it is free of plagiarism and of sufficient grammatical clarity to be examined. To the best of my knowledge, the research and writing are those of the candidate except as acknowledged in the Author Attribution Statement. I confirm that the investigations were conducted in accord with the ethics policies and integrity standards of Nanyang Technological University and that the research data are presented honestly and without prejudice.

29 Dec 2019

. . . . . .

Date

. . . . . .

A/Prof New Tze How Daniel

Authorship Attribution Statement

This thesis contains material from 3 papers published / submitted and under review in the following peer-reviewed journals, 1 paper published in a book chapter and 3 papers accepted at conferences in which I am listed as an author.

Part of Chapter 4 is published in a peer-reviewed journal as:

Lim, H.D., New, T.H., Mariani, R., and Cui, Y.D., *Visual hull based 3D reconstruction of shocks in under-expanded supersonic bevelled jets*. Experimental Thermal and Fluid Science, 2018. 99: p. 458-473.

The contributions of the co-authors are as follows:

- A/Prof New Tze How Daniel provided the initial project direction and closely guided me throughout the entire study.
- I set up the supersonic jet apparatus with Dr Cui Yong Dong at Temasek Laboratories, National University of Singapore.
- I designed and performed the multi-view schlieren experiments and external camera calibration procedures.
- Dr Mariani Raffaello and Dr Cui Yong Dong assisted me in performing the schlieren experiments and the external camera calibration.
- I came up with the idea of using visual hull based techniques for 3D shock wave reconstruction and the algorithm was written by me.
- I developed and refined the semi-synthetic camera calibration technique and image post-processing procedures.

- I applied the 3D reconstruction technique to under-expanded supersonic bevelled jets and validated its accuracy with current 2D schlieren methods.
- I prepared the manuscript drafts. All authors contributed in the revisions.
- I prepared the revised manuscript requested by the reviewers. The revised manuscript was edited by A/Prof New Tze How Daniel.

Part of Chapter 4 is published in conference proceedings as:

Lim, H.D., New, T.H., and Cui, Y.D., *A semi-synthetic camera calibration method for 3D reconstruction of shocks in supersonic jets*, in *19th International Symposium on the Application of Laser and Imaging Techniques to Fluid Mechanics*. 2018: Lisbon, Portugal.

The contributions of the co-authors are as follows:

- A/Prof New Tze How Daniel provided the initial project direction and closely guided me throughout the entire study.
- I set up the supersonic jet apparatus with Dr Cui Yong Dong at Temasek Laboratories, National University of Singapore.
- I designed and performed the single-view schlieren experiment and external camera calibration procedures, assisted by Dr Cui Yong Dong.
- I developed the first version of the semi-synthetic camera calibration method.
- I developed the image post-processing procedures.
- I prepared the conference paper and presentation slides. All authors contributed in the revisions.

- I presented the paper in the conference.

Part of Chapter 5 is published in a peer-reviewed journal as:

Lim, H.D., New, T.H., Mariani, R. and Cui, Y.D., *Effects of bevelled nozzles on standoff shocks in supersonic impinging jets*. Aerospace Science and Technology, 2019. 94: p. 105371.

The contributions of the co-authors are as follows:

- A/Prof New Tze How Daniel provided the initial project direction and closely guided me throughout the entire study.
- I set up the supersonic jet apparatus with Dr Cui Yong Dong at Temasek Laboratories, National University of Singapore.
- A/Prof New Tze How Daniel designed the impingement plate.
- A/Prof New Tze How Daniel and I designed the experiment and formulated the research objective.
- I performed the schlieren experiments together with Dr Mariani Raffaello, assisted by Dr Cui Yong Dong.
- I post-processed the schlieren images and reconstructed the shock waves using the visual hull based 3D reconstruction technique. I analysed and interpreted the data with the help of A/Prof New Tze How Daniel.
- I prepared the manuscript drafts. All authors contributed in its subsequent revisions.

Part of Chapter 6 is published in a book chapter in:

Lim H.D., New T.H., Cui Y.D., Shi S., *Time-resolved optical flow of supersonic bevelled nozzles*. In 31st International Symposium on Shock Waves, pp. 337-344. Springer, Cham, 2017.

The same manuscript has been presented at the ISSW31 conference and received a student competition award, and is published in the conference proceedings as:
Lim, H.D., New, T.H., Cui, Y.D., and Shi, S., *Time-resolved optical flow of supersonic bevelled nozzles*, in *31st International Symposium on Shock Waves (ISSW31)*. 2017: Nagoya, Japan.

The contributions of the co-authors are as follows:

- A/Prof New Tze How Daniel and Prof Shi Shengxian provided the initial project direction and closely guided me throughout the entire study.
- I set up the supersonic jet apparatus with Dr Cui Yong Dong at Temasek Laboratories, National University of Singapore.
- I performed the ultrahigh-speed schlieren experiments, assisted by Dr Cui Yong Dong.
- I developed the optical flow algorithm and perform validation tests using synthetic data.
- I processed the time-resolved schlieren images with my optical flow algorithm.
- I interpret the results together with A/Prof New Tze How Daniel.

- I prepared the conference paper and presentation slides. All authors contributed in its subsequent revisions.
- I presented the paper in the conference.

Part of Chapter 6 is published in conference proceedings as:

Lim, H.D., Wu, J., Wei, X., New, T.H., Cui, Y.D., and Shi, S., *Challenges of optical flow analysis in supersonic jets*. in *55th AIAA Aerospace Sciences Meeting*. 2016. Grapevine, Texas, USA.

The contributions of the co-authors are as follows:

- A/Prof New Tze How Daniel and Prof Shi Shengxian provided the initial project direction and closely guided me throughout the entire study.
- I set up the supersonic jet apparatus with Dr Cui Yong Dong and Dr Wu Jie at Temasek Laboratories, National University of Singapore.
- I designed and experimented with the double-camera (and beamsplitter) Z-type schlieren setup.
- I performed the schlieren experiments and was assisted by Dr Wu Jie and Wei Xiaofeng.
- I performed numerical tests based on an open source optical flow algorithm and synthetic particle-image data, to assess the optimal performance of optical flow based on the image framing rate requirement.
- I prepared the conference paper and presentation slides. All authors contributed in its subsequent revisions.

- I presented the paper in the conference.

Part of Chapter 7 is under preparation for submission to a peer-reviewed journal as:

Lim, H.D., Wei, X.F., Zang, B., U S Vevek, Mariani, R., New, T.H. and Cui, Y.D., *Short-time proper orthogonal decomposition of time-resolved schlieren images for characterization of transient jet screech*.

The contributions of the co-authors are as follows:

- A/Prof New Tze How Daniel provided the initial project direction and closely guided me throughout the entire study.
- I set up the supersonic jet apparatus with Wei Xiaofeng and Dr Cui Yong Dong at Temasek Laboratories, National University of Singapore.
- Wei Xiaofeng designed the acoustic experimental setup with the help of A/Prof New Tze How Daniel, performed the acoustic measurements with the assistance of Dr Cui Yong Dong, and post-processed the results.
- I designed and performed the time-resolved schlieren experiments, assisted by Dr Mariani Raffaello and Dr Cui Yong Dong.
- I developed the time-resolved schlieren-based proper orthogonal decomposition algorithm (POD) with the help of Dr Zang Bin.
- I developed the signal processing algorithms to analyse the POD results.
- U S Vevek and Dr Zang Bin assisted me in reviewing the signal processing procedures and interpretation of the results, which eventually led to the

discovery of jet screech with an intermittent property. Wei Xiaofeng independently confirmed this with his acoustic data.

- I developed the short-time POD analysis technique for intermittent jet screech analysis.
- I prepared the manuscript drafts. All authors contributed in its subsequent revisions.

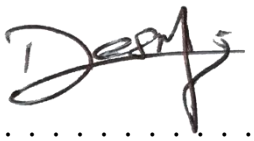

28 Dec 2019
. . . . . .
Date

. . . . . .
Lim Haoxiang Desmond

Abstract

The primary focus of this thesis is on the developments of image-based flow diagnostics for supersonic jet flow and noise control. Three different in-house techniques are presented: (1) 3D shock wave reconstruction technique based on schlieren imaging and visual hull concepts, (2) schlieren image velocimetry based on the optical flow algorithm (SIVOF), and (3) a data-driven approach to identify and characterize intermittent jet screech based on proper orthogonal decomposition (POD) of time-resolved schlieren images. The secondary focus is to provide experimental data and improve understanding on problems associated with the supersonic jet. To this end, the in-house techniques are applied in conjunction with conventional experimental techniques to Mach number 1.45 supersonic cold jets produced from convergent-divergent circular nozzles. In order to achieve flow and noise control, modifications to the nozzle exit are introduced through bevelling, and four different designs are investigated; baseline, 30° bevelled, 30° double-bevelled and 60° bevelled circular nozzles.

The 3D shock wave reconstruction technique was developed to accurately reconstruct the first shock cell of an over-expanded baseline jet, which consists of a 0.9 mm diameter Mach disk imaged at a focal distance of over 700 mm. This is a scenario typically encountered during scaled-down testing in laboratories and represents a significant challenge in the context of 3D image reconstruction. To mitigate this issue, an in-house semi-synthetic camera calibration procedure was developed to provide highly precise camera parameters. In addition, multi-view schlieren image post-processing and the volume carving visual hull approach were used to digitally

reconstruct the shock wave. The nominal cubic voxel resolution of the reconstructed shock wave was 0.044 mm, and the key parameters of under-expanded baseline and 30° bevelled jet shock structures have a 2.5% average error when compared to traditional schlieren visualization techniques. These results attest the accuracy and high-fidelity of the technique. Furthermore, since the technique directly reconstructs the shock structures without measuring a prior fluid property such as the 3D density or velocity field, it benefits from experimental simplicity and requires little resources in both experimental setup and image post-processing.

In an extended study, the 3D shock wave reconstruction technique was applied in conjunction with traditional schlieren visualization to study the effects of bevelled nozzles on standoff shocks in supersonic impinging jets. The properties of the standoff shock are known to be a strong function of the nozzle-pressure-ratio and separation distance based on the existing literature. In the study, the 3D geometry, position and stability properties of the standoff shock at three different flow configurations were investigated, and the results indicate that the standoff shock is also sensitive to the nozzle exit geometry. This was attributed to changes in the jet shock structures and the reflection point as a result of the nozzle exit modifications. Since the reflection point is a region of low pressure on the top side of the standoff shock, a localized suction effect is created which influences the standoff shock. The strength and location of the reflection point were identified as the major contributing factors leading to the observed changes in the standoff shock properties.

The schlieren image velocimetry technique based on an in-house optical flow algorithm is proposed as an alternative velocimetry technique that has the advantage

of offering a dense velocity field, is totally non-intrusive, avoids seeding challenges, and allows flow physics to be incorporated into the objective function. The optical flow algorithm incorporated modern minimization methods with second order div-curl regularizer and robust penalty functions. As a result, it outperformed a competitive open source optical flow algorithm in a synthetic validation test, with an average endpoint error of 0.701. The technique was applied to over-expanded baseline and 30° bevelled jets with the results agreeing well with earlier studies. When compared against PIV results, the much higher spatial and temporal resolution of SIVOF resulted in sharper and clearer vortical structures that can be tracked across several time-resolved frames. An embedded shear layer resulting from subsonic flow downstream of a 0.9 mm diameter Mach disk was also observed, which is testament to the high-fidelity flow field offered by SIVOF.

A new image-based technique that can identify and characterize intermittent jet screech is proposed. Short-time POD was performed on time-resolved schlieren images of under-expanded baseline and bevelled jets. Spectral analyses were performed on the time coefficients of the first POD modes, and the frequencies associated with the peak amplitudes were recorded and organized into a histogram with a bin width of St=0.01. The frequency of occurrence of the statistical mode was proposed as a parameter that can robustly identify the presence and characterize the type of jet screech, with the jet screech frequency revealed by the statistical mode. The baseline and 30° bevelled jet results revealed a peak amplitude at precisely the acoustically-validated screech frequency of St=0.25, indicating a correlation between the turbulent flow structures and the screech tone.

Acknowledgements

The submission of this thesis would not have been possible without the guidance and support of my supervisor, A/Prof New Tze How Daniel. I would like to express my heartfelt gratitude to him, for always going the extra mile in both research and non-academic matters, and for being the inspirational person that he probably doesn't know he is. I would also like to thank A/Prof Wu Jie, Asst Prof Raffaello Mariani, Dr Zang Bin, U S Vevek and Wei Xiaofeng for the numerous scientific discussions, invaluable help, advices and support they have given me. It has been a true pleasure of mine working with these people in the research group.

I would like to specially thank my external collaborators A/P Shi Shengxian, A/P Wang Qian and Dr Cui Yong Dong for the numerous scientific discussions and support throughout my PhD. I would like to thank my Thesis Advisory Committee, Asst Prof Marcos and A/P Wang Qian for their invaluable comments and guidance throughout my PhD journey. Special thanks to the Laboratory Technologist, Mr Lee Beng Teck Bernard, for his help and technical skills during my experiments.

I am fortunate to have received the opportunity to pursue a PhD in a highly reputable university, and I would like to express my appreciation to Nanyang Technological University, Singapore, for the Nanyang President's Graduate Scholarship. Support for the research work through a Singapore Ministry of Education AcRF Tier-2 grant (Grant number: MOE2014-T2-1-002) is also gratefully acknowledged. I would also like to thank Temasek Laboratories, National University of Singapore, for the equipment and laboratory support.

Last but not least, I would like to thank my family and friends for their understanding and emotional support throughout this journey. Heartfelt thanks to my fellow Residential Mentors in Crescent and Pioneer halls, for making my entire PhD enjoyable even in the face of numerous setbacks and daunting challenges. Special thanks to my SJG friends for always being there for me week in and week out. My sincerest thanks to my selfless parents, who supported me my entire life without asking for anything in return. Finally, to my beloved wife, Tan Yixin, thank you for putting up with me through my busiest period and always loving me unconditionally. Thank you for always being there for me, and I look forward to our future.

Table of Contents

List of Figures

List of Tables

List of Symbols

Abbreviations

AEPE	average endpoint error
BOS	background-oriented schlieren
BSAN	broadband shock associated noise
CCD	charge-coupled device
CFD	Computational Fluid Dynamics
CWT	Continuous Wavelet Transform
DFT	discrete Fourier transform
DMD	dynamic mode decomposition
FFT	fast Fourier transform
FPS	frames-per-second
HKE	horizontal knife-edge
IO	indeterminate-origin
LED	light-emitting diode
MOC	Method-of-Characteristics
MRF	Markov Random Field
NPR	nozzle-pressure-ratio
OFCE	optical flow constraint equation
PDE	partial differential equations
PIV	particle-image velocimetry
POD	proper orthogonal decomposition
PSD	power spectral density

SIV	schlieren image velocimetry
SIVOF	schlieren image velocimetry based on the optical flow technique
SNR	signal to noise ratio
SPL	sound pressure level
STFT	short-time Fourier transform
SVD	singular value decomposition
VH	visual hull
VKE	vertical knife-edge
2D	two-dimensional
3D	three-dimensional

Latin letters

$\boldsymbol{A}$	intrinsic matrix of camera
$\boldsymbol{a}$	POD mode coefficients
$\frac{A}{A^*}$	area ratio of nozzle exit to nozzle throat
A_x, B_x, C_x, D_x	spline parameters for x
A_y, B_y, C_y, D_y	spline parameters for y
c	local speed of sound
$C_{i=1,2\ldots n}$	camera centre of camera index i[2]
$\boldsymbol{C_i}$	position of camera index i in world coordinates[4]
$\boldsymbol{C_{n\times n}}$	two-point correlation matrix
D	nozzle exit inner diameter
dB	decibel

D_j	jet column average diameter
D_{MD}	Mach disk diameter
D_{SC}	shock cone diameter
duv	unknown flow increment to be calculated
E	objective function or energy functional
E_D	data term
E_S	regularization term
f	focal length, frequency[7]
f_c	jet plume characteristic frequency
f_s	image acquisition frequency
$f/$	f-number
$F(M_0 = 1)$	frequency of occurrence of the statistical mode
$F(M_0 = 2)$	second highest frequency of occurrence
GNC	graduated non-convexity
$\boldsymbol{H}$	homography matrix
h	separation distance of jet to impingement plate
I	image intensity
$I_{i=1,2\ldots n}$	image intensity of image index i
I_{raw}	raw image before structure-texture decomposition
I_{struct}	structural image component
J	total number of data points for cubic spline
j	image pixel index
k	Gladestone-Dale coefficient, number of image pyramid levels[6]

L	characteristic length
M	Mach number[1], a scene point in the world[2], pixel-to-world magnification factor[4, 6]
M_d	design Mach number
M_j	jet Mach number
m	a scene point in the image of first camera
m'	a scene point in the image of second camera
$(M_0 = 1)$	statistical mode
N	number of cameras[2]
n	refractive index[1], number of snapshots / images[2, 4], sample size[7]
n_1	refractive index of medium 1
n_2	refractive index of medium 2
o	jet origin position[3]
O	optical centre of first camera
O'	optical centre of second camera
p	principal point
P_o	total pressure
P_∞	ambient pressure
q	number of velocity vectors or image pixels in a single snapshot
$\boldsymbol{R}$	rotation matrix
$\boldsymbol{R_i}$	rotation matrix of camera index *i*

[1] Only for Chapter 1
[2] Only for Chapter 2
[3] Only for Chapter 3

r	radial distance from nozzle origin
Re	Reynolds number
$(\boldsymbol{R},\boldsymbol{T})$	extrinsic parameters of a camera
s	arbitrary scaling constant, standoff shock distance[5]
$S_{i=1,2\ldots n}$	silhouette image from camera index *i*
St	Strouhal number
$\boldsymbol{T}$	translation vector[2]
t	time, spline parametric parameter[4], standoff shock thickness[5]
$\boldsymbol{T_i}$	translation vector of camera index *i*
u	streamwise velocity, image velocity in the x-direction[2, 6], flow speed[1]
$\boldsymbol{U}$	POD modes (SVD approach)
u_c	convective velocity
u_j	jet exit velocity
$\boldsymbol{uv}$	velocity matrix for x-y plane
uv_{gt}	ground truth velocity field
$\widetilde{uv}$	current velocity estimate
$\boldsymbol{uw}$	velocity matrix for x-z plane
$\boldsymbol{V}$	POD mode coefficients (SVD approach)
v	image velocity in the y-direction[2, 6]
$VC_{i=1,2\ldots n}$	visual cone projected from camera index *i*
w	image velocity in the z-direction[2]

[4] Only for Chapter 4

x	axial distance from nozzle origin
x_0	x-coordinate of principal point
X_{CL}	shock cell length
X_{MD}	Mach disk axial location
X_{RP}	reflection point location
$\boldsymbol{X}(j,t)$	image matrix for POD analysis[2, 7]
$\begin{bmatrix} x \\ y \end{bmatrix}$	coordinates in image plane of first camera[2, 4]
$\begin{bmatrix} x' \\ y' \end{bmatrix}$	coordinates in image plane of second camera[2]
$\begin{bmatrix} X \\ Y \\ Z \end{bmatrix}$	world coordinates[2, 4]
y_0	y-coordinate of principal point
z	weighting variable in half-quadratic minimization problem[6]
z_D	weighting variable for robust penalty functions of data term
z_ζ	weighting variable for robust penalty functions of ζ
z_ξ	weighting variable for robust penalty functions of ξ

Greek letters

$\boldsymbol{\Lambda}$	eigenvectors
α	focal length of *x* in pixel units
β	focal length of *y* in pixel units
γ	specific heat ratio[1], skewness of image axes[2, 4]
Δf	frequency resolution

ε	hyperparameter used in robust penalty functions
ζ	auxiliary field variable for vorticity estimates
θ	azimuthal angle[4, 5, 7], hyperparameter for structural part of image to approximate original raw image[6]
θ_{IS}	intercepting shock angle[4]
θ_{RS}	reflected shock angle[4]
$\theta_{x,i}$	azimuthal rotational angle of camera index *i*
θ_1	angle of incidence
θ_2	angle of refraction
$\boldsymbol{\lambda}$	eigenvalues
λ_1	weighting constant for smoothness assumption of ξ
λ_2	weighting constant for smoothness assumption of ζ
λ_3	blending factor for blended textural image component
μ	dynamic viscosity, hyperparameter to define complex bump wavelet kernel[7]
ξ	auxiliary field variable for divergence estimates
ρ	density of fluid, robust penalty function[2, 6]
ρ_D	penalty function for data term
ρ_S	penalty function for regularizer term
$\boldsymbol{\Sigma}$	eigenvalues (SVD approach)

[5] Only for Chapter 5
[6] Only for Chapter 6
[7] Only for Chapter 7

	hyperparameter to define complex bump wavelet kernel[7],
σ	hyperparameter defining convexity of generalized Charbonnier penalty function[2, 6]
τ	weight assigned to regularization term
$\boldsymbol{\phi}$	POD modes
ϕ	polar angle from nozzle origin
$\psi(\omega)$	complex bump wavelet kernel in Fourier domain
ω	angular frequency

Superscript

$\bar{}$	time-averaged
$\sim$	fluctuating
$\widehat{}$	homogeneous coordinates
$'$	derivative of single variable function[6]
q	spline segment index
T	matrix transpose

Subscript

c	neighbourhood of pixels
t	derivative in time
x	1st order derivative in x-direction
xx	2nd order derivative in x-direction
y	1st order derivative in y-direction

yy	2nd order derivative in y-direction

Chapter 1 Introduction

1.1 Basic theory of incompressible jets

Jet flows are a type of free shear flow that may be described by a continuous injection of fluid mass and momentum into an ambient fluid, and have been the subject of academic and industrial interest for the past century [1-4]. This is in part motivated by the desire to improve understanding in the origin, evolution and decay of jet flows, and in part because of their current and future engineering applications. Some of the most common jet applications include turbofan and turbojet engines, gas turbine cooling, booster rockets for space launch vehicles, thrusters in reaction control systems of spacecrafts, industrial effluent discharge, heat transfers in electronics, aerosol spraying systems, among many others.

Early studies on the initiation, evolution and decay of large-scale coherent structures have demonstrated their influence in the dynamics of incompressible freely-exhausting jets [5, 6], and it is now widely accepted that controlling these coherent structures is effective in achieving better entrainment and mixing properties. The origins of these structures may be described with linear stability theory [7], whereby perturbations in the form of initial turbulence, acoustic waves or mechanical excitation are amplified. If the perturbations are unstable, they will lead to growths in the initial velocity perturbations and formations of coherent structures due to the Kelvin-Helmholtz instabilities. These structures form at frequencies that are dependent upon the initial shear layer thickness [8, 9], and may then undergo vortex-pairing behaviour as they propagate downstream towards the transition region, which

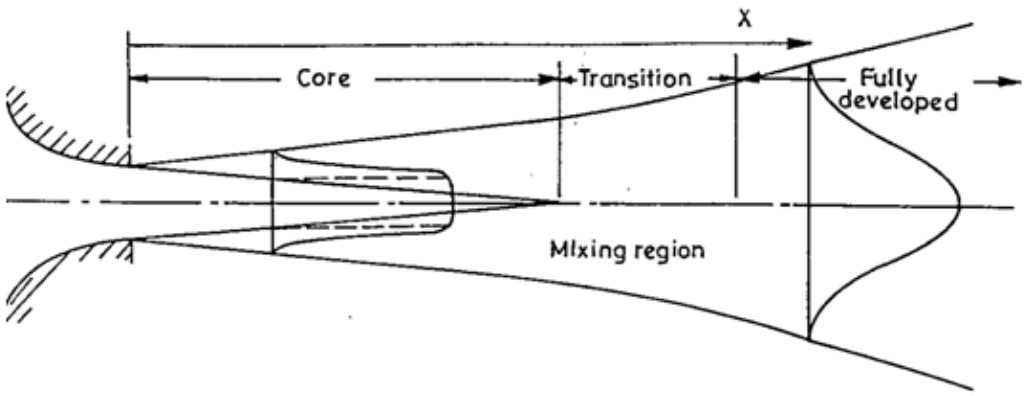

Figure 1.1: Flow schematic of an incompressible turbulent free jet [10]

decreases the vortex formation frequency and increases the structure wavelength [5, 11]. Enhanced mixing is achieved as the small-scale shear layers are rolled up within large-scale shear layers, which are rolled up within even larger-scale shear layers, and so on and so forth. This allows for very effective overall mixing between the jet stream and the ambient fluid, as the large-scale structures are very efficient in convective transport and fluid entrainment while the small-scale structures are very efficient in thorough mixing.

Further downstream from the jet exit at around five jet diameters, the potential core ends and the shear layer surrounding the potential core starts to coalesce. This marks the start of the transition region. Centreline velocity starts to decay, and three-dimensional effects dominate the jet vortex structures. Complex non-linear mechanisms define processes such as self-induction, vortex stretching, as well as disconnection and reconnection [12], which dominate the fundamental jet flow dynamics. At this stage, mixing is further enhanced when coherent structures break up and the flow gradually transits to full turbulence with smaller scale structures

dominating the flow. Further downstream beyond the transition region and in the fully developed turbulence region, the flow is said to be self-similar with velocity profile and other properties scalable by a characteristic length scale. A more detailed and comprehensive treatment of the stability analysis, origins of turbulence and coherent structures can be found in the work of Schlichting and Gersten [7].

1.2 Supersonic jets

Subsonic jets are typically characterized by the Reynolds number, defined as:

$$Re = \frac{\rho u_j L}{\mu} \tag{1.1}$$

where ρ is the density of the fluid, u_j is the jet exit velocity, L is the characteristic length and μ is the dynamic viscosity of the fluid. In supersonic flow applications, it is common to use the Mach number (M) which is defined as the ratio of the flow speed (u) to the local speed of sound (c):

$$M = \frac{u}{c} \tag{1.2}$$

For supersonic jets, the jet velocity is higher than the local speed of sound, and it is more useful to characterize them based on the design Mach number (M_d) and the nozzle-pressure-ratio (NPR). The design Mach number is related to the design of the jet nozzle and its relationship is given by:

$$\frac{A}{A^*} = \left(\frac{\gamma+1}{2}\right)^{-\frac{\gamma+1}{2(\gamma-1)}} \frac{\left(1+\frac{\gamma-1}{2}M_d^2\right)^{\frac{\gamma+1}{2(\gamma-1)}}}{M_d} \tag{1.3}$$

where γ is the specific heat ratio and $\frac{A}{A^*}$ represents the area ratio of the nozzle exit to the nozzle throat. The NPR is defined based on the operating conditions of the jet, and is given by the ratio of the total pressure of the jet (P_o) to the ambient pressure (P_∞) in which the jet is exhausted into:

$$\text{NPR} = \frac{P_o}{P_\infty} \tag{1.4}$$

Using the isentropic flow relations, the jet Mach number (M_j) can be defined based on the NPR and its relationship is given by:

$$\text{NPR} = \left(1+\frac{\gamma-1}{2}M_j^2\right)^{\frac{\gamma}{\gamma-1}} \tag{1.5}$$

or in an equivalent form:

$$M_j = \sqrt{\frac{2\left(\text{NPR}^{\frac{\gamma-1}{\gamma}}-1\right)}{\gamma-1}} \tag{1.6}$$

Supersonic jets can be over-expanded when operated at below the design NPR, perfectly expanded when operated at the design NPR, and under-expanded when operated at above the design NPR. Under-expanded jets have received considerably

more attention in the fluids community [13-20] due to their relevance in real-world engineering applications.

1.2.1 Jet noise

The supersonic jet noise is a particularly perplexing problem. Due to its significant contribution to noise pollution, it remains as one of the major technological hurdles in bringing back supersonic commercial flights over land. While effective mitigation techniques have always been of interest in the aerospace and research community, recent successes have still not led to a comprehensive understanding of the noise generation mechanism. Hence, further studies which make use of both traditional and advanced experimental/simulation techniques are important and necessary in order to shed more light on the underlying physics of the noise generation phenomenon.

The noise generated by a supersonic jet can be divided into three main categories. *Turbulent mixing noise* is produced by fine- and large-scale turbulent structures [4]. If the convective Mach number reaches supersonic speeds, the contribution from the large-scale turbulent structures will be much more dominant due to the effects of Mach wave radiation. When supersonic jets are operated at off-design conditions, quasi-steady shock structures are formed within the jet potential core. This results in the addition of two types of shock-associated noise, commonly known as the discrete *screech tones* [21, 22] and *broadband shock-associated noise* (BSAN) [23, 24]. Screech tone is produced through an acoustic feedback loop, where receptivity processes at the nozzle lip produces instability waves which grow into large-scale structures and propagate downstream. These structures may then interact with the

shock cells, producing feedback waves that propagate upstream and impinge upon the nozzle lip, resulting in further excitation of initial instabilities and thus completing the feedback loop [25]. BSAN is generated when large-scale structures interact with the quasi-steady shock cells [24, 26] (i.e. a superposition of multiple waveguide modes with different wavelengths), whereby constructive scattering leads to multiple spectra peaks with directional dependency. The importance of these three noise components can vary drastically depending on the angle of the observer to the nozzle exit, with turbulent mixing noise more dominant in the downstream direction while BSAN and screech tones typically dominate in the upstream direction [4].

1.2.2 Shock systems of imperfectly expanded jets

In a perfectly expanded jet where the exit pressure is equivalent to the ambient pressure, shock systems do not form within the potential core, and the thrust efficiency is maximised. Nonetheless, jets are more likely to be imperfectly expanded in real-world applications due to the variation of atmospheric pressure with flight altitude, atmospheric turbulence, etc. For imperfectly expanded jets, the shock systems have drawn considerable attention in supersonic jet flow studies due to its influence on the local fluid properties. Depending on the NPR, the pattern of the shock systems within the jet potential core may differ. While the Mach number and the jet divergence angle can also have some influence on the shock structures, this is to a much lesser extent and the effects are not on the same scale as the NPR [14]. The presence of shock waves is significant because they are associated with drastic and sharp changes to the local flow temperature, pressure, density and velocity [27]. In addition, the shock structures are also closely linked to the shock associated jet noise

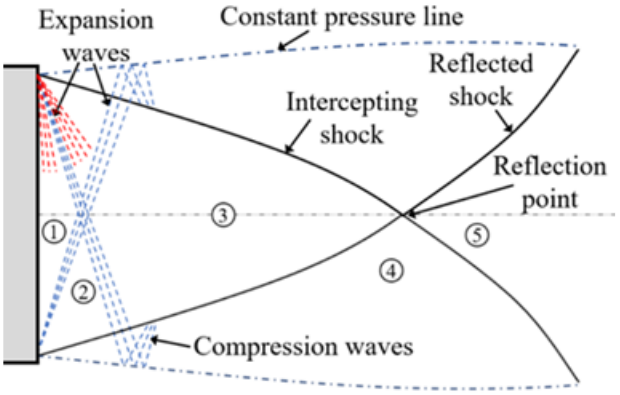

Figure 1.2: Flow schematic of a moderately under-expanded jet

[4, 24, 26, 28], as explained earlier. Clearly, the shock systems of imperfectly expanded jets are closely tied with some of the most important jet properties.

In a moderately under-expanded freely-exhausting jet as shown in Figure 1.2, the exit pressure (P_1) is higher than that of the back pressure (P_∞). For the flow to correct itself, it undergoes expansion through a series of Prandtl-Meyer expansion waves to achieve an increase in Mach number and a reduction in static pressure to P_2. Note that the oblique intercepting shocks also starts from the nozzle lips because expansion waves (in red) also exist at angles almost normal to the jet axis. This leads to an earlier reflection upon the constant pressure line as compression waves, resulting in the compression wave coalescing earlier into the intercepting shock very close to the nozzle lips. In region 2, the flow is turned away from the jet centreline, and the normal velocity component must be zero at the jet centreline, a second set of expansion wave occurs which turns the flow towards the jet centreline, resulting in further reduction of the static pressure to P_3. P_3 is now lower than the ambient pressure, hence the expansion waves reflect on the constant pressure line as compression waves and coalesce to form the intercepting oblique shocks, which then

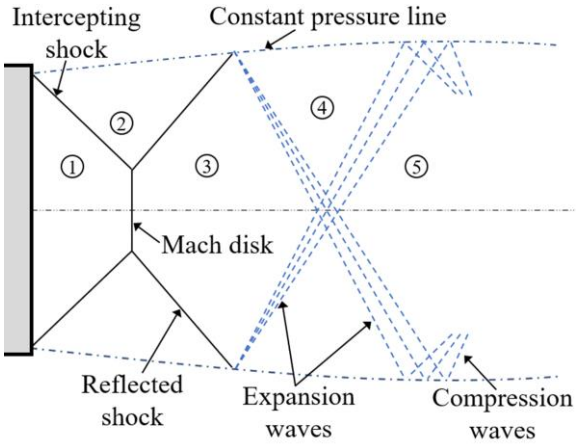

Figure 1.3: Flow schematic of an over-expanded jet

reflect off at the reflection point to form the reflected shocks further downstream. Flow in region 3 continually undergoes expansion as it travels downstream, until it passes through the intercepting and reflected shocks to arrive at region 4 and 5 with higher static pressures of P_4 and P_5 respectively. The pressure jump across the intercepting and reflected shock is dependent on the intercepting and reflected shock angle with respect to the local flow direction. Based on this flow schematic, it becomes clear that there is an adverse pressure gradient across the reflection point, and the location of the lowest static pressure lies just upstream of the reflection point. For strongly under-expanded jets where the NPR is much higher, the reflection point exists as a Mach disk, and the intercepting shocks are known as barrel shocks. The first shock cell ends at the axial location where the reflected shock impinges onto the constant pressure line and reflects as expansion waves. Beyond the first shock cell, the compression, expansion and reflection processes repeat itself downstream for several shock cells in an almost periodic manner, resulting in the formation of the characteristic “shock diamonds” frequently associated with supersonic jets.

For an over-expanded jet in which the flow schematic is presented in Figure 1.3, the exit pressure (P_1) is lower than that of the back pressure (P_∞). Since the normal velocity component must be zero at the jet centreline, the flow near the central region of the jet compresses through a Mach disk, which results in a decrease in the Mach number to subsonic and an increase in the static pressure to P_3. Near the periphery of the nozzle, the flow compresses through the intercepting oblique shock, resulting in an increase in the static pressure to P_2. The intercepting shock reflects off the Mach disk to form the reflected shock, which propagates further downstream and reflects off the constant pressure line to form expansion waves. As a result, the flow in region 2 must undergo further compression across the reflected shock to attain the static pressure of P_3. From region 3 to region 4 and 5, the flow continually undergoes expansion through the expansion waves. The entire process repeats itself in an almost periodic manner as the expansion waves reflect off the constant pressure line as compression waves, which then coalesce to form oblique shocks.

1.2.3 Shear layers

The shear layers envelop the potential core and shock systems of the supersonic jet. In supersonic jet applications, the relatively low growth rate of the supersonic shear layer poses a challenge in mixing enhancement. Other than velocity and density ratio, compressibility effects must now also be taken into consideration [29]. Through a series of pressure pitot measurements and schlieren experiments conducted for combinations of Mach number and gases [30], compressibility effects were investigated and deemed to be responsible for reducing the growth rate of the shear layers. The convective Mach number was proposed as a parameter to characterize

the compressibility effects present in the shear layer and was effective in correlating the growth rate from experimental data. A subsequent study performed across a wide range of convective Mach numbers showed highly asymmetrical convective Mach numbers during high compressibility [31], which deviated from theoretical isentropic assumptions valid for shear layers with low compressibility. This had been speculated to be due to the turbulent structures forming shocklets on a single side of the shear layer in a separate study [32].

Subsequently, supersonic-subsonic and supersonic-supersonic shear layers were investigated [33] with some rather surprising observations. In supersonic-supersonic shear layers, turbulent structures at low convective Mach numbers were observed to be very similar to the organized rolled up structures commonly observed in subsonic cases. At higher convective Mach numbers, these structures become increasingly disorganized and cease to hold any resemblance to subsonic cases. For supersonic-subsonic shear layers, turbulent structures were disorganized throughout and not comparable to those of subsonic shear layers regardless of the convective Mach number. Similar to the supersonic-supersonic case, increasing convective Mach numbers also lead to increasingly disorganized structures. Furthermore, the structures present for both supersonic-supersonic and supersonic-subsonic shear layers displayed inertness even when subjected to significant shear. This inert property of the eddies was attributed as one of the reasons behind the reduction in growth rate. Asymmetrical convective velocities were once again observed, with convective velocities following closely to the slow stream in supersonic-supersonic shear layers (slow modes), and fast stream in supersonic-subsonic shear layers (fast

modes). The dependence of convective velocities on the type of shear layer was speculated to be partially due to the observed inert behaviour of the eddies, although no physical mechanism was proposed. The problem of asymmetrical convective Mach number was speculated to be due to viscous dissipation instead of the presence of shocklets proposed in an earlier study [32]. To account for the asymmetrical convective Mach numbers observed, a heuristic linear model based on empirical observations was proposed. This was subsequently refined with a logarithmic model [34].

More recently, the research focus of shear layers has shifted to issues regarding noise mitigation and mixing enhancement. Apart from the shock associated noise, a major contribution to supersonic jet noise is the Mach wave radiation [4], which are able to propagate significant levels of noise to the far field. In order to attain noise mitigation, a secondary co-flow had been introduced to reduce the convective Mach number of eddies in the primary supersonic stream [35]. By reducing convective Mach numbers from supersonic to subsonic, this effectively eliminates Mach wave radiation thus mitigating the turbulent mixing noise component of the supersonic jet noise. The same co-flow approach can also lead to enhanced supersonic jet mixing [36], by operating the co-flow jet at pressure ratios below the design NPR to induce flow separation and shock formation within the nozzle itself. Results of potential core reducing by up to 50% of the original length suggest a strong relationship between mixing enhancement and flow separation within the nozzle. Further investigations [37, 38] revealed unsteady phenomena and asymmetrical flow separation within the nozzle, with strong instabilities growing towards the nozzle exit.

At the jet nozzle exit whereby receptivity to perturbations is deemed to be the highest, the strong instability in the initial condition appears to play a significant role in mixing enhancement.

1.3 Flow and noise control of supersonic jets with IO nozzles

Based on the brief introduction of supersonic jets thus far, it should be clear that the jet shock systems are responsible in determining the overall jet structure, near-field pressure and temperature distribution, as well as having significant influences on the shock associated jet noise. The shear layers are closely linked to jet mixing efficacy and Mach wave radiation – one of the major components of jet noise, and its compressibility effects can be characterized by the convective Mach number. Based on this understanding, an appropriate choice of flow and noise control would be one that can introduce significant modification to the shock structures as well as alter the instability characteristics of the shear layer. This can be achieved through the use of indeterminate-origin (IO) nozzles [39], which involves a systematic circumferential variation of the axial lengths of the nozzle lip. Some examples of circular IO nozzles are presented in Figure 1.4. Nozzle exit modifications can be classified as a type of passive flow control technique that has the advantage of being practical, easy to implement and has low weight penalty as compared to active flow control techniques.

Past studies have demonstrated that circular IO nozzles have the capability to simultaneously modify the shock structures and alter the instability characteristics of the shear layer [27, 40-42]. In particular, single-bevelled circular nozzles were observed to introduce thrust/jet vectoring and non-diamond shock cells [27, 42] that

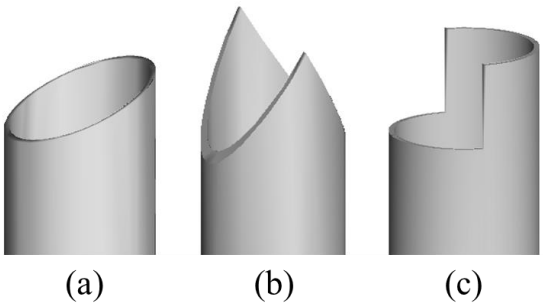

Figure 1.4: Schematics of circular indeterminate-origin jet nozzles. (a) Bevelled, (b) double-bevelled and (c) stepped nozzles.

were successful in mitigating jet screech [40] and could offer lower noise pollution in an industrial setting such as cold-spraying applications. The jet shear layer was augmented azimuthally with asymmetric spread rates observed in the two orthogonal planes. Double-bevelled circular nozzles were observed to introduce asymmetric shock cells and jet spread rates between the two orthogonal planes, with improved overall mass flux through jet entrainment [41] and potentially favourable impact upon heat transfer levels. Single- and double-bevelled rectangular nozzles [43, 44] have also been investigated and were observed to be effective in shifting the noise directivity upstream, which could further mitigate noise pollution. Spark schlieren images of these jets [45] indicate significant distortions to the overall jet shock structures, and suggest that noise pollution could be reduced by modifying the shock structures. Nozzle exit cuts made to a single side of the rectangular nozzles, specifically targeted at generating streamwise vorticity, have also demonstrate jet mixing level improvements and noise level reductions for the under-expanded jet regime [46]. More recently, surface heat transfer characteristics of impinging elliptic jets [47] were investigated, and it was observed that the standoff shock exerts significant influences upon the heat transfer rates.

1.4 Existing experimental techniques

The supersonic jet has been briefly introduced and modifications to the nozzle exit geometry have proven to be an effective passive flow control technique based on the jet literature. Nonetheless, there is limited amount of experimental data or validated numerical simulations available to fully assess the performance of circular IO jet nozzles in supersonic flow conditions. Currently, most of the existing supersonic jet literature are focused on axisymmetric nozzles [17, 18, 20, 30, 31, 33, 35, 48, 49]. Even so, based on a recent review study on under-expanded jets issued from standard circular nozzles [14], experimental data is still lacking as parameters such as the intercepting shock diameter and first shock cell length remains difficult to predict. It is not easy for any conclusive and unifying relations to be drawn as some existing results have showed large discrepancies of up to 100% [14]. Thus far, only the Mach disk location shows good agreement across different studies such that it can be accurately predicted by empirical relations.

The limited amount of experimental data can be attributed to difficulties in conducting experiments on supersonic jets, particularly for IO nozzles where significant three-dimensional (3D) distortions to the shock structures can be observed. Accurately characterizing the compressibility effects of the shear layers is also not an easy task as it involves velocimetry of the shear layer. Most of the current experimental techniques can be difficult to implement, computationally demanding and/or require expensive equipment, and these challenges need to be overcome before extensive optimization studies on supersonic jet nozzle designs can be conducted.

1.4.1 Point measurement techniques

Traditional experimental techniques that can perform flow velocimetry include the pressure pitot probe measurements and hot wire anemometry. These are point measurement techniques that can also be used to measure the 3D velocity field, from which the 3D geometry of shock structures within the jet potential core can be inferred. Nonetheless, it is very inefficient to make use of point measurement techniques for 3D measurements due to the large number of required sampling points. These techniques are also well known to be ill-suited for supersonic jet measurements as they are inherently intrusive by nature, leading to issues such as mechanical vibrations and the formation of unwanted shocks. An example of the formation of unwanted shocks due to an intrusive measuring instrument is presented in Figure 1.5.

1.4.2 Seeding-based techniques

Seeding-based techniques such as the two-dimensional (2D) cross-correlation particle-image velocimetry (PIV) is less intrusive and offers 2D velocity fields. However, seeding-based approaches are based on the assumption that seeding particles can faithfully track air particles in compressible and highly turbulent flows, including across complex shock waves whereby sharp changes in fluid properties tend to occur. In reality, seeding particle distributions are often non-uniform in such flow scenarios, and can be further complicated by particle agglomeration effects. The use of sub-micron seeding particles can reduce seeding particle drag and alleviate particle tracking uncertainties. Nonetheless, high-power lasers would have to be employed to compensate for the loss of light scattering efficiency in smaller particles. This may be an impractical option due to economical or safety reasons. Sometimes,

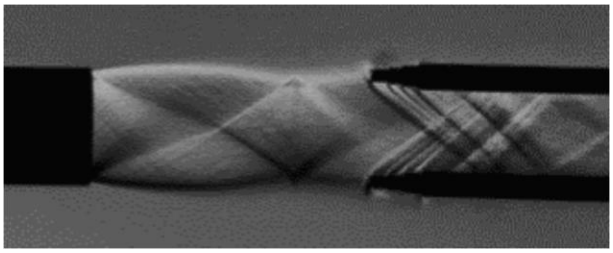

Figure 1.5: Schlieren image of unwanted shocks when a pressure probe is inserted into the supersonic jet flow field

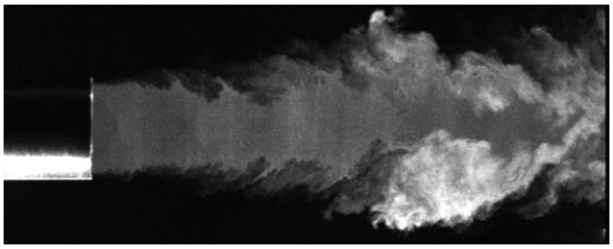

Figure 1.6: Particle-image of a supersonic jet with unwanted seeding

unwanted seeding may also occur due to unfavourable laboratory conditions. An example is presented in Figure 1.6, where the high humidity of the ambient air and low temperature of the jet core resulted in significant water vapor condensation, leading to unwanted seeding particles present in the particle-image. Image blurring may also occur due to the significant refractive index gradients across shocks, which can result in poor cross-correlation results. The spatial resolution of velocity fields may also be limited by the cross-correlation window matching approach in post-processing, which could lead to failures in resolving the smaller-scale flow structures. The temporal resolution is also limited due to practical hardware (lasers and cameras) constraints, as well as the tendency of researchers to prioritize spatial resolution in PIV experiments.

In the case of tomographic PIV, it has the advantage of offering 3D velocity field information, which is very useful in characterizing the shear layers as well as inferring the 3D geometry of shock waves. However, the challenge of controlling the seeding density is even more severe as a delicate balance must be maintained between having sufficiently large number of particles for 3D cross-correlation to be performed and having low number of particles to reduce the presence of ghost particle artefacts. Seeding control is in fact one of the most difficult challenges to overcome in supersonic jet applications and require researchers to be well-trained and have access to the right equipment (usually expensive) in order to succeed. Storage and processing of PIV data is also a realistic challenge facing many researchers as large amount of data is required to be processed in order to perform temporal averaging and accurately resolve the geometries of 3D shock structures. Because of the challenges listed above, there are very few studies which have successfully applied tomographic PIV in supersonic jet applications. One of the first studies that have done so involved a Mach number 1.4 under-expanded supersonic jet, where velocimetry of the shear layers and 3D reconstruction of the shock systems were achieved [48].

1.4.3 Schlieren-based techniques

Schlieren and shadowgraph are age old techniques first introduced by Robert Hooke (1635-1703) in the 17th century for the visualisation of invisible and inhomogeneous mediums. The resurgence, refinement and extensive testing of the modern schlieren technique was championed by August Toepler (1836-1912) in the 19th century, and modern schlieren applications now follow the same design principles of Toepler's

schlieren technique [50]. Schlieren relies on principles of light refraction in mediums with a change in refractive index. For light rays passing from a medium with refractive index, n_1, to another with refractive index, n_2, the angle of incidence, θ_1, and angle of refraction, θ_2, are governed by the Snell's law:

$$n_1 sin(\theta_1) = n_2 sin(\theta_2) \tag{1.7}$$

The Gladstone-Dale relation governs the relationship between the refractive index of a medium and its density, ρ, and is given by:

$$n - 1 = k\rho \tag{1.8}$$

where the Gladstone-Dale coefficient, k, is approximately 0.23 cm^3/g for air in standard conditions. By substituting Eq. (1.8) into Eq. (1.7), the light refraction at the interface of two mediums can be shown to be dependent upon the density difference.

A conventional Z-type double-mirror schlieren system is depicted in Figure 1.7. Broadband light from a lamp or light-emitting diode (LED) is focused by the condenser lens into a single point, where the slit functions as an aperture to improve the spatial coherence of light. The first parabolic mirror is distanced at its focal length, f, away from the slit aperture, thus producing collimated light into the test region. The schliere object in the test region has density variations, which changes the local refractive index and refract light from its original optical path. From the first mirror to the second, a minimum distance of $2f$ is required. The second parabolic mirror with the same focal length of f focuses the collimated light from the test region into

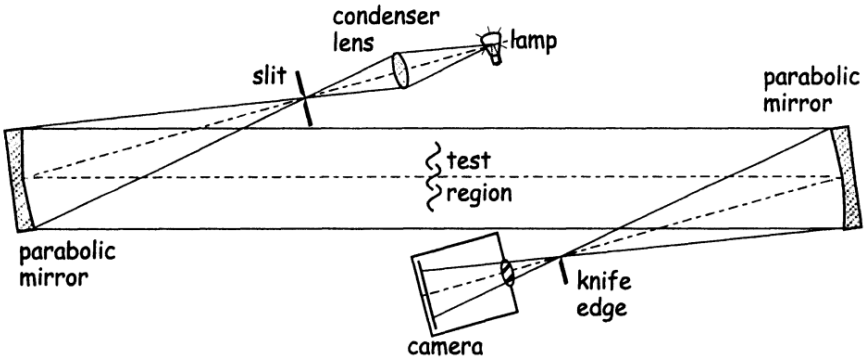

Figure 1.7: Z-type double mirror schlieren system [50]

a focal point. A knife-edge is placed at the focal point, and the direction and amount of cut-off determines the sensitivity of the schlieren system. Regions of bright and dark spots are created in the final schlieren image and digitally recorded by the camera. For the schlieren system to capture high speed convection of turbulent structures in the mixing layer without any blurring, the exposure time of the camera is required to be in the order of microseconds.

The use of a knife-edge controls schlieren sensitivity towards density variations normal to it, forming intensity patterns which gives information on the first derivative of the density integrated along the light path. Horizontal and vertical knife-edges are typically the most popular and are selected based on the flow field to provide information on the vertical and horizontal density gradients respectively. An example of schlieren images obtained with the two different knife-edge configurations is presented in Figure 1.8. In the specific case whereby no knife-edge is used, the intensity patterns, known as shadowgraphs, provide information on the second derivative of density integrated along the light path. Since schlieren and

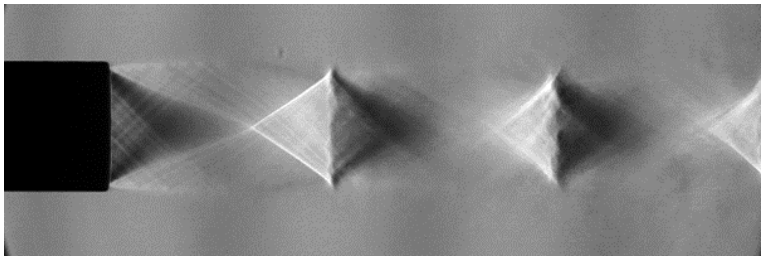

(a)

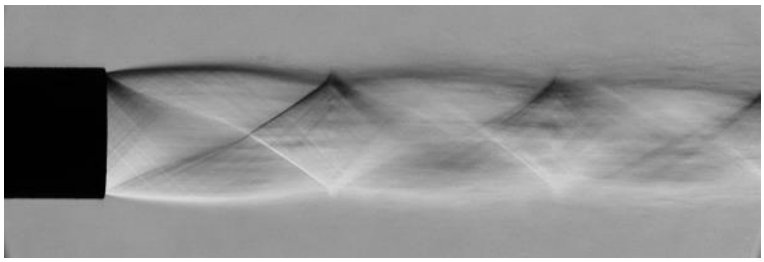

(b)

Figure 1.8: Schlieren images of an under-expanded supersonic jet using a (a) vertical and (b) horizontal knife-edge

shadowgraph patterns contain information integrated along the light path, this makes the technique very sensitive to density, temperature or pressure changes in the environment.

In terms of flow visualization techniques in supersonic jet applications, schlieren-based techniques are generally favoured for shock wave visualization purposes as they are totally non-intrusive, of relative ease in experimental design, and suitable for flows with strong density variations. Traditionally, schlieren and shadowgraph techniques have been employed for 2D visualization of flow phenomena in inhomogeneous mediums. In the past two decades, the advent of digital cameras and image-processing techniques have brought about significant developments and notable strides [51] in quantitative schlieren techniques such as the background-oriented schlieren (BOS) [52-54] and schlieren image velocimetry (SIV) [55].

Despite the popularity of schlieren techniques for shock visualizations and the inherent three-dimensionality of most real-world shocks, there have been limited attempts at digitally reconstructing 3D shock structures.

Among the schlieren-based techniques, tomographic BOS has the capability to measure the 3D density field, thus allowing shock structures to be inferred or digitally reconstructed with further post-processing. This technique typically involves the use of optical flow or cross-correlation approaches to obtain displacement vectors of density gradients, computing the light-path integrated density field by solution of the Poisson equation, and using filtered back-projection techniques to obtain the final 3D density field. Similar to tomographic PIV whereby the global 3D velocity field is required, tomographic BOS technique also requires the global 3D density field to be known first before the shock wave geometry can be recovered. Current relevant applications of tomographic BOS include obtaining 3D shock structures from supersonic flow over cones [56, 57] and from under-expanded axisymmetric jets [20]. Other applications include the reconstruction of unsteady and asymmetric hot gas flow's density field using a synchronized 16 cameras configuration [58], and the reconstruction of low speed plume flows using a 12 cameras configuration by posing the problem in an optimization framework [59]. However, the tomographic BOS technique has its limitations which include image blurring across shocks with significant refractive index change, camera calibration issues when dealing with multiple camera configurations [60], large memory requirements and computational cost (even during the camera calibration stage), as well as limited resolution of shock

waves when computed density fields are reconstructed from a limited number of camera views or with low resolution cameras.

1.5 Research problems

Passive flow control of supersonic jets using nonconventional nozzles is desirable in order to control the jet shock structures and the shear layer, which has direct implications on the jet noise generation and mixing properties. However, the limitations of existing experimental techniques mean that extensive studies to design an optimal supersonic nozzle can be difficult and inefficient to perform. Furthermore, even for conventional circular jet nozzles, the physical mechanism behind ongoing issues such as the jet noise is still poorly understood due to a lack of experimental and validated numerical data. Experimental results are in demand to improve understanding on supersonic jets and validate current Computational Fluid Dynamics (CFD) models. As such, the following points sums up the current research problems related to supersonic jets.

- Lack of experimental results, particularly for nonconventional nozzles.
- Supersonic jet noise is still not well understood.
- Traditional point measurement experimental techniques are ill-suited for supersonic jet applications due to their intrusive nature which leads to unwanted shocks, and their general inefficiency in 3D applications.
- Traditional 2D schlieren imaging is still predominantly employed in supersonic jet studies which involve 3D shock structures.

- Tomographic BOS and tomographic PIV have high experimental complexity and requires significant experience and resources for both experimental setup and image post-processing, which is not ideal for extensive optimization studies.
- Seeding-based PIV techniques are linked to problems such as non-uniform particle distribution, poor visibility of particles, particle agglomeration, image blurring due to strong refractive index change across shock waves, low spatial and temporal resolution of velocity field, and high experimental complexity in supersonic jet applications.

1.6 Research objectives

In view of the current research problems, the following research objectives are formulated:

(1) Develop a schlieren-based 3D shock wave reconstruction technique that can avoid the need to measure a prior fluid property.

(2) Demonstrate the capability of the 3D shock wave reconstruction technique by extending it to analyse highly complex and asymmetric shock structures in supersonic impinging bevelled jets.

(3) Develop a schlieren-based velocimetry technique which does not rely on seeding particles and is able to offer higher spatial and temporal resolution as compared to existing PIV techniques.

(4) Develop a data-driven schlieren-based flow diagnostics technique for supersonic jet screech studies.

(5) Provide experimental data for supersonic jets produced by nonconventional nozzles.

Essentially, the primary focus of this thesis is on the development of novel experimental techniques for the study of supersonic jets. For the qualitative aspect, schlieren images obtained at multiple viewpoints are post-processed using the visual hull 3D reconstruction technique, to provide 3D visualization of complex and asymmetric shock systems produced from nonconventional nozzles. For the quantitative aspect, SIV achieved using optical flow is able to offer much higher spatial and temporal resolution of velocity fields as compared to existing PIV techniques. In addition, a data-driven technique based on time-resolved schlieren-based proper orthogonal decomposition (POD) is developed to identify and characterize the presence of intermittent jet screech. Successful development and application of these techniques to highly complex supersonic jets where asymmetric shock systems are produced can reveal further insights and improve understanding on the flow mechanisms responsible for some of the empirical observations. Hence, the secondary focus of this thesis is on understanding the underlying flow physics of supersonic jets, using both existing and the newly developed experimental techniques.

1.7 Layout of thesis

In Chapter 1, an introduction of the supersonic jet and existing experimental techniques have been presented. The research problems and objectives have also been identified. Chapter 2 provides the literature review for image-based 3D reconstruction techniques, variational optical flow model and implementation

procedures, and a data-based modal decomposition method known as the POD in the fluid's community. Chapter 3 presents the supersonic jet apparatus, test nozzles and schlieren setup. Chapter 4 presents the 3D shock wave reconstruction technique based on the visual hull concept and a novel semi-synthetic camera calibration procedure. Its capabilities are demonstrated by applying the technique to asymmetric jet shock structures. Chapter 5 presents a study on under-expanded impinging jets, which employs the 3D shock wave reconstruction technique to study the role of the reflection point on the standoff shock behaviour. Chapter 6 presents the SIV technique based on the optical flow algorithm and demonstrates its capability by applying it to time-resolved schlieren images of over-expanded supersonic jets. Chapter 7 reports on a data-driven approach to identify and characterize intermittent jet screech based on time-resolved schlieren-based POD. Chapter 8 concludes the contribution of this thesis.

Chapter 2 Literature Review

2.1 3D shock wave reconstruction

In supersonic jet applications, direct reconstruction of shock waves based on schlieren images has the advantage of experimental simplicity and efficiency. Here, the term "direct reconstruction" refers to the 3D reconstruction of shock waves based on images processing techniques, without the need to measure a prior fluid property such as density or velocity. Despite the clear advantages, to the best of the author's knowledge, there is limited amount of work performed on direct reconstruction of shock waves.

2.1.1 Structure-from-motion

Three-dimensional reconstructions from multiple 2D images may be broadly classified into structure-from-motion [61, 62] and shape-from-silhouette techniques [63, 64]. In structure-from-motion techniques, reconstruction of a static scene is achieved by moving a single camera to multiple positions and capturing images from different viewpoints. This is also equivalent to the multi-view stereo technique whereby multiple synchronized cameras at different viewpoints capture an image of a static scene simultaneously. Full knowledge of the camera parameters is required, necessitating a camera calibration involving an external calibration board. Once the camera calibration is completed and the stereo images captured, the correspondence problem must be solved before 3D recovery of a structure using triangulation and surface fitting methods is possible. This is traditionally the most difficult problem for stereo analysis approaches, and common techniques to deal with the

correspondence problem include the template matching and feature matching schemes.

Template matching schemes involve cross-correlation of image intensity values. This is suitable when the region to be reconstructed is highly textured, and even more so if coloured images are available. In cross-correlation approaches, the choice of the window size determines the density of disparity map and robustness. In order to improve the density of disparity map and robustness against false matches, correlation was performed twice in parallel by reversing the roles of both images and passing only consistent matches in both correlations [65]. Multi-resolution schemes were used in conjunction with the aforementioned parallel correlation technique, and disparity map at every single resolution level was combined to obtain a dense disparity map. Inconsistent matches were rejected, and interpolation was performed to fill in for missing information. While this allows a 3px × 3px correlation window to be achieved, the approach was not robust against repetitive patterns, and a dense disparity map cannot be achieved in low textured images. Zhang et al. [66] adopted correlation techniques to first identify matching candidates, and then used a relaxation technique to zero down on the correct match. The relaxation technique involves calculating the neighbourhood's support for a candidate based on certain constraints such as affine approximation and continuity in scene flows. Interestingly, this was conducted on uncalibrated images; i.e. correlation was conducted in a 2D search instead of a 1D search along the epipolar line. Using the initial correspondence information, a fundamental matrix was then robustly determined to estimate the epipolar geometry, and a second round of correlation which considers the epipolar

geometry was carried out to refine the correspondence. As with most literature based on correlation techniques, the performance is very dependent on the level of texture available in the image.

Feature matching schemes may work better than cross-correlation methods due to their geometric and photometric invariance properties [67], which is generally able to improve robustness and limit the influence of noise. In the context of shock systems issuing from a supersonic jet, features may include "corners" created by shock reflections, or "edges" from the shock structures itself. The Scale Invariant Feature Transform (SIFT) [68] is one of the most popular robust feature matching scheme. It is invariant to image scaling and rotation and is robust against illumination changes and viewpoints. Images first undergo scale space sampling and subtraction operations to obtain difference-of-Gaussian images. From these images, feature points may be identified from maxima and minima pixel values, while those with poor contrast and edges are robustly rejected. Feature points are then given an orientation vector (i.e. descriptor) to uniquely identify them, and this allows corresponding points in two images to be matched. While most literature regard edges as poor features that should be filtered out [68], it is noted that edge features had successfully been used for homography computation [69]. An extension to SIFT is the Speeded Up Robust Features (SURF) algorithm [70, 71], which basically aims to speed up the feature point detection and descriptor process without compromising too much on distinctiveness. While this approach is fast and yields reasonable result, it is more suitable and necessary for real-time applications. In general, feature matching schemes are not able to provide disparity map that is sufficiently dense for

reconstruction to be performed accurately. Additional constraints and prior knowledge of the object to be reconstructed may need to be incorporated during the surface reconstruction stage for satisfactory results.

In the fluids community, the reconstruction of a bursting bubble based on stereoscopic shadowgraphs and the projective geometry mathematical framework [72] is probably the most relevant study to the current intended shock wave reconstruction application. Perspective projection was satisfied by employing two Z-type double-mirror shadowgraph system with an offset angle and placing the test section in the convergent section of the optical paths. The reconstruction algorithm was based on a structure-from-motion approach [73], with the correspondence problem robustly matched through the use of the epipolar geometry [66]. It must be emphasized that structure-from-motion (i.e. multi-view stereo) techniques are only capable of reconstructing stereoscopic scenes which provide depth perception to the viewer, and do not offer full 3D information regardless of the viewing angle. More importantly, it is very challenging to apply stereo reconstruction techniques on schlieren images of shock waves due to the integrative nature of schlieren and the general lack of features and textures on the surface of shock structures.

2.1.2 Shape-from-silhouette

Shape-from-silhouette techniques rely on the reconstruction of volumes or surfaces in the scene such that the reconstruction is consistent with the input silhouette images from different viewpoints. This idea was first introduced by Baumgart [74], and shapes reconstructed from this approach were subsequently termed “visual hull” (VH) by Laurentini [75]. More concisely, VH is defined as an object’s maximal

geometrical representation that is consistent with silhouette images from any viewpoints lying outside the object's convex hull. The VH approach for 3D reconstruction has several key advantages in the current shock wave reconstruction application. Firstly, the reconstructed object is fully 3D and provides a more complete visualization of the reconstructed object, as well as having the potential to allow important geometrical information to be extracted. Secondly, VH implementation is relatively straightforward from the perspectives of both experimental setup and data processing, especially when compared to multi-view stereo techniques which require special attention for the correspondence problem to be solved [68, 70]. Thirdly, silhouette-based approaches are good fits with schlieren techniques, whereby "shadow"-like intensity patterns are created due to density variations along the optical light path. Finally, as opposed to multi-view stereo methods, VH methods are inherently more robust, and allow the integration of a semi-synthetic camera calibration technique which serves to relax the requirements on experimental camera calibration, while providing reasonably accurate reconstruction of miniature objects typically encountered during scaled-down testing.

Despite the advantages and attractiveness of the VH approach, there are some limitations which restrict its application in reconstruction problems. Under the assumption that no viewpoints lie inside an object's convex hull, the VH approach performs poorly when reconstructing concave objects due to the inability of the visual cone in resolving concavities. This is best elucidated in Figure 2.1, where two cameras capturing images of a convex object (a solid cylinder) is shown in Figure 2.1(a), while Figure 2.1(b) depicts the exact same setup but the object now has a

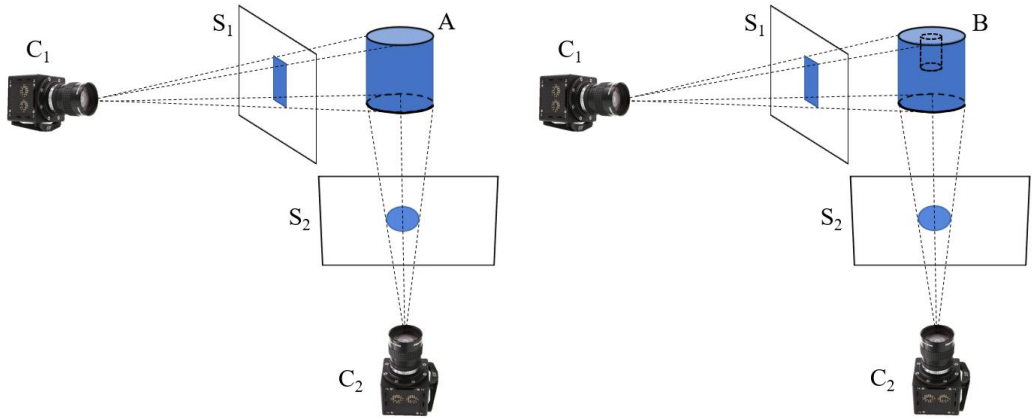

(a) (b)

Figure 2.1: Illustration of the voxel-based VH technique with (a) convex object (b) concave object

concavity (cylinder with a hole in the centre). Here, it should be highlighted that object A in Figure 2.1(a) is the convex hull of object B in Figure 2.1(b). Object A can be reconstructed accurately if there is a sufficiently large number of cameras positioned at different viewing angles. However, object B can never be accurately reconstructed even with an infinite number of cameras, due to the assumption of no viewpoints lying inside B's convex hull, which leads to a lack of information on the concavity. VH reconstruction also requires multiple viewpoints to achieve accurate results (the higher the number of viewpoints, the higher the accuracy), and this is usually not feasible in dynamic scenes which restricts VH applications to static scenes.

The example as described above can be translated to an imperfectly expanded supersonic jet with shock structures contained within the potential core. In a supersonic jet, the jet boundary can be disregarded as it will not take part in the reconstruction and it does not hide/obstruct the shock structures that are to be

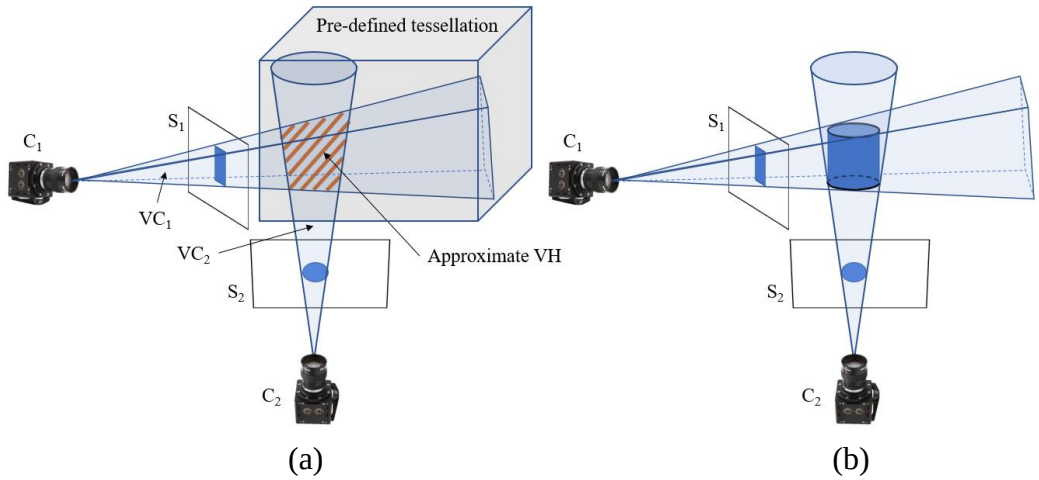

Figure 2.2: Illustration of the volume carving concept (a) visual cones projected into the pre-defined tessellation (b) comparison with original object

reconstructed. Hence, only the shock structure itself needs to be considered, and it will constitute the outer-most layer (analogous to the cylinder in Figure 2.1).

Two main categories of VH techniques have the capabilities of achieving full 3D reconstruction of an object: surface-based [76], and voxel-based [75] VH technique. Surface-based VH technique uses polyhedral surfaces to represent the VH, which is constructed using points, edges and faces generated through the intersection of occluding contours projected from silhouette images. It is computationally less intensive than the voxel-based VH method and can avoid space discretization problems which may result in visually boxy VH. However, numerical instability is an issue when dealing with complex objects, and implementation is not as straightforward as the voxel-based VH technique. The voxel-based VH approach is preferred for the current application as there is no requirement for real-time reconstruction, and numerical stability is also guaranteed which allows the technique to be potentially extended to more complex flow scenarios. The voxel-based VH

technique relies on a systematic volume carving approach to arrive at a volumetric representation of the object's VH.

As shown in Figure 2.2(a), a pre-defined tessellation of cubic voxels is sampled and subjected to a binary decision-making process when visual cones ($VC_{i=1,2\ldots n}$) are projected from the camera centre ($C_{i=1,2\ldots n}$) and silhouette images ($S_{i=1,2\ldots n}$) into the tessellation. Sampled voxels that do not belong in the projected visual cones are discarded, and the remaining voxels constitute the object's approximate VH. Figure 2.2(b) illustrates the difference between the original object and the approximate VH generated from two viewpoints. It can be inferred that with an infinite image resolution and number of viewpoints, the approximate VH becomes the object's true VH. In the rest of this thesis, for the sake of brevity, the term "VH" will be used to represent the approximate VH since the number of viewpoints and resolution of the silhouette images cannot be infinite.

2.1.3 Camera calibration

For direct reconstruction of shock waves using image-based techniques, full knowledge of the position and orientation of the cameras is required. Using the classic pinhole camera model as shown in Figure 2.3, the camera coordinate system can be represented by O for the optical centre of the first camera, and O' for the optical centre of the second camera. By designating the first camera coordinate system as the world coordinate system, a point from the scene in world coordinates can then be represented by $M = \begin{bmatrix} X \\ Y \\ Z \end{bmatrix}$, while the corresponding image coordinates for

the first and second cameras are $m = \begin{bmatrix} x \\ y \end{bmatrix}$ and $m' = \begin{bmatrix} x' \\ y' \end{bmatrix}$ respectively. The camera coordinate systems are related to the world coordinate system by the rotation matrix, $\boldsymbol{R}$, and translation vector, $\boldsymbol{T}$. This relation is also known as the extrinsic parameters of a camera, $(\boldsymbol{R}, \boldsymbol{T})$, and determines the whereabouts of a camera in the world. To relate the image plane coordinate system to the camera coordinate system, an intrinsic matrix, $\boldsymbol{A}$, is required. The intrinsic matrix describes the skewness of the image axes, γ, coordinates of the principal point, $p = (x_0, y_0)$, and focal length of x- and y-direction expressed in pixel units as (α, β). Together, the intrinsic and extrinsic parameters relate a scene point in the world to its corresponding point in the image plane. It is customary to use homogeneous coordinates (denoted by $\widehat{hat}$) to represent the Cartesian coordinate systems defined above which can simplify the mathematical analysis. Hence, the complete camera model with an arbitrary scaling constant, s, can be expressed as:

$$s\widehat{m} = \boldsymbol{A}[\boldsymbol{R}, \boldsymbol{T}]\widehat{M} \tag{2.1}$$

$$s \underbrace{\begin{bmatrix} x \\ y \\ 1 \end{bmatrix}}_{\substack{Image \\ coordinates}} = \underbrace{\begin{bmatrix} \alpha & \gamma & x_0 \\ 0 & \beta & y_0 \\ 0 & 0 & 1 \end{bmatrix}}_{\substack{Intrinsic \\ parameters}} \underbrace{\begin{bmatrix} r_{11} & r_{12} & r_{13} & t_1 \\ r_{21} & r_{22} & r_{23} & t_2 \\ r_{31} & r_{32} & r_{33} & t_3 \end{bmatrix}}_{\substack{Extrinsic \\ parameters}} \underbrace{\begin{bmatrix} X \\ Y \\ Z \\ 1 \end{bmatrix}}_{\substack{World \\ coordinates}} \tag{2.2}$$

Furthermore, since the origin of the world coordinate system can be defined arbitrarily, defining $Z = 0$ at the scene plane is convenient and will reduce the complexity of the mathematical analysis. Dropping the third column of extrinsic parameter matrix, the 3 × 3 homography matrix can then be expressed as:

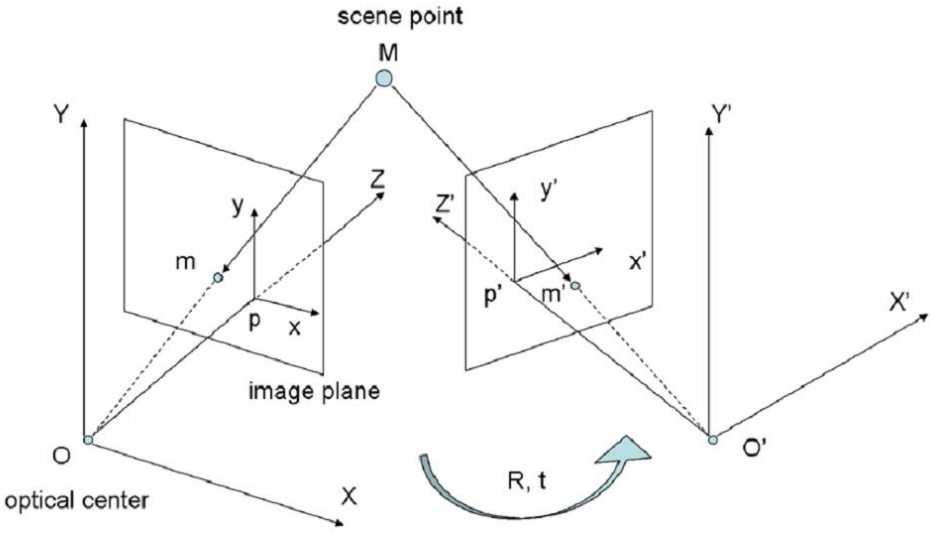

Figure 2.3: Coordinate system based on the pinhole camera model [72]

$$\boldsymbol{H} = \boldsymbol{A}[\boldsymbol{R}, \boldsymbol{t}] = \underbrace{(\boldsymbol{h_1}, \boldsymbol{h_2}, \boldsymbol{h_3})}_{Homography} = \underbrace{\begin{bmatrix} \alpha & \gamma & x_0 \\ 0 & \beta & y_0 \\ 0 & 0 & 1 \end{bmatrix}}_{\boldsymbol{A}} \underbrace{\begin{bmatrix} r_{11} & r_{12} & t_1 \\ r_{21} & r_{22} & t_2 \\ r_{31} & r_{32} & t_3 \end{bmatrix}}_{(\boldsymbol{r_1}, \boldsymbol{r_2}, \boldsymbol{t})} \tag{2.3}$$

$$\boldsymbol{h_1} = \boldsymbol{A}\boldsymbol{r_1}, \qquad \boldsymbol{h_2} = \boldsymbol{A}\boldsymbol{r_2} \tag{2.4}$$

For orthogonal rotational vectors:

$$\boldsymbol{r_1^T r_2} = 0 \quad and \quad \boldsymbol{r_2^T r_1} = 0 \tag{2.5}$$

With Eq. (2.4) and (2.5):

$$\boldsymbol{h_1^T A^{-T} A^{-1} h_2} = 0 \tag{2.6}$$

$$\boldsymbol{h_1^T A^{-T} A^{-1} h_1 - h_2^T A^{-T} A^{-1} h_2} = 0 \tag{2.7}$$

$$\text{Let } \boldsymbol{B} = \boldsymbol{A^{-T}A^{-1}} = \begin{bmatrix} B_{11} & B_{12} & B_{13} \\ B_{21} & B_{22} & B_{23} \\ B_{31} & B_{32} & B_{33} \end{bmatrix} \tag{2.8}$$

where **B** is symmetric and positive definite. Since **B** is symmetric, it can be fully defined by a vector with 6 degree of freedom.

$$\boldsymbol{b} = [B_{11}, B_{12}, B_{22}, B_{13}, B_{23}, B_{33}]^T \tag{2.9}$$

Using Eq. (2.6), (2.7) and (2.8), a set of linear equations can be set up in the form of:

$$\boldsymbol{Vb} = \begin{bmatrix} v_{12} \\ (v_{11} - v_{12}) \end{bmatrix} \boldsymbol{b} = 0 \tag{2.10}$$

$$\begin{aligned} v_{ij} = \big[& h_i(1)h_j(1), \quad h_i(1)h_j(2) \\ & + h_i(2)h_j(1), \quad h_i(2)h_j(2), \quad h_i(3)h_j(1) \\ & + h_i(1)h_j(3), \quad h_i(3)h_j(2) + h_i(2)h_j(3), \quad h_i(3)h_j(3) \big] \end{aligned} \tag{2.11}$$

For N number of homographies (camera views), $\boldsymbol{V}$ will become a $2N$-by-6 matrix. Since vector $\boldsymbol{b}$ has 6 degrees of freedom, and each view provides 2 linear equations, solutions to $\boldsymbol{Vb} = 0$ can be obtained with a minimum of 3 different views. In general, more views are usually favoured to reduce the influence of noise, and the resulting overdetermined system is solved by a least squares minimization approach. To obtain the intrinsic and extrinsic parameters, camera calibration can be performed using an external calibration board. Most literature and open source codes originating from computer vision make use of a checkerboard pattern.

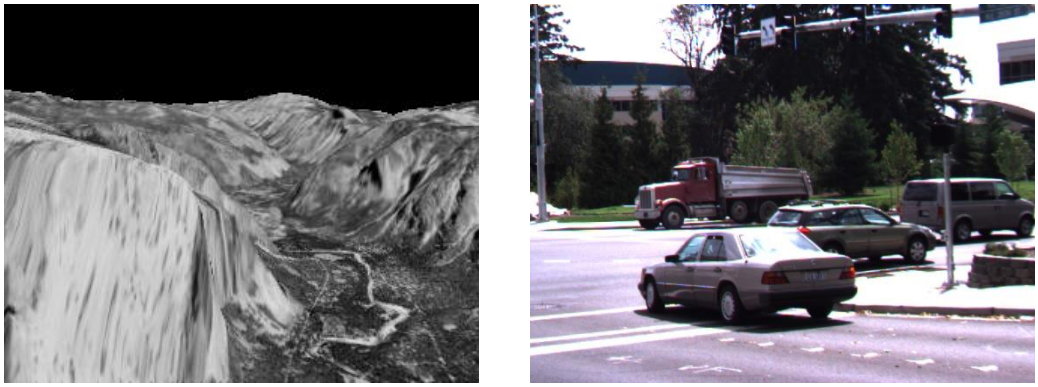

(a) (b)

Figure 2.4: Sample images of the (a) synthetic Yosemite and (b) real-world Dumptruck evaluation datasets, obtained from the Middlebury Flow site [77]

2.2 Optical flow in schlieren image velocimetry

Optical flow originated from the computer vision community and was developed to extract global velocity fields from rigid body motion images [78-80]. Some examples include the Yosemite and Dumptruck sequence as shown in Figure 2.4. More recently, optical flow has been extended to a wider range of applications including robot navigation, object and people tracking, meteorology, incompressible fluid flow studies, among many others. In particular, variational optical flow techniques are very attractive as it has the capability to incorporate physics or empirical observations into the objective function, and it can also offer a dense velocity field of one velocity vector per pixel. This is in contrast to traditional cross-correlation techniques commonly used in PIV post-processing which relies on statistical correlations via a window matching approach. Statistical correlation lead to results which are not grounded by physics, and the use of an interrogation window intrinsically limits the spatial resolution of the velocity field. In the context of supersonic flows where experimental conditions can be relatively harsh, successful implementation of optical

flow for SIV (i.e. schlieren image velocimetry) may be potentially rewarding as dense velocity fields can be achieved without being intrusive or reliant on seeding particles. The capabilities of current schlieren systems can be extended beyond a flow visualization tool, enabling quantitative studies in harsh environments where traditional experimental techniques may fall short of. Hereinafter, for the sake of brevity, the term "SIVOF" will be used to abbreviate schlieren image velocimetry based on the optical flow technique.

2.2.1 Variational optical flow

Variational optical flow was first introduced by Horn and Schunck [78] based on the assumption of brightness constancy across successive images. In an image sequence (or image pair), the pixel intensity of an object in the image plane can be expressed as $I(x(t), y(t), t)$, and its material derivative under the assumption of brightness constancy can be expressed as:

$$\frac{DI(x(t), y(t), t)}{Dt} = 0 \tag{2.12}$$

where $(x(t), y(t))$ represents the object's trajectory in image coordinates. Using the chain rule, Eq. (2.12) may be expressed in a linearized form as:

$$I_t + I_x u + I_y v = 0 \tag{2.13}$$

where $u = {dx}/{dt}$ and $v = {dy}/{dt}$ (i.e. image velocities in the x and y directions respectively) and the subscripts represent derivatives in the respective directions. Equation (2.13) is known as the optical flow constraint equation (OFCE) and has two

unknowns in u and v. By itself, it is insufficient in computing image velocities since there are two unknowns for a single pixel, leading to the well documented aperture problem [81]. An additional constraint is required in order to arrive at a unique and non-trivial solution. For the seminal optical flow work of Horn and Schunck [78], a smoothness assumption of the global velocity field was introduced as a regularizer, and the objective function (i.e. energy functional) can be expressed as:

$$E = \int \underbrace{\left(I_t + I_x u + I_y v\right)^2}_{Data\ term} + \tau \underbrace{\left(|\nabla u|^2 + |\nabla v|^2\right)}_{Regularization\ term} dxdy \tag{2.14}$$

where the data term represents the brightness constancy assumption, the regularization term represents the smoothness assumption, and τ represents the relative weight assigned to the regularization term (also known as the Lagrange multiplier in the context of variational calculus). Minimization of Eq. (2.14) can then lead to solutions of the image velocities.

There are several ways to minimize Eq. (2.14) using numerical discretization methods. At the level of the energy functional (Eq. (2.14)), minimization can be directly performed using Markov Random Field (MRF) based methods. Alternatively, minimization can also be performed on the analytical Euler-Lagrange PDEs that satisfy Eq. (2.14). This can be derived by first re-expressing Eq. (2.14) as follows:

$$E(u,v) = \int \underbrace{\left(I_t + I_x u + I_y v\right)^2}_{Data\ term} + \tau \underbrace{\left(u_x^2 + u_y^2 + v_x^2 + v_y^2\right)}_{Regularization\ term} dxdy \tag{2.15}$$

Equation (2.15) has two unknown functions in $u(x, y)$ and $v(x, y)$, which are dependent on two variables in x and y. Hence, the system of Euler-Lagrange equations with respect to $u(x, y)$ and $v(x, y)$ are:

$$\frac{\partial E}{\partial u} - \left(\frac{\partial}{\partial x}\frac{\partial E}{\partial u_x} + \frac{\partial}{\partial y}\frac{\partial E}{\partial u_y}\right) = 0 \tag{2.16}$$

$$\frac{\partial E}{\partial v} - \left(\frac{\partial}{\partial x}\frac{\partial E}{\partial v_x} + \frac{\partial}{\partial y}\frac{\partial E}{\partial v_y}\right) = 0 \tag{2.17}$$

Solving for Eq. (2.16) and (2.17) and expressing only the final form of the equations:

$$I_x^2 u + I_x I_y v + I_x I_t - \tau\left(u_{xx} + u_{yy}\right) = 0 \tag{2.18}$$

$$I_y^2 v + I_x I_y u + I_y I_t - \tau\left(v_{xx} + v_{yy}\right) = 0 \tag{2.19}$$

Equation (2.18) and (2.19) are linear equations which can be discretized and solved numerically through the use of any efficient linear solvers such as the Gauss-elimination, Jacobi, Conjugate Gradients, Gauss-Seidel, etc.

2.2.2 Related work

In the original Horn and Schunck's implementation of optical flow, the regularization term have been shown to penalize vorticity and divergence estimates [82, 83]. While this may not necessarily be an issue in rigid body motion applications, it is not physically meaningful in the context of fluid mechanics. Thus, several attempts have been made to modify the objective function such that it is more physically meaningful within the context of fluid flow applications. Corpetti et al. [82, 83] applied optical

flow to meteorological images, and used the continuity equation to derive the objective function in order to account for compressibility effects. The regularization term was replaced with one that assumes a smoothly varying divergence and vorticity field. Subsequently, Liu and Shen [84] derived the connection between fluid flow and optical flow in several common experimental methods such as PIV, shadowgraph and schlieren imaging. To incorporate more physics into the optical flow analysis, Ruhnau et al. [85] simplified the Navier-Stokes equation into a vorticity transport model and used it as a physical constraint for turbulence effects in incompressible fluids. Heitz et al. [86] used a simplified vorticity transport model to predict the vorticity and divergence field that is propagated after a small time step, before updating the propagated velocity and using it as a physical constraint to regularize the flow. Based on the current experimental fluid mechanics literature, and to the best of the author's knowledge, optical flow has mostly been applied to incompressible fluid flows with little emphasis on SIV of supersonic jets.

Apart from developing an optical flow model suitable for supersonic jet application, the schemes (the *method*) used in minimizing the objective function (the *model*) play a major role for robustly estimating accurate velocity fields. Multi-resolution image pyramids have often been used to deal with large displacements [52, 79, 82, 87], and has proven to be effective and essential for accurate optical flow results. For illustration, the multi-resolution scheme as shown in Figure 2.5 has three image pyramid levels constructed from subsampling and Gaussian smoothing of the original image pair. At the coarsest level, the largest motions are resolved, and the velocity field is up-sampled via interpolations to the next resolution level. This serves to

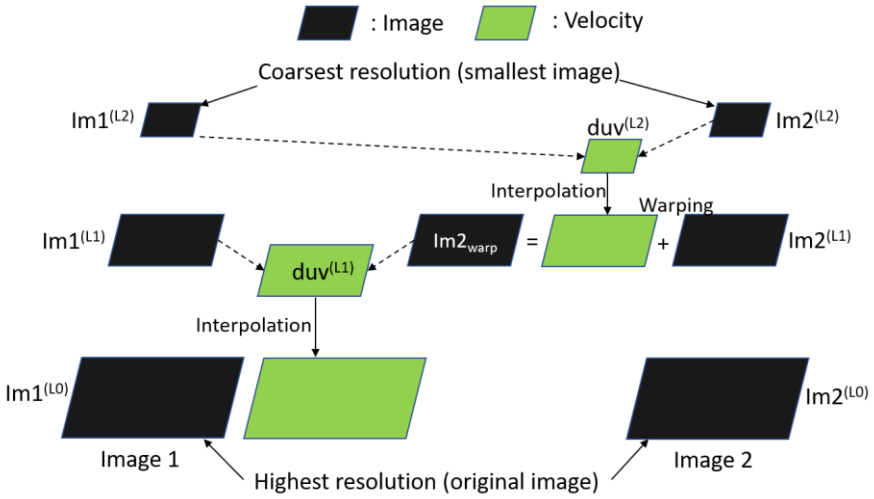

Figure 2.5: Multi-resolution scheme for large pixel displacements

initialize the calculation of the incremental velocities for the new resolution level through an image warping operation. The process repeats itself until the finest resolution level in which the original image pair exists. Robustness of optical flow technique in large motion applications can be improved using this technique, as the image size and maximum pixel displacement decrease during the subsampling process. However, the subsampling process can also lead to a loss of motion details for the smallest spatial structures. In particular, *motions of small spatial structures that are larger than the size of itself cannot be handled adequately* [88] by the multi-resolution scheme. This is an intrinsic limitation associated with the multi-resolution scheme, and due diligence must be exercised when incorporating the multi-resolution scheme in optical flow algorithms. It implies that the camera framing rate requirements used in optical flow-based experiments is dictated not only by the speed of the flow, but also by the spatial size of the flow structures that is to be studied.

In Eq. (2.14), the quadratic penalty function (L2-norm) associated with both the data and regularization term has the effect of assigning large weights to outliers, hence leading to high noise sensitivity and over-smoothed solutions. To circumvent this problem, it is common to replace the quadratic penalty function with robust penalty functions, which have been demonstrated to perform much better than quadratic penalty functions in optical flow analysis [89, 90]. Corpetti et al. [83] used the non-convex Leclerc penalty function for both the data and regularization term, defined as:

$$\rho(x) = 1 - \exp(-\varepsilon x^2) \tag{2.20}$$

where ε is some positive hyperparameter. Sun et al. [89] investigated the generalized Charbonnier penalty function, defined as:

$$\rho(x) = (x^2 + \varepsilon^2)^{\sigma} \tag{2.21}$$

where σ determines the convexity of the function. For $\sigma = 0.5$, the function is the convex Charbonnier penalty, and for $\sigma < 0.5$, the function becomes increasingly non-convex. The most accurate optical flow results were obtained when $\sigma = 0.45$ (slightly non-convex Charbonnier penalty function), which also outperformed the more robust and non-convex Lorentzian penalty function [90], defined as:

$$\rho(x) = \log\left(1 + 0.5\left(\frac{x}{\varepsilon}\right)^2\right) \tag{2.22}$$

This was speculated to be due to the difficulties associated with minimizing a fully non-convex function. Other robust penalty functions such as the Tukey's Biweight,

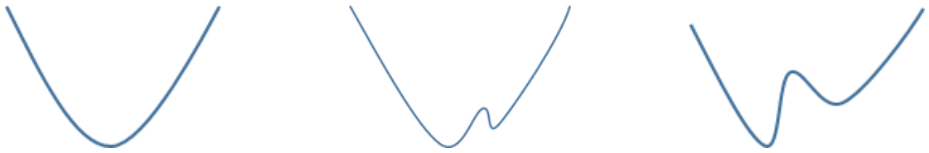

(a) (b) (c)

Figure 2.6: Illustration of GNC approach to minimize non-convex functions. (a) Convex function, (b) slightly non-convex function and (c) non-convex function.

Hampel, Andrew's Sine and Geman and McClure are available in Black and Rangarajan [90]. In general, robust penalty functions assign smaller weights to outlier data, hence reducing their influences on the final solutions and allowing for deviations in the data or regularization term. This has the effect of preventing over-smoothing of solutions, which is crucial in supersonic jet applications since the velocities associated with the jet shear layer is expected to vary drastically from supersonic to subsonic speeds. In addition, the flow turbulence is a big problem in image processing, as physical processes such as dissipation, pairing, turbulent structure-shock wave interaction, can all lead to disappearance/generation of structures across a schlieren image pair. Allowing abrupt variations in image velocities to occur is key to improving the robustness of optical flow.

Depending on the choice of robust penalty functions, a non-convex optimization problem can arise. To deal with the resulting non-convex optimization problem, multigrid [91] or multiscale [92] minimization strategies which operate in a discrete form may be adopted. Alternatively, the graduated non-convexity (GNC) [90, 93] approach can also be adopted, which operates on similar principles but in a

continuous form. GNC has been successfully implemented in similar applications and is a method that is related to graduated optimization. This is best elucidated in Figure 2.6. The non-convex problem (see Figure 2.6(c)) is first replaced by a convex problem (see Figure 2.6(a)). Solutions to the convex problem can be easily computed and is used as an initial guess for the next iteration, where a small component of the non-convex function is added to the convex function to obtain a function that becomes slightly non-convex (see Figure 2.6(b)). At the iteration where the slightly non-convex function is solved, a solution that is closer to the global solution can be obtained, which will again be used as an initial guess for the next iteration. The entire process repeats by adding a larger component of the non-convex function to the initial convex function in each iteration, such that the function that is minimized at each progressive iteration becomes increasingly non-convex. At the final iteration, the non-convex function itself is minimized with a good initial guess obtained from the solutions of the previous iteration. While GNC does not guarantee global solutions to non-convex problems, it usually performs well and gives reasonably good solution that is close to the global solution. It is noted that methods such as simulated annealing can also be used to deal with the non-convexity. However, in image processing where the problem is usually high dimensional (the number of dimensions increase with the image resolution), this is a computationally expensive approach that is generally not feasible.

Intensity changes across an image pair can sometimes be unavoidable. This problem is present in computer vision applications, whereby movement of shadows or reflections can lead to overall intensity changes across an image pair. In 2D particle-

images, out-of-plane particle motions can also lead to intensity changes across an image pair. A common method to circumvent this problem is to introduce an additional brightness gradient constancy [79] in the optical flow *model* to account for such effects. Nonetheless, such an approach leads to second derivatives of the image intensity which tends to be noisy. Robust penalty functions can also be used for the data term, which is able to relax the brightness constancy requirement as explained earlier. Alternatively, image pre-processing is also a potential solution that can be used to mitigate the problem. In the structure-texture decomposition method [94], images are decomposed into their corresponding structural (large scale details) and textural (fine scale details) part based on the Rudin-Osher-Fatemi (ROF) method [95]. The two components are then linearly combined with a user-defined blending factor, with larger weights typically assigned to the textural part. Optical flow is then performed on the post-processed images. There are also several other methods of image pre-processing which are more straightforward, such as the direct application of Gaussian or Laplacian pre-filters. These methods had been investigated in a parametric study [89, 96], and the results indicate that the structure-texture decomposition method has the best performance in terms of the accuracy of optical flow solutions, although the performance of simple image pre-filtering methods are also fairly competitive.

In terms of heuristic methods that can improve the optical flow algorithm, several studies [89, 94] have shown that it is worthwhile to make use of temporal averaging to compute the partial derivatives of image intensity at the expense of a small amount of effort and computational cost. While the use of temporal averaging is not

mathematically grounded, it improves optical flow accuracy presumably due to the "pre-conditioning" effect it has on the time dependent partial derivatives. Filters are also often used to remove spurious vectors in both optical flow and PIV post-processing. The commonly used filtering methods include median filtering, standard deviation filtering, as well as interpolations to replace "NaN" values. Though not explicitly reported, median filtering is used extensively in optical flow algorithms to remove spurious vectors. Nonetheless, this can result in smoother solutions which can be undesirable. To circumvent excessive smoothing, a weighted median filter based on spatial distance of neighbourhood pixels, colour-value distance, and occlusion state was introduced with very promising results in rigid body motion applications [89, 96]. In the case of schlieren images of supersonic jet flow whereby properties such as colour imaging or occlusion states are not physical, it might be worthwhile to consider a new type of weighted median filtering that is capable of preserving spatial structures of the flow features in the supersonic shear layer.

There have been a lot of studies performed on optical flow, evidenced by the extensive number of publications publicly available. An exhaustive review of the optical flow technique is outside the scope of the current thesis, and only the most important concepts relevant to the in-house optical flow algorithm developed for the current supersonic jet application is presented. Currently, most of the optical flow literature are in the context of computer vision problems and to the best of the author's knowledge, there has been little work published for SIVOF in supersonic jet applications.

2.3 Proper orthogonal decomposition

POD is a data-based analytical tool that is also known as principal component analysis, Karhunen–Loève transform or singular value decomposition depending on the field of application. The use of POD for fluid flow analysis was first introduced by Lumley [97] and subsequently improved upon by Sirovich [98] and Berkooz et al. [99] among many others. The approach decomposes the original flow field into spatially orthogonal modes ranked according to their energy contribution, allowing a high-dimensional fluid problem to be approximated with a lower dimension energy-efficient system. This allows useful information to be extracted from experimental or simulation data, and the most important and energetic structures that are dominant within the flow field can be identified and studied. There have been many successful applications of POD analysis in a wide variety of flow scenarios, such as flow past cylinders [100], turbulent jets [101-105], flow past backward-facing step [106], laminar separation bubble [107] and time-resolved schlieren images of a supersonic ramp nozzle [108].

To start off the explanation of the snapshot-based POD, it is first assumed that there is 2D velocity data available in the x-y plane. This can be obtained from experiments such as laser sheet planar PIV or SIV. Note that there is no requirement for the data to be time-resolved or sampled periodically. In order to perform POD analysis in the x-y plane, the instantaneous velocity fields (snapshots) are arranged in single column vector format to obtain the velocity matrix:

$$\boldsymbol{uv} = \begin{bmatrix} u_1^1 & \dots & u_1^n \\ \vdots & & \\ u_q^1 & & \\ v_1^1 & \dots & v_1^n \\ \vdots & & \\ v_q^1 & & \end{bmatrix}, \tag{2.23}$$

where q denotes the number of velocity vectors in a single snapshot, n denotes the total number of snapshots, u denotes the velocity in the x-direction and v denotes the velocity in the y-direction. The fluctuating matrix, $\widetilde{\boldsymbol{uv}}$, is then constructed by subtracting the time-averaged velocity field, $\overline{\boldsymbol{uv}}$, from $\boldsymbol{uv}$.

$$\widetilde{\boldsymbol{uv}} = \boldsymbol{uv} - \overline{\boldsymbol{uv}} \tag{2.24}$$

Next, the two-point correlation matrix is constructed by:

$$\boldsymbol{C_{n\times n}} = \widetilde{\boldsymbol{uv}}^{\boldsymbol{T}} \times \widetilde{\boldsymbol{uv}} \tag{2.25}$$

The eigenvectors $\boldsymbol{\Lambda}$ and eigenvalues $\boldsymbol{\lambda}$ may then be obtained by solving the eigenvalue problem:

$$\boldsymbol{C\Lambda} = \boldsymbol{\lambda\Lambda} \tag{2.26}$$

The eigenvalues represent the relative amount of energy associated with each eigenvector and can be used as a criterion to rank the eigenvectors. The spatially orthogonal POD modes $\boldsymbol{\phi}$ may then be obtained by:

$$\boldsymbol{\phi} = \widetilde{\boldsymbol{uv}} \times \boldsymbol{\Lambda} \tag{2.27}$$

Finally, the POD mode coefficients or temporal coefficients may be obtained by projecting the fluctuating velocity field on the POD modes:

$$\boldsymbol{a} = \widetilde{\boldsymbol{uv}}^{\boldsymbol{T}} \times \boldsymbol{\phi} \tag{2.28}$$

Order reduction can then be achieved by reconstructing the fluctuating flow field based on selected POD modes:

$$\widetilde{\boldsymbol{uv}}_{\boldsymbol{recon}} = \boldsymbol{\phi} \times \boldsymbol{a}^{\boldsymbol{T}} \tag{2.29}$$

By selecting POD modes that are the most representative of the flow field, this effectively filters out the influence of experimental noise and fine-scale turbulence. It is also possible to reconstruct the fluctuating flow field based on phase-sorted snapshots [100], to obtain phase-resolved fluctuating flow fields of a cyclical flow phenomenon.

For POD analysis in the x-z plane, the velocity matrix can be redefined by snapshots taken in the x-z plane:

$$\boldsymbol{uw} = \begin{bmatrix} u_1^1 & \dots & u_1^n \\ \vdots & & \\ u_q^1 & & \\ w_1^1 & \dots & w_1^n \\ \vdots & & \\ w_q^1 & & \end{bmatrix} \tag{2.30}$$

where *w* denotes the velocity in the z-direction. Subsequent procedures follow the same as described earlier and will be omitted for the sake of brevity.

Alternatively, POD can also be implemented by performing a singular value decomposition (SVD) on the data matrix, which has the advantage of better numerical stability. In this approach, the explanation will be presented by using a slightly different example for a more comprehensive understanding on the capabilities of POD. To start off, time-resolved schlieren images are assumed to be available from experiments, and POD can be performed on these images directly without any further image post-processing. For an image-series with n number of images, with each image comprising of q number of image pixels, the image matrix can be formulated as:

$$\boldsymbol{X}(j,t) = \begin{bmatrix} u_1^1 & \dots & u_1^n \\ \vdots & \ddots & \vdots \\ u_q^1 & \dots & u_q^n \end{bmatrix}, \tag{2.31}$$

where j denotes the pixel index and t denotes time. The fluctuating image matrix can then be obtained by:

$$\widetilde{\boldsymbol{X}} = \boldsymbol{X} - \overline{\boldsymbol{X}} \tag{2.32}$$

where the overbar denotes time-averaging. The economy-size SVD of the fluctuating image matrix is then obtained by

$$\widetilde{\boldsymbol{X}} = \boldsymbol{U}\boldsymbol{\Sigma}\boldsymbol{V}^*, \tag{2.33}$$

where $\boldsymbol{U}$ represents the POD modes, $\boldsymbol{\Sigma}$ is the diagonal matrix containing information on the eigenvalues, and $\boldsymbol{V}$ contains the temporal mode coefficients for the corresponding POD modes. Since time-resolved data is now available, it is possible

to perform spectral analysis and reveal additional information on selected POD modes [102, 109]. The dominant frequency associated with a particular POD mode can be obtained by performing Welch's power spectral density (PSD) estimate on a selected column vector of $\boldsymbol{V}$ (i.e. a selected POD mode). This can offer additional insight into the flow phenomenon associated with a selected POD mode.

Chapter 3 Experimental Setup

3.1 Supersonic jet apparatus

For the various studies presented in this thesis, all experiments were performed in an open-air blow-down supersonic cold jet facility situated in Temasek Laboratories, National University of Singapore. The same supersonic jet apparatus had been used in several past studies [27, 42, 110]. Dehumidified compressed air from air reservoirs capable of storing air at a maximum of 69 bars stagnation pressure is channelled through a series of valves and regulators to the settling chamber of the jet, where standard flow straighteners were employed to improve flow quality. A pressure tap located just before the flow exits the outlet of the settling chamber indicates the working conditions of the flow. Convergent-divergent circular nozzles of various designs can be refitted at the outlet to produce the supersonic jet flow, and the NPR is precisely controlled with a needle valve upstream of the settling chamber. The supersonic jet is designed to exhaust directly into the humidity- and temperature-regulated laboratory in a safe manner.

3.2 Test nozzles

Four different convergent-divergent circular nozzles were used throughout the various studies presented in this thesis, and their design details can be found in past studies which made use of the exact same nozzles [27, 41]. The circular-to-circular contraction section was designed with a contraction-ratio of 10.5. The divergent section was designed using a filleting method and have been demonstrated to display comparable flow characteristics as nozzles designed using the conventional

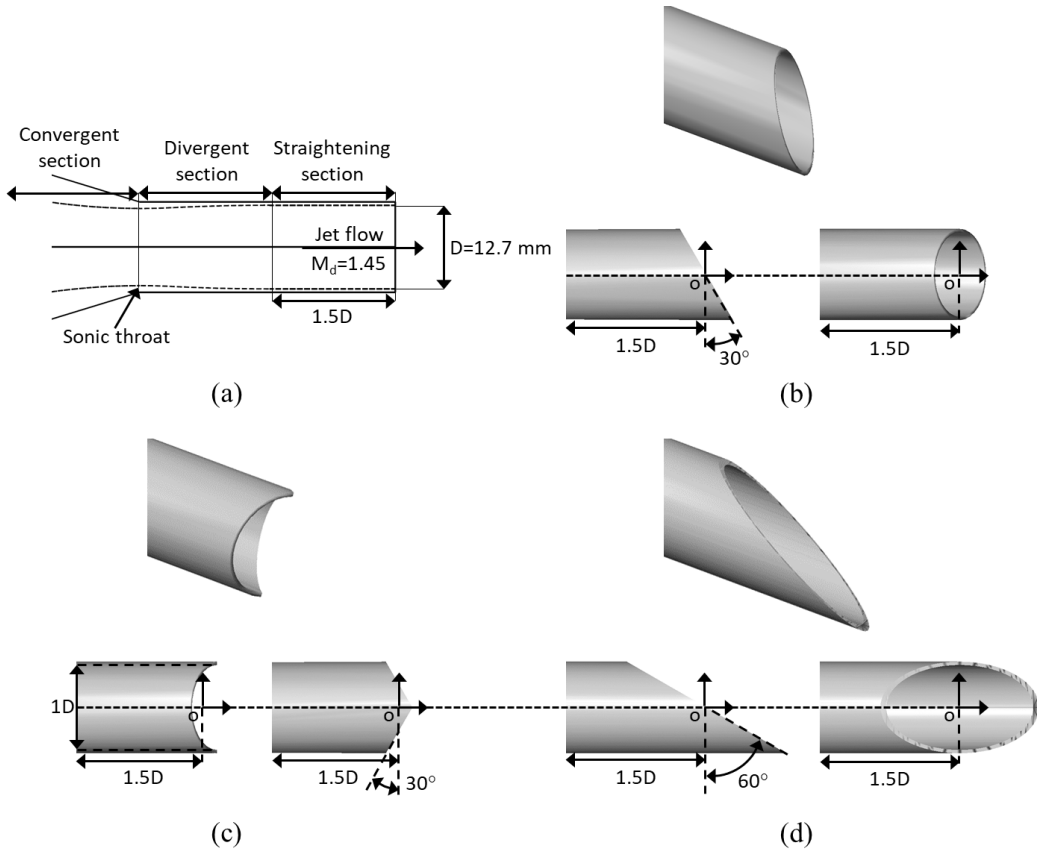

Figure 3.1: Detailed design schematics of the (a) baseline nozzle and the straightening sections of the (b) 30° bevelled, (c) 30° double-bevelled and (d) 60° bevelled nozzles

Method-of-Characteristics (MOC) technique [27]. At the end of the divergent section, the inner diameter is D=12.7 mm, and a straightening section of 1.5D length was added such that nozzle exit modifications can be implemented. The nozzle exit inner diameter is D=12.7 mm, and the lip thickness is 0.5 mm (approximately 0.04D). The design Mach number is M_d=1.45 for a perfectly expanded NPR of 3.4. All nozzles were fabricated out of stainless steel and well-polished to ensure low surface roughness. The nozzles consist of a circular baseline, a 30° bevelled, a 30° double-bevelled and a 60° bevelled nozzle as shown in Figure 3.1. For the sake of consistency, they were designed with the same mean axial length (i.e. defined here as

the average of the longest and shortest nozzle lengths) and jet origin position, o. Experiments were performed at four different NPR values; NPR=2.8 (over-expansion), NPR=3.4 (perfect expansion), NPR=4 and NPR=5 (moderate under-expansion).

3.3 Schlieren setup

All schlieren experiments were conducted using a modified double-mirror Z-type system [27] unless otherwise stated. A 200 W LED lamp provided broadband illumination and a slit in front served as an aperture to improve the spatial coherence of the light source. Two *f*/10, 3 m focal length, 300 mm diameter, parabolic, first surface mirrors reflected light into the test section and onto a knife-edge. Depending on the focus of the study, a vertical knife-edge can be used at the tangential focus to emphasize the shock systems and a horizontal knife-edge at the sagittal focus to emphasize the shear layers. Just after the knife-edge, a digital camera with lens is used to capture the schlieren image. A schematic of the experimental setup and images captured in the laboratory at two different viewpoints are presented in Figure 3.2.

The modified double-mirror Z-type system is preferred over the traditional double-mirror Z-type system due to advantages such as lower laboratory space requirements, flexibility in optimizing the experimental setup to achieve higher resolution images and allowing the camera to be focused on the jet axis during camera calibration procedures. Nonetheless, optical aberrations in the form of astigmatism tend to be higher for this experimental setup, due to slightly larger light ray angle of incidence

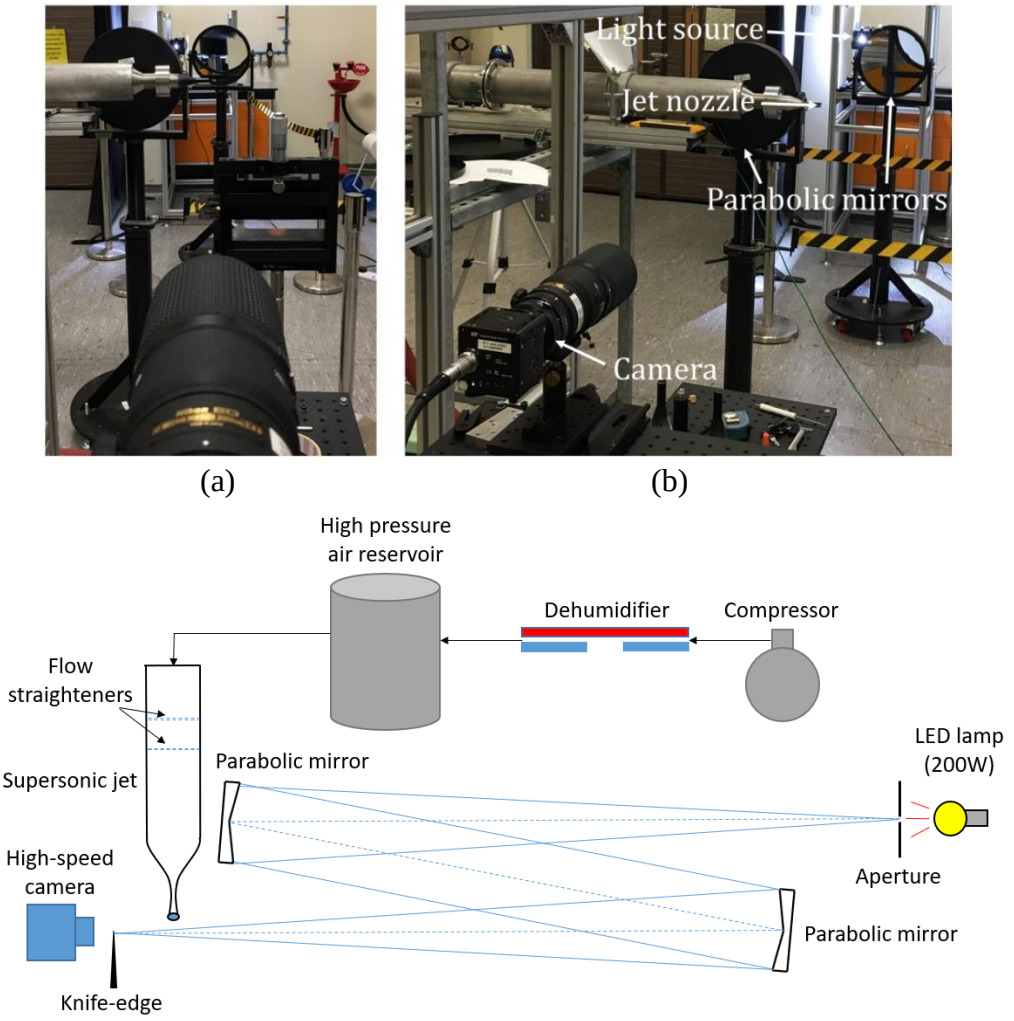

Figure 3.2: Modified Z-type double-mirror schlieren setup (a) viewpoint 1 (b) viewpoint 2 (c) schematic diagram

and reflection at the two parabolic mirrors. This was circumvented with the strict use of the correct knife-edge orientation at the sagittal and tangential focus, and the use of a circular aperture as knife-edge was mindfully avoided. The non-collimated light in the test section can also increase the errors and lead to unwanted distortions in the schlieren image. Fortunately, this effect is mitigated by the high f-number (*f*/10) of the parabolic mirrors and the comparatively small jet nozzle diameter of D=12.7 mm.

Chapter 4 A 3D Shock Wave Reconstruction Technique Based on the Voxel-based Visual Hull Method

4.1 Overview

The voxel-based VH technique takes advantage of the strong edge features commonly observed in schlieren images of shock waves to perform direct reconstruction. As such, it is possible to recover the 3D geometry of the shock waves without measuring a prior fluid property, such as velocity in velocimetry-based techniques or density in quantitative schlieren techniques. This approach offers several key advantages over current 3D techniques (tomographic PIV or tomographic BOS), including reductions in computational time, low hardware requirement during post-processing, inexpensive experimental setup, ease of implementation, as well as the ability to achieve high resolution and accurate reconstructed shocks even with limited number of cameras or using low resolution cameras. Not only does it extend the functionality of existing schlieren systems available in most compressible flow research laboratories to achieve quantifiable shock structure characteristics, it can also be used for challenging hypersonic flows or to provide experimental data to validate steady-state simulations (where unsteady viscous effects are not captured).

4.2 Methodology

The limitations of voxel-based VH technique have been highlighted in Section 2.1.2. To circumvent the limitations, the following two assumptions were made. (#1) For the current shock reconstruction problem, shock systems to be reconstructed do not have any hidden features in geometrical concavities when the cameras are positioned

orthogonal to the jet streamwise direction. (#2) Shock systems are steady, and the use of a single camera capturing images at n number of viewpoints during different time instances offers the same results as using n number of cameras capturing images simultaneously. The first assumption was found to be reasonable from preliminary inspections of the captured schlieren images, whereby shock waves that are to be reconstructed were observed to be geometrically convex. The observations are also consistent with previous supersonic jet studies conducted at the same flow conditions [27]. The second assumption was verified by capturing schlieren images at 1000 frames-per-second (FPS) and observing no change in the positions of the shocks.

In order to obtain the reconstructed shock wave, two pieces of information are required. The first piece of information is the camera matrix which fully describes the spatial orientation and position of n number of cameras, as well as the focal length, optical centre and pixel skewness (if any) of the image. More information will be provided on the camera matrix in Section 4.2.1. Ideally, the number of cameras at different viewing angles should be as large as possible as described in the Section 2.1.2, but is limited to 36 in the current application for practical reasons. The choice of 36 was deemed to be sufficient based on the final resolution and accuracy of the reconstructed shock waves. This implies that 36 camera matrices are required in order to project the visual cones from its corresponding silhouette images.

The second piece of information is the silhouette or binary images describing the shock waves. The image intensity can be written as:

$$I_{i=1,2\ldots n}(x,y) = \begin{cases} 1, & for\ pixels\ lying\ within\ shock\ wave \\ 0, & for\ pixels\ lying\ outside\ shock\ wave \end{cases} \quad (4.1)$$

where x and y represents the image coordinates, and the subscript i represents the index of the image captured at a particular viewing angle. Keeping in mind of assumption (#2) which was made earlier, a single camera can be used to capture all 36 schlieren images at different viewing angles at different time instances. With these two pieces of information, standard volume carving can then be carried out to obtain the reconstructed shock wave.

The experimental methodology to achieve direct shock wave reconstruction will be presented in the following three sub-sections. Section 4.2.1 will focus on the external camera calibration and numerical procedures involved in generating the semi-synthetic camera parameters. Section 4.2.2 will focus on the experimental procedures to capture optimal schlieren images, and the image processing procedures undertaken to process the schlieren images into silhouette images. Section 4.2.3 will provide more information on the final volume carving step to generate the visual hull output. A flowchart that summarises Section 4.2 is presented in Figure 4.1 to facilitate the discussion.

4.2.1 Semi-synthetic camera matrices

A pinhole camera model was used to provide the perspective transformation to relate world coordinates to image coordinates. This has been presented in Eq. (2.2) and is reproduced here again in Eq. (4.2) as it is central to the current discussion. The

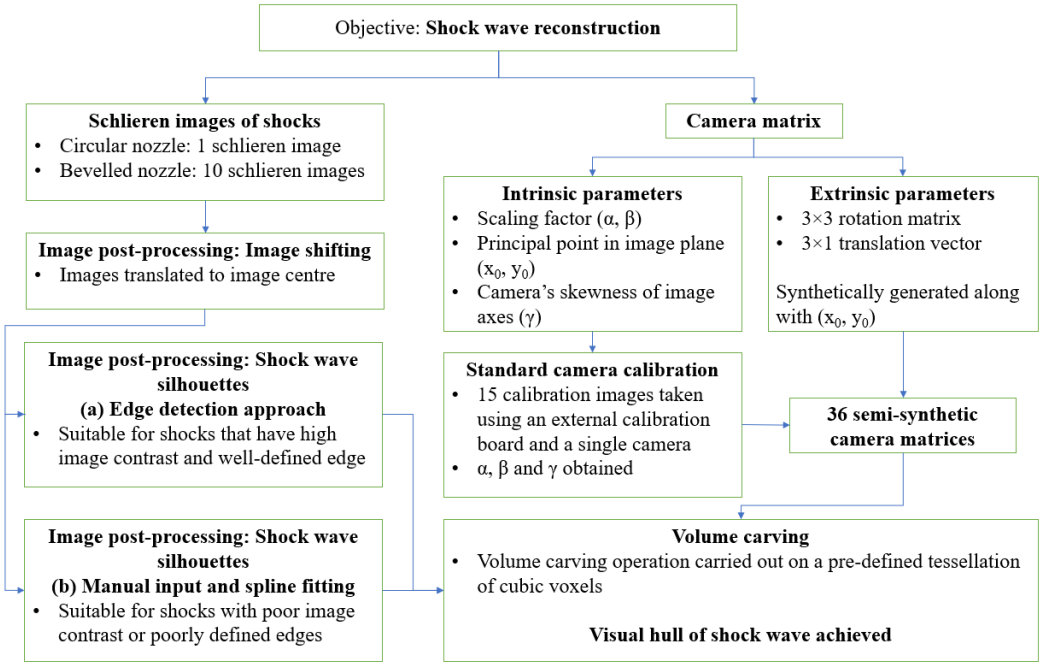

Figure 4.1: Flowchart of experimental methodology

camera matrix may be sub-divided into the intrinsic and extrinsic parameters as follows:

$$\underbrace{s\begin{bmatrix} x \\ y \\ 1 \end{bmatrix}}_{Image\ coordinates} = \underbrace{\begin{bmatrix} \alpha & \gamma & x_0 \\ 0 & \beta & y_0 \\ 0 & 0 & 1 \end{bmatrix}}_{Intrinsic\ parameters} \underbrace{\begin{bmatrix} r_{11} & r_{12} & r_{13} & t_1 \\ r_{21} & r_{22} & r_{23} & t_2 \\ r_{31} & r_{32} & r_{33} & t_3 \end{bmatrix}}_{Extrinsic\ parameters} \underbrace{\begin{bmatrix} X \\ Y \\ Z \\ 1 \end{bmatrix}}_{World\ coordinates} \tag{4.2}$$

The intrinsic parameters describe the geometrical properties of a camera, with skewness of image axes represented by (γ) and is often assumed to be zero. The principal point or image axes in the image plane is represented by (x_0, y_0) and is usually at the image centre. The focal length expressed in pixel units for image coordinates (x, y) is represented by (α, β), and should have the same value theoretically. In practice, they may differ due to reasons such as camera lens

distortion, camera calibration errors or anamorphic format image compression. The extrinsic parameters define the position and orientation of the real world relative to the camera, with the orientation described by the 3 × 3 rotation matrix and the position described by the 3 × 1 translation vector. Essentially, the camera matrix serves as a mapping function to relate 3D world coordinates to the 2D image coordinates. To obtain the solutions to the intrinsic and extrinsic camera parameters, an external calibration pattern with known dimensions is typically used along with standard nonlinear least-squares minimization Levenberg–Marquardt algorithm [111], as presented in Section 2.1.3.

However, the use of the traditional camera calibration technique is not suitable for the current application. This was first discovered during initial testing, when a 0.9 mm diameter Mach disk of an over-expanded jet at NPR=2.8 failed to be reconstructed. The extrinsic parameters were found to be lacking in accuracy, in part due to the miniature size of the reconstructed VH relative to the large projection distance of the camera to the VH, in part due to practical limitations of existing camera calibration procedures. In this study, the diameter of the Mach disk is less than 1 mm, while the projection distance is over 700 mm. Hence, minute angular misalignments in the camera's orientation or position introduced by errors in the extrinsic parameters were able to contribute significantly to the final reconstructed VH. The use of a very small calibration pattern intended to maximise schlieren image resolution further exacerbated the problem of insufficient accuracy in the extrinsic parameters.

To obtain highly accurate camera parameters suitable for the current application, the intrinsic parameters γ, α and β were obtained using standard external camera calibration techniques while all other remaining camera parameters were synthetically generated. The synthetic extrinsic parameters were artificially generated to ensure perfect geometrical alignment of the cameras relative to the jet test section, hence overcoming the challenges faced during the initial testing. Additionally, there is also a need to control the principal point (x_0, y_0) although it belongs to the intrinsic parameters. This will be further discussed in Section 4.2.2 due to its relationship with the image processing procedures. Since the intrinsic parameters are a property of the camera and lens, the same intrinsic parameters can be used throughout all 36 camera matrices.

With the use of synthetically generated extrinsic parameters, this means the cameras have been mathematically shifted from their original positions and orientations, and there are certain implications on the captured images that one must be cautious with. In real-world photography, light-carrying information of a 3D scene enters a camera and is recorded on a charge-coupled device (CCD) as a 2D image. A shift in the camera position or orientation will inevitably lead to a change in the field-of-view, as well as changes in scene details such as object occlusion, object shadowing, reflectance, etc. Effectively, this leads to a very different set of information that should have been recorded by the shifted camera. Images will require more than simple transformations in the form of scaling, rotation, or translation in order to correct them such that they can correspond to the new position and orientation of the shifted camera. However, the additional information to make the necessary

correction is not available, as the original 2D image does not have the capability to fully capture information of a 3D scene.

Fortunately, it turns out that this constraint is not applicable in the context of schlieren imagery. In a schlieren setup, light rays are projected from a mirror or lens into the camera, and the information recorded by the CCD is an integration of the density variations along the entire light path. Assuming that there are only slight changes in the camera position and orientation, the schlieren light rays should still be able to project onto the camera's CCD, and the information recorded by the camera will not change since it is dependent only on the amount of refraction the light rays undergo. Hence, this relaxes the relationship between the extrinsic camera parameters and the captured images, thus permitting the use of synthetically generated extrinsic parameters in the current application. It should be highlighted that while this approach takes advantage of the observation that the shock wave information in the schlieren images are invariant to slight changes in the camera orientation and position, the exact location where the image forms on the CCD will still be affected by the change in extrinsic parameters. Hence, there remains a need to carry out image processing in terms of image translation, and adjustment of the principal point in the intrinsic parameters.

4.2.1.1 Intrinsic parameters from external camera calibration

The intrinsic parameters γ, α and β were obtained by implementing external camera calibration technique using MATLAB's camera calibrator and a Bespoke external calibration board, where the latter consisted of a 7 × 10 checkerboard pattern with 2.14 mm squares prepared at a resolution of 1200 dpi. This board was positioned at

the nozzle exit where the strongest shock waves were produced. A reference rotational angle of 0˚ was defined such that the board was squarely facing the camera, with the rotational axis of the board aligned with the jet axis. The alignment was ensured with the help of a self-levelling laser device. The board was rotated from -70˚ to 70˚ at regular intervals of 10˚, hence capturing 15 calibration images. The precise rotation was achieved by mounting the calibration board on an optomechanical instrument (Thorlabs RP01), which has graduation marks at 2° increment. The captured images were then post-processed to obtain the initial camera parameters, with an overall mean error of 0.63 pixels. The intrinsic parameters were retained while the extrinsic parameters were discarded.

It should be highlighted that since the purpose of the external calibration conducted here is to obtain only the intrinsic parameters (the extrinsic parameters will be synthetically generated), the described procedure regarding the alignment and precise rotation of the calibration board does not have to be strictly adhered to. However, closely following the procedures as described above instead of choosing random angles to position the calibration board were found to be optimal in ensuring alignment of the board's rotational axis with the jet axis across all 15 calibration images, thus ensuring that the focal lengths (α, β) obtained are as accurate and consistent as possible.

For the case of the initial testing first mentioned in Section 4.2.1 whereby attempts to recover the Mach disk were unsuccessful, the full camera matrices (both intrinsic and extrinsic parameters) were obtained purely from external camera calibration. Hence, the procedures as described above were strictly followed to obtain camera matrices

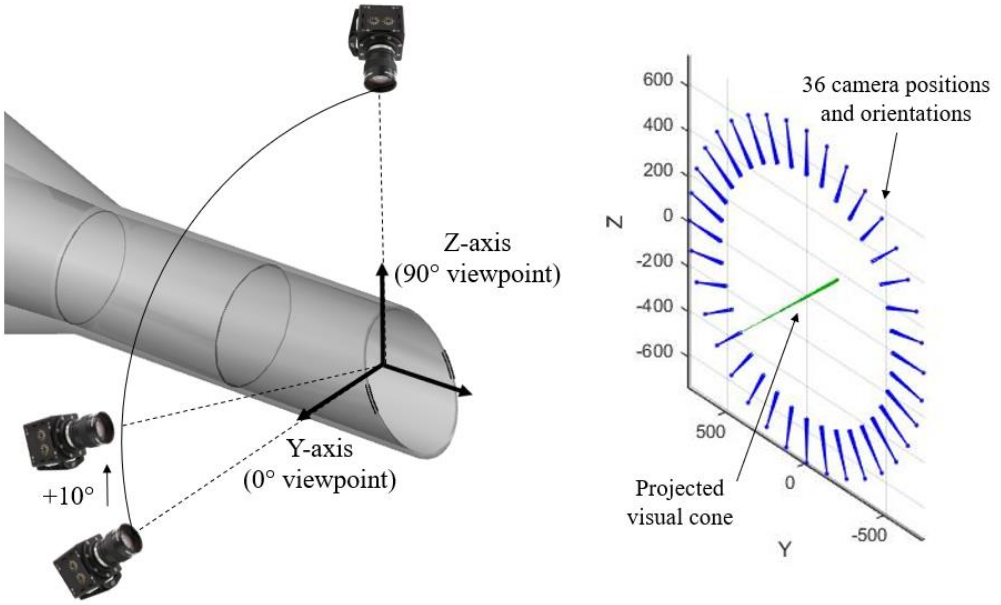

(a) (b)

Figure 4.2: Positions and orientations of the cameras generated with synthetic extrinsic parameters (a) cameras pointing towards bevelled jet axis (b) cameras forming a circle on YZ-plane

that are as accurate as possible. In theory, keeping the camera stationary while rotating the calibration board at regular intervals of 10˚ (camera-centric view) is equivalent to keeping the calibration board stationary and moving the camera at 10˚ interval around the azimuthal position of the jet (pattern-centric view). Following the procedures as described above allowed camera matrices representing cameras at multiple viewpoints to be obtained.

4.2.1.2 Synthetic extrinsic parameters

The locations and orientations of the 36 cameras that were synthetically generated is shown in Figure 4.2, with Figure 4.2(a) illustrating cameras in the first quadrant pointing towards the jet axis. Figure 4.2(b) illustrates all 36 cameras lying on the perimeter of a perfect circle in a 2D YZ-plane, with the radius of the circle

representing the focal length of the camera in world coordinates. The centre of the circle is coincident with the jet axis. The focal length *f* can be obtained by:

$$f = \frac{\alpha + \beta}{2} \times M \tag{4.3}$$

where M represents the pixel-to-world magnification factor obtained from the calibration board. The rotation matrix $\boldsymbol{R}$ and translation vector $\boldsymbol{T}$ were synthetically generated with the following equations:

$$\boldsymbol{R_i} = \begin{bmatrix} 1 & 0 & 0 \\ 0 & \cos(\theta_{x,i}) & -\sin(\theta_{x,i}) \\ 0 & \sin(\theta_{x,i}) & \cos(\theta_{x,i}) \end{bmatrix} \tag{4.4}$$

$$\boldsymbol{T_i} = -\boldsymbol{R_i} \times \boldsymbol{C_i} \tag{4.5}$$

where $\theta_{x,i}$ represents the azimuthal rotational angle and $\boldsymbol{C_i}$ represents the column vector containing the camera position in world coordinates (X, Y, Z). The first camera position was defined at $C_1 = (0, f, 0)$, with $\theta_{x,1} = \frac{\pi}{2}$. Subsequent camera positions and orientations were then obtained by numerically rotating the first camera about the streamwise direction, or vector (1, 0, 0), by 10˚ incrementally. Mathematically, this is the same as performing a rotation of a 3D point about the X-axis. In equation form, this can be written as:

$$\theta_{x,i+1} = \theta_{x,i} + 10° \times \frac{\pi}{180°} \tag{4.6}$$

$$\boldsymbol{C_{i+1}} = \begin{bmatrix} 1 & 0 & 0 \\ 0 & 0.9848 & 0.1736 \\ 0 & -0.1736 & 0.9848 \end{bmatrix} \times \boldsymbol{C_i} \tag{4.7}$$

where the 3×3 matrix in Eq. (4.7) can be obtained by taking the transpose of Eq. (4.4) and using 10° rotation angle. Thirty-six cameras with precisely known positions and orientations can then be generated, as shown in Figure 4.2(b).

4.2.2 Silhouette images generation

4.2.2.1 Schlieren images

Schlieren experiments were conducted using the modified double-mirror Z-type system and supersonic jet apparatus presented in Chapter 3. An IDT NX4-S1 camera with a Nikon AF Micro-Nikkor 200 mm f/4D IF-ED lens was used to capture schlieren images at 1024px × 1024px resolution and 1000 FPS. All experiments were conducted at under-expanded exhaust conditions at NPR=4 and 5 for the baseline circular and 30° bevelled nozzle [27].

In Figure 4.3, contrast and brightness enhanced schlieren images of the circular jet at NPR=5 captured during initial testing are shown. Figure 4.3(a), Figure 4.3(b) and Figure 4.3(c) show the images captured using the horizontal knife-edge (HKE) placed at the sagittal focus, with exposure time increasing from 0.77 µs to 30 µs. Figure 4.3(d) and Figure 4.3(e) shows the images captured using the vertical knife-edge (VKE) placed at the tangential focus, with an exposure time of 30 µs and 494 µs respectively. Figure 4.3(f) shows the picture of a shadowgraph taken with an exposure time of 12 µs. Optimal images for the current application were found to be taken by using a long exposure time of over 400 µs and with a vertical knife-edge.

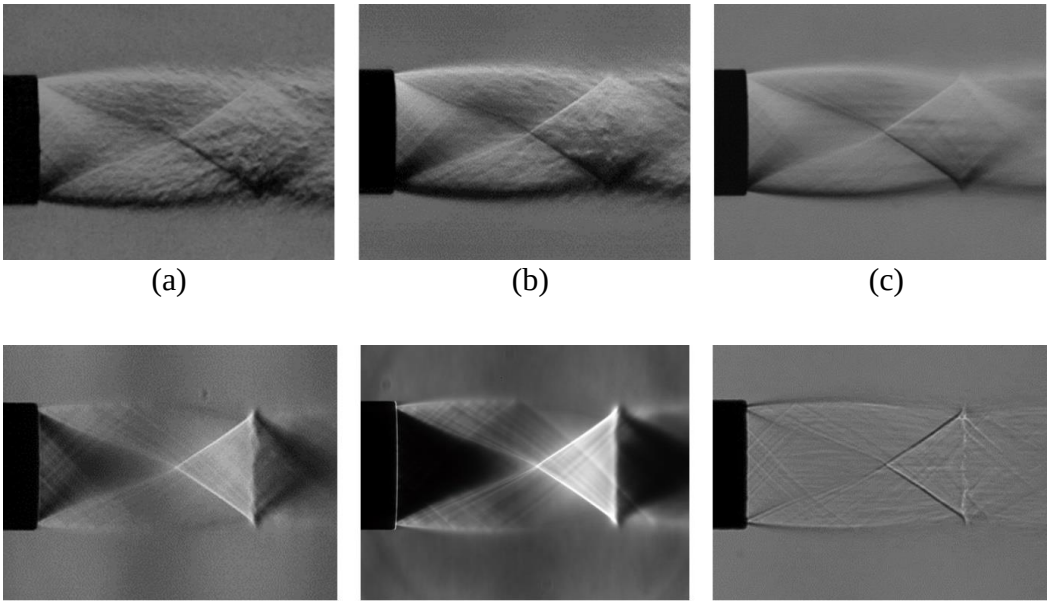

Figure 4.3: Enhanced images of the circular jet at NPR=5, captured with (a) HKE schlieren, 0.77 μs, (b) HKE schlieren, 1 μs, (c) HKE schlieren, 30 μs, (d) VKE schlieren, 30 μs, (e) VKE schlieren, 494 μs, and (f) shadowgraph, 12 μs image exposure time

The use of a longer exposure time was able to reduce the influence of turbulent structures, and it also allows a much greater cut-off at the knife-edge which creates over-ranging of the expansion and compression zones. This greatly improved the contrast of the intercepting and reflected shocks, while also reducing visibility of unwanted faint shocks that were otherwise visible in Figure 4.3(d) and Figure 4.3(f). In this study, all schlieren images were captured with an exposure time of over 400 μs, with the vertical knife-edge adjusted to about 80% cut-off.

For the reconstruction, 36 images captured at azimuthal angular interval of 10° are required in order to provide the silhouette images for the 36 semi-synthetic camera matrices. However, this was not necessary for the baseline nozzle where the shock systems were expected to be axisymmetric. The axisymmetric property of the

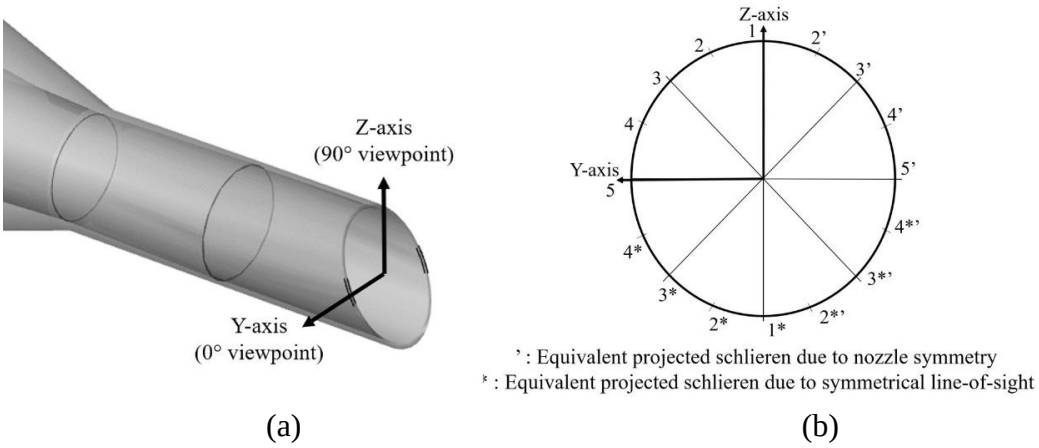

Figure 4.4: (a) Bevelled nozzle drawing with azimuthal angle defined and (b) illustration of equivalent schlieren projection views

baseline shock systems was verified by taking schlieren images of the shock structures from multiple different viewing angles during the study. Specific to the baseline nozzle, only a single image was taken from one viewpoint. Once the image has been processed to generate the silhouette image, it was duplicated and used as the silhouette images for all 36 viewpoints. For the bevelled nozzles, nozzle symmetry about the Z-axis and schlieren line-of-sight symmetry effectively limits the angles of unique schlieren's projected views to a single 90-degree quadrant. A schematic to illustrate this property is shown in Figure 4.4. Hence, 10 schlieren images were captured at regular intervals of 10°, within the range of [0, 90] degrees. This was achieved by rotating the nozzle with the help of a Bespoke circular ruler fixed onto the circular bracket clamping the detachable nozzle in position. The error associated with the azimuthal rotational angle was estimated to be about 1° based on the Bespoke circular ruler. With every nozzle rotation of 10°, the reflection point of the bevelled jet operated at NPR=5 shifted by about 4 pixels. Hence, a rotational error of 1°

translates to a negligible image pixel error of 0.4 pixels. The acquired schlieren images were post-processed into silhouette images, before being reflected about both symmetry axis to obtain 36 silhouette images in the range of [0, 360] degrees.

4.2.2.2 Image post-processing procedures

With the use of synthetic extrinsic parameters, cameras are mathematically enforced to point straight at the jet axis. Consequently, this would mean that for the captured images, the image row in which the jet axis can be located should be at the image centre. Furthermore, the tip of the nozzle should appear in the same image column across all captured images. Hence, all captured schlieren images were translated by using the nozzle outer diameter and the nozzle tip as reference, with zeroes padding the shifted image borders. Because of the image translation, the principal point (x_0, y_0) of all 36 camera matrices was redefined at the image centre with pixel location of (512.5, 512.5).

Before the schlieren images can be used together with the camera matrices to perform reconstruction, they have to be processed into silhouette images first. The procedure to process the schlieren images into silhouette images is dependent on the characteristics of the schlieren images captured. In Figure 4.5(a), the circular jet operated at NPR=5 shows excellent contrast of shock waves' pixel intensity relative to the background, with well-defined shock wave edges. For such images, the silhouette images were generated using the edge detection method, which was found to be robust when applied to schlieren images with these characteristics.

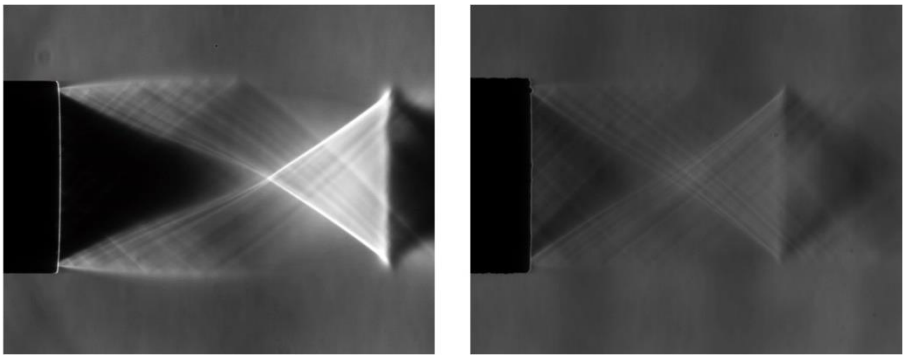

(a) (b)

Figure 4.5: Schlieren images of circular baseline jet operated at (a) NPR=5 and (b) NPR=4

When the circular jet was operated at NPR=4, the shock structures are much weaker, and it was not possible for the schlieren images shown in Figure 4.5(b) to attain the same level of image contrast shown in Figure 4.5(a). While the circular jet operated at NPR=4 shows shock wave edges which are still sufficiently strong to enable detection by the edge detection method, the presence of weaker shocks with similar edge contrast throughout the entire flow region effectively decreases the signal to noise ratio (SNR). This leads to spurious edges being detected but cannot be filtered out efficiently, hence reducing the reliability of the edge detection method in such a scenario. For images where the edge detection fails, the algorithm switches to a manual spline fitting method.

a) <u>Edge detection method</u>

In the edge detection approach, schlieren images were processed with MATLAB's edge detection using the Canny method. The Canny edge detection method is one of the basic building blocks in image processing and consist of three main steps. First, a Gaussian filter is applied to smooth the image and reduce image noise. Next, the

(a) (b) (c)

Figure 4.6: Shock structures of an under-expanded baseline jet (NPR=4) (a) schlieren (b) noisy edge map (c) silhouette of shock wave

intensity gradient is computed, where edges can be identified based on the local maxima of the intensity gradient. Finally, two thresholds are used to detect strong and weak edges, and weak edges are included in the output if they are connected to strong edges. Since noise often manifests as weak edges, the extra criteria to accept weak edges improves the robustness of Canny method, increasing the likelihood to detect true weak edges. The Canny method was selected because it performed better than other methods available in MATLAB's image processing toolbox, which includes the Sobel, Preweitt and Roberts method. It is also robust to image translation, rotation, or other forms of geometrical transformation.

The edge detection function converts schlieren images as shown in Figure 4.6(a) into obtain edge maps (or binary images), shown in Figure 4.6(b). Unlike edge detection of the nozzle which was relatively straightforward due to the strong contrast between the nozzle outline and the schlieren background, the edge map which includes the shock wave edges were usually much noisier due to the use of a weaker edge detection threshold, and de-noising was necessary before silhouette images (see

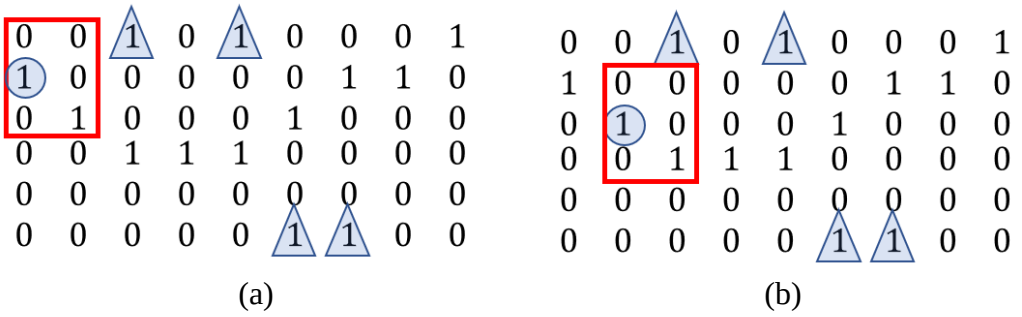

Figure 4.7: Image intensity and the window search process at (a) current iteration (b) next iteration

Figure 4.6(c)) can be generated. To achieve this, an area opening operation which removes connected components with pixels less than a specified threshold was performed. This essentially acts like a filter that can remove the low wavelength noise, with the resulting image consisting of the shock wave edges and a small number of high wavelength noise – long continuous edges scattered in the background. The remaining noisy edges were difficult to remove efficiently using filters due to their strong similarity with the shock wave edges, sensitivity to Canny edge function's input parameters, and low robustness when handling schlieren images across different test cases.

To identify the pixel locations of the shock wave edges, a 2×7 pixels vertical window was initialized on the shock wave edge, and dynamically shifted to search neighbouring pixels for shock wave edges. Pixels of non-zero value that managed to enter the window during the search was accepted as part of the shock wave edge, with the new-found pixel location used in the next iteration to initialize the next window. The stoppage criterion was set at the first occurrence of either 5000 iterations or arrival at the nozzle edges, which was pre-determined earlier. The vertical

rectangular window was chosen to accommodate for shock waves with large angles. Removal of noise during the area opening operation and the choice of a relatively small window ensured noisy edges did not enter the window during the window search process. A simple illustration to describe this process is provided in Figure 4.7, whereby a 2×3 pixels vertical window is represented by the red rectangle, pixel intensity of 1 represents the shock wave edge, pixel intensity of 1 with the blue triangle represents unwanted image noise, and the blue circle represents the pixel location used to initialize the search window at the current iteration. In Figure 4.7(a), a non-zero value pixel manages to enter the window at the bottom right corner and is thus labelled and recorded as part of the shock wave edge. This pixel then becomes the new location to initialize the search window at the next iteration, as illustrated by Figure 4.7(b). The process repeats itself until the stoppage criteria is fulfilled.

b) <u>Manual spline fitting method</u>

In the manual spline fitting approach, approximately 5 to 9 points along the shock wave in the schlieren image were manually selected, thus allowing linear or Hermite's cubic interpolative splines approximating the shock waves to be fitted automatically. The linear splines were created by using the following parametric equations:

$$y_{interpolated}^{(q)} = y_q + \left(y_{q+1} - y_q\right) t \tag{4.8}$$

$$x_{interpolated}^{(q)} = x_q + \left(x_{q+1} - x_q\right) t \tag{4.9}$$

where t is the parametric parameter, (x_q, y_q) represents the coordinates of the q^{th} selected data point, and the superscript (q) represents the spline segment index.

Following the same notation, the cubic splines were created with the following parametric equations:

$$y_{interpolated}^{(q)} = A_y^{(q)} t^3 + B_y^{(q)} t^2 + C_y^{(q)} t + D_y^{(q)} \tag{4.10}$$

$$x_{interpolated}^{(q)} = A_x^{(q)} t^3 + B_x^{(q)} t^2 + C_x^{(q)} t + D_x^{(q)} \tag{4.11}$$

For each cubic spline segment, the parameters $A_x^{(q)}, B_x^{(q)}, C_x^{(q)}$ and $D_x^{(q)}$ can be determined by using the Hermite matrix:

$$\begin{bmatrix} A_x^{(q)} \\ B_x^{(q)} \\ C_x^{(q)} \\ D_x^{(q)} \end{bmatrix} = \begin{bmatrix} 2 & -2 & 1 & 1 \\ -3 & 3 & -2 & -1 \\ 0 & 0 & 1 & 0 \\ 1 & 0 & 0 & 0 \end{bmatrix} \begin{bmatrix} x_q \\ x_{q+1} \\ x_q{}' \\ x_{q+1}{}' \end{bmatrix} \tag{4.12}$$

And the first order derivatives can be obtained by solving the following equation:

$$\begin{bmatrix} 1 & 0 & 0 & 0 & & 0 & 0 & 0 & 0 \\ 1 & 4 & 1 & 0 & \cdots & 0 & 0 & 0 & 0 \\ 0 & 1 & 4 & 1 & & 0 & 0 & 0 & 0 \\ 0 & 0 & 1 & 4 & & 0 & 0 & 0 & 0 \\ & & \vdots & & \ddots & & & \vdots & \\ 0 & 0 & 0 & 0 & & 4 & 1 & 0 & 0 \\ 0 & 0 & 0 & 0 & & 1 & 4 & 1 & 0 \\ 0 & 0 & 0 & 0 & \cdots & 0 & 1 & 4 & 1 \\ 0 & 0 & 0 & 0 & & 0 & 0 & 0 & 1 \end{bmatrix} \begin{bmatrix} x_0' \\ x_1' \\ x_2' \\ \vdots \\ \vdots \\ x_{J-1}' \\ x_J' \end{bmatrix} = \begin{bmatrix} 1 \\ 3(x_2 - x_0) \\ 3(x_3 - x_1) \\ \vdots \\ \vdots \\ 3(x_J - x_{J-2}) \\ 1 \end{bmatrix} \tag{4.13}$$

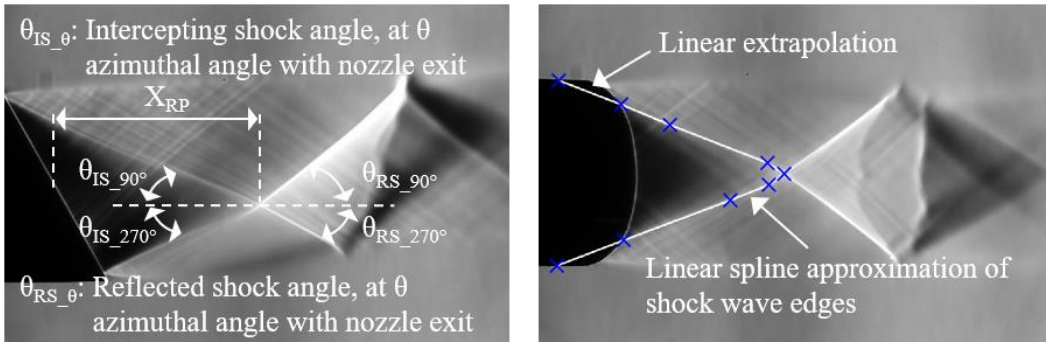

(a) (b)

Figure 4.8: Shock structures of an under-expanded bevelled jet (NPR=5) (a) schlieren at 0° viewpoint (b) schlieren at 90° viewpoint with linear spline approximating shock wave

where *J* represents the total number of data points. The parameters A_y, B_y, C_y and D_y can be obtained with Eq. (4.12) and (4.13) using the same procedure, hence details are omitted for the sake of brevity.

The pixel locations of these fitted splines approximating the shock waves may then be extracted. An illustration of a linear spline fitted to approximate the intercepting shock edges from the bevelled nozzle is shown in Figure 4.8(b). While the manual spline fitting method may appear primitive as compared to the fully automated edge detection method, it is unconditionally robust and still offers accurate reconstruction results. Both edge detection and manual spline fitting techniques were used interchangeably to process the schlieren images.

From Figure 4.8(b), there is also an illustration of the shock wave edges being linearly extrapolated to the nozzle outer diameters. The bevelled nozzle incurred in the issue of information loss for shock waves lying upstream of the nozzle tip, due to schlieren line-of-sight blockage by the nozzle. To circumvent this problem and ensure the

reconstructed shock cones are representative of the actual shock systems, local gradients were calculated, and this information was then used to linearly extrapolate the shocks towards the nozzle.

With the shock wave edges identified through either the edge detection or the manual spline fitting method, the silhouette image as shown in Figure 4.6(c) was then created by filling the pixels of the enclosed area bounded by the shock waves' edges with pixel value of 1. The filling operation was conducted by performing a row-wise conversion of pixel value from 0 to 1, with the shock wave edges used to initialize the operation.

4.2.3 Volume carving

An initial bounding box with 30 million voxels was defined, and standard volume carving was carried out based on those parameters. Every single voxel in the initial bounding box was sampled and subjected to a binary decision, and voxels lying outside any of the 36 projected visual cones were rejected, with the remaining voxels constituting the visual hull that represents the shock structures. For reference, the final voxels count typically ranged from 10% to 15% of the starting number of voxels, and the cubic voxel resolution for the NPR=4 baseline jet is 0.044 mm. Since only the shock surfaces are of interest, they were extracted from the reconstructed VH and plotted with the CAD drawings of the nozzles. The extraction was achieved by sorting the VH's voxels into multiple XZ slices, and then searching each XZ slice for voxels with the maximum (or minimum) x-coordinate value to obtain the shock surface of the intercepting shock (or reflected shock). Here, it must be highlighted that the intercepting and reflected shocks were reconstructed separately, hence the

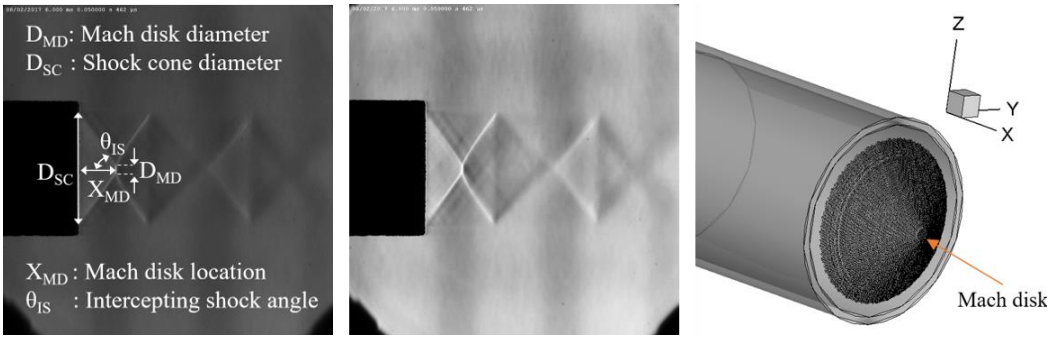

Figure 4.9: Shock structures of an over-expanded baseline jet (NPR=2.8) (a) schlieren (b) contrast-enhanced schlieren (c) reconstructed results

search criterion would be able to yield the correct shock surfaces. The in-house shock reconstruction algorithm was developed based on a standard volume carving visual hull code [112], and image processing was carried out on a laptop with 8 GB memory and an Intel® Core™ i7-5500U 2.4 GHz processor. For 36 projected visual cones and 30 million starting voxels, the average computation time was less than 5 minutes.

4.3 Results and discussions

The NPR=2.8 baseline jet which was used to produce the 0.9 mm diameter Mach disk for developing and refining the algorithm is presented in Figure 4.9, while Table 4.1 provides the corresponding details of selected key parameters. Although over-expanded jet is not the focus of this study, the code was developed by using the Mach disk as a gauge for the required level of accuracy and resolution in the reconstruction procedure. Hence, these details are provided for the purpose of completing the study and explanation in the earlier section. Details on the procedure to obtain measurements from the schlieren images can be found in Section 4.3.2.

Table 4.1: Reconstructed shock cone key parameters for NPR=2.8 baseline jet

	Schlieren images	Reconstructed shock cone
Baseline nozzle, over-expanded flow condition (NPR=2.8)		
D_{MD}	0.92 mm	0.90 mm
D_{SC}	11.25 mm	10.93 mm
X_{MD}	3.79 mm	3.77 mm
θ_{IS}	53.6°	53.1°

4.3.1 General observations

The reconstructed shock structures for the baseline jet at NPR=4 and 5 are presented in Figure 4.10 and Figure 4.11 while the results for the bevelled jets at NPR=4 and 5 are shown in Figure 4.12 and Figure 4.13 respectively. Bevelling the nozzle shifts the reflection point towards the longer lip of the nozzle, as observed in the results for both NPR=4 and 5 in Figure 4.12 and Figure 4.13 respectively. Intercepting shocks are formed when compression waves coalesce, and the angle at which the intercepting shock forms is largely dependent on the initial expansion fan angles as well as the constant pressure streamline. Bevelling of the nozzle and allowing the expansion fan to form earlier near the shorter lip of the nozzle appears to have altered the conditions, leading to a smaller intercepting shock angle from the shorter lip. The converse holds true for the intercepting shock from the longer lip. Coupled with the different axial positions in which the intercepting shocks originated from, a nett effect of the reflection point sitting closer to the longer lip of the nozzle is observed.

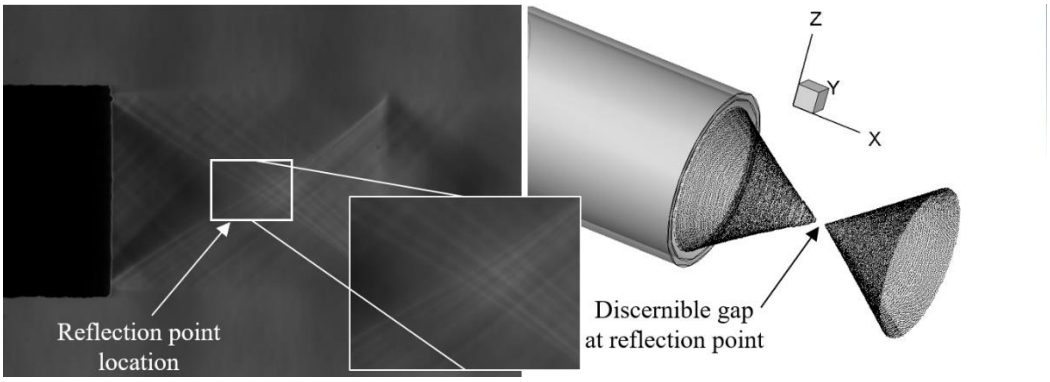

(a) (b)

Figure 4.10: Baseline nozzle's shock structures at NPR=4 (a) schlieren (b) reconstructed shock

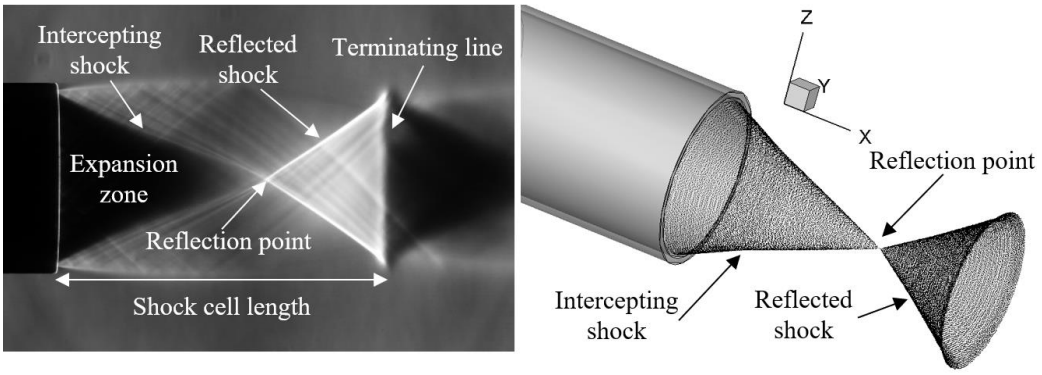

(a) (b)

Figure 4.11: Baseline nozzle's shock structures at NPR=5 (a) schlieren (b) reconstructed shock

At the reflection point location, the intercepting and reflected shocks appear to be disjointed in the NPR=4 reconstruction results of both nozzles, as shown in Figure 4.10(b) and Figure 4.12(b). This is a non-physical observation and can be attributed to the nature of the schlieren images captured during NPR=4 operating conditions. The schlieren image of the NPR=4 baseline nozzle presented in Figure 4.10(a) shows the presence of many additional edge features near the reflection point location. For the NPR=4 bevelled nozzle case, the schlieren image as shown in Figure 4.12(a)

shows the presence of an extra edge line emanating from the shorter nozzle lips (or 90° azimuthal angle of the nozzle exit), running parallel to the intercepting shock, and extending all the way pass the reflection point location to the reflected shock. These types of edge features contribute to ambiguities and inaccuracies during the shock wave silhouette image generation process, hence resulting in a disconnection of the intercepting and reflected shocks in the final reconstructed shock structures.

In contrast, for the NPR=5 baseline and bevelled jets, the schlieren image in Figure 4.11(a), Figure 4.13(a) and Figure 4.13(c) all display strong contrast and clearly defined edges, hence reconstructed results do not encounter the same issues experienced by the NPR=4 baseline and bevelled jets. With an increase in NPR value, the intercepting shock angle decreases, and the reflection point shifts further downstream. Density variations across shock waves become stronger, allowing the experimental setup to be optimally adjusted to obtain schlieren images with better shock wave contrast and clearer edges that are most suitable for the reconstruction.

For the same NPR value across the two nozzles, the bevelled nozzle appears to have missing shock surfaces near the shorter lip of the nozzle, as shown in Figure 4.12 and Figure 4.13. This can be attributed to the bevelled nozzle line-of-sight blockage problem and was heuristically mitigated by linear extrapolation of shock wave edge maps as explained and shown in an earlier section. Striations may also be observed in the reconstructed cones and can be attributed to the nature of the space discretization techniques. To a limited extent, these effects may be reduced with the use of a higher resolution camera to create higher resolution silhouette images, along with pre-defining higher voxel resolution in the initial bounding box. However, this

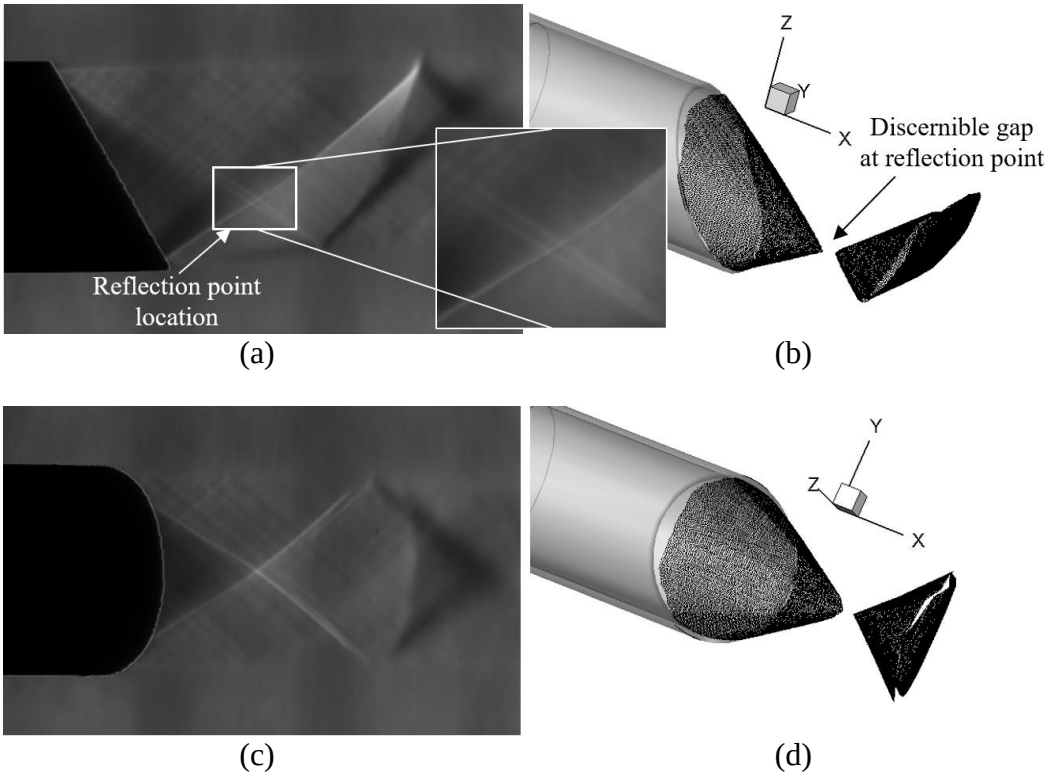

Figure 4.12: Bevelled nozzle's shock structures at NPR=4 (a) schlieren at 0° viewpoint (b) reconstructed shock (c) schlieren at 90° viewpoint (d) reconstructed shock

comes with heavier computational cost. For the current application, these options were not necessary as the prevailing resolution is sufficient and any further increment in resolution will not yield additional insights into the flow behaviour.

4.3.2 Quantitative evaluations

Dimensions of selected key parameters, measured directly from the schlieren images and numerically from the reconstruction, are illustrated for the baseline and bevelled nozzle in Table 4.2 and Table 4.3 respectively. The definition of these key parameters can be found in Figure 4.6(a) and Figure 4.8(a). All measured angles were obtained based on measured lengths and trigonometry, though the errors of angles were not provided as there is a natural bias of large errors for angles close to zero. Schlieren

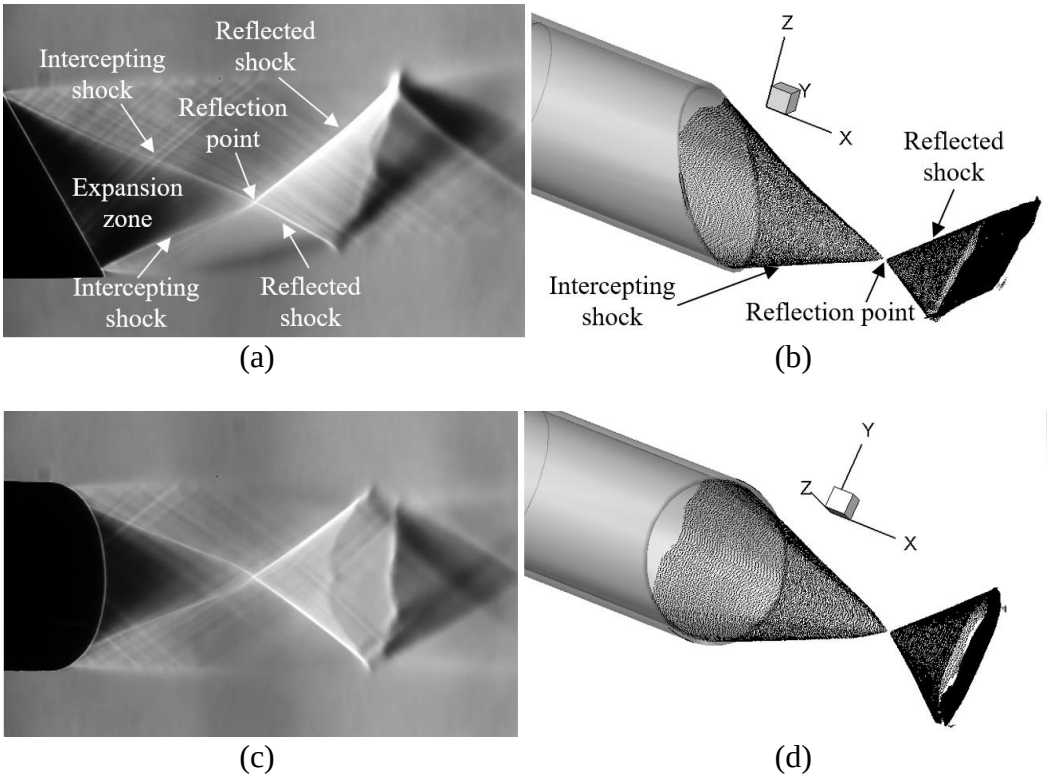

Figure 4.13: Bevelled nozzle's shock structures at NPR=5 (a) schlieren at 0° viewpoint (b) reconstructed shock (c) schlieren at 90° viewpoint (d) reconstructed shock

image key parameters' dimensions were obtained by multiplying the key parameters' pixel dimensions with the image-to-world magnification factor, whereby the magnification factor was obtained by using the nozzle outer diameter as reference length and is independent from the magnification factor obtained from camera calibration. In the schlieren images, shock wave edges have a width of a few pixels, and directly using the schlieren images to obtain the key parameters' pixel dimensions will increase the subjectivity and random errors of the measurements. To address this issue, post-processed schlieren images in the form of edge maps were used instead of the raw schlieren images in order to obtain the key parameters' pixel

dimensions. The associated random errors are placed at ±4 pixels and is always under 2% for the lengths of key parameters under consideration.

For the reconstruction results, key parameters were numerically extracted from the reconstructed VH. The accuracy of these results was limited by practical limitations of the pre-defined voxel and image resolution, accuracy of the focal length obtained from the initial laboratory camera calibration procedure (overall mean error of 0.63 pixels), accuracy of the 36 semi-synthetic camera matrices and accuracy of the edge maps that were generated. Of these limitations, the first two points are practical limitations that are inherent and unavoidable in experiments, hence only the final two points will receive additional attention in the following sub-sections.

Table 4.2: Reconstructed shock cone key parameters for baseline jet

	Schlieren images	Reconstructed shock cone	Percentage error
Baseline nozzle, under-expanded flow condition (NPR=4)			
D_{SC}	11.55 mm	11.34 mm	1.82
X_{RP}[8]	9.20 mm	9.10 mm	1.09
X_{CL}	17.58 mm	17.50 mm	0.46
θ_{IS}	33.6°	33.1°	-
θ_{RS}	36.3°	36.1°	-
Baseline nozzle, under-expanded flow condition (NPR=5)			
D_{SC}	12.01 mm	12.15 mm	1.17

[8] Due to the presence of a gap at the reflection point, the midpoint between the reflection points of the intercepting and reflected shocks was used to obtain X_{RP} for the reconstructed shock cone.

X_{RP}	14.60 mm	14.15 mm	3.08
X_{CL}	23.31 mm	23.57 mm	1.12
θ_{IS}	22.3°	22.3°	-
θ_{RS}	35.3°	35.1°	-

Table 4.3: Reconstructed shock cone key parameters for bevelled jet[9]

	Schlieren images	Reconstructed shock cone	Percentage error
Bevelled nozzle, under-expanded flow condition (NPR=4)			
X_{RP}[8]	9.08 mm	9.54 mm	5.07
$\theta_{IS\_90°}$	33.7°	36.5°	-
$\theta_{IS\_270°}$	31.6°	31.6°	-
$\theta_{RS\_90°}$	40.4°	40.7°	-
$\theta_{RS\_270°}$	32.2°	38.3°	-
Bevelled nozzle, under-expanded flow condition (NPR=5)			
X_{RP}	14.79 mm	15.73 mm	6.36
$\theta_{IS\_90°}$	22.6°	22.1°	-
$\theta_{IS\_270°}$	23.3°	23.8°	-
$\theta_{RS\_90°}$	42.8°	40.9°	-
$\theta_{RS\_270°}$	30.4°	30.4°	-

[9] Due to the asymmetry of the reconstructed shocks for the bevelled nozzle, only shock angles for the image plane shown in Figure 4.12(a) and Figure 4.13(a) are illustrated.

When comparing key parameters derived from the schlieren images and the reconstruction, the average error for the reconstructions' key parameters such as, shock cone diameter (D_{SC}), reflection point location (X_{RP}) and shock cell length (X_{CL}) is about 2.5%, with the maximum error not exceeding 6.4%. For the circular jet cases, the average error was about 1.5%. The low error margin coupled with the voxel sizes of the reconstructed shock cones provided earlier suggest that the errors in the reconstructed shock cones are in the range of a few voxels, indicating any further improvement would require the use of sub-voxel accurate schemes. The bevelled jets tend to have larger errors as compared to the baseline jets, with an average error of 5.7%. This can be explained by focusing on the differences in their image processing procedures where the dominant source of error is attributed to (explained in greater detail in sub-section 4.3.2.2). For the baseline jet, only one schlieren image was required due to the axisymmetric property of the jet. In contrast, the bevelled jet required 10 schlieren images captured at different viewpoints. A larger number of schlieren images used to generate the silhouette images will inevitably mean a higher chance for the bevelled jet's image processing procedure to introduce additional errors into the silhouette images. Going by the same line of thought, the errors associated with extending this technique to fully asymmetric problems may increase even further.

4.3.2.1 Semi-synthetic camera matrices

From Figure 4.10(b) and Figure 4.11(b), the reconstruction results can be observed to have axisymmetric geometrical properties about the jet axis, which is consistent with schlieren images of the shock structure taken from multiple view angles as mentioned earlier on. This was within expectations due to the use of the semi-

synthetic camera parameters, leading to 36 cameras possessing even angular spacing of 10˚ and equal orthogonal distance of the focal length *f* relative to the jet axis (see Figure 4.4(b)). The lack of ellipses or other irregular geometries in the results is a good indication that camera parameters are accurate enough to perform reconstruction at low enough errors such that it cannot be visually detected in the results.

Nevertheless, even though the reconstructed results of the baseline jets appear axisymmetric, there are still errors associated with some of the extracted parameters, as shown in Table 4.2. It will be useful to understand the origins of these errors, be it from the semi-synthetic camera parameters or the image processing procedures. A synthetic test was designed to narrow down the source of error by examining the performance of the semi-synthetic camera parameters. To conduct this test, a synthetic silhouette image was generated by creating a 1024px × 1024px matrix of zeroes with 2 × 2 cell of ones at the centre of the matrix, as shown in Figure 4.14(a). This image was then assigned to all 36 camera matrices and volume carving was conducted to obtain the visual hull. Theoretically, the real-world representation of the VH created from this image should be a cylinder with equal length and diameter. Since the criterion for a VH to be reconstructed is for sampled voxels to lie within all 36 projected visual cones, and the use of a very small silhouette generated with only 2 pixels in a single direction leads to very low aspect ratio visual cones being projected, the litmus test for the accuracy of the camera matrices will simply be to observe and see if anything can be reconstructed. In the event of a reconstruction failure, the 2 × 2 cell of ones will be increased to 4 × 4, 6 × 6 and so forth until

$$SYN = \begin{bmatrix} 0 & & \cdots & \cdots & & 0 \\ & \ddots & 0 & 0 & 0 & \\ \vdots & 0 & 1 & 1 & 0 & \vdots \\ \vdots & 0 & 1 & 1 & 0 & \vdots \\ & 0 & 0 & 0 & \ddots & \\ 0 & & \cdots & \cdots & & 0 \end{bmatrix}$$

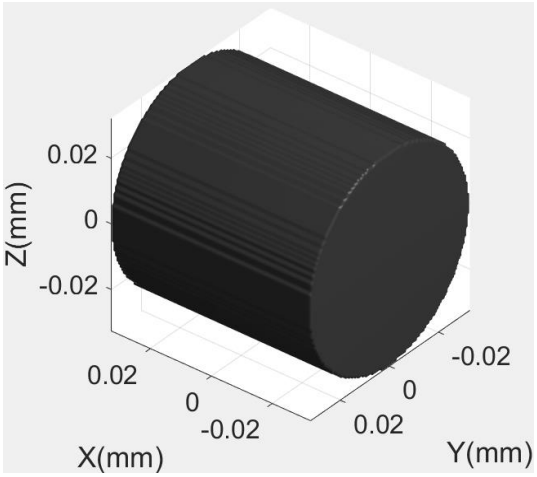

(a) (b)

Figure 4.14: Synthetic test (a) synthetic silhouette image with 2 × 2 cell of ones (b) reconstructed VH generated from synthetic silhouette image on the left

reconstruction of a VH is successful. The number of pixels of the silhouette can then be used as a quantitative indicator of the errors associated with the camera matrices.

The results for the reconstruction are shown in Figure 4.14(b), with over 800,000 remaining voxels out of a starting of 4 million voxels. The visually boxy (striations) reconstructed VH is an indicator of resolution limitations rather than inaccuracy of the camera matrices. The successful reconstruction along with the VH centred at the [0, 0, 0] location can be considered as a direct proof of the perfect alignment and accuracy of the camera matrices. To complete the study, the test was repeated with the introduction of errors into one of the camera matrix's external parameters. This created a misalignment for that one camera and should result in the intersection of the projected visual cones from only 35 cameras instead of all 36 cameras. Indeed, when the volume carving was conducted, no VH was reconstructed and the reconstruction fails during the projection of the visual cone from the misaligned camera. Finally, the test was repeated once again, but with errors introduced into one

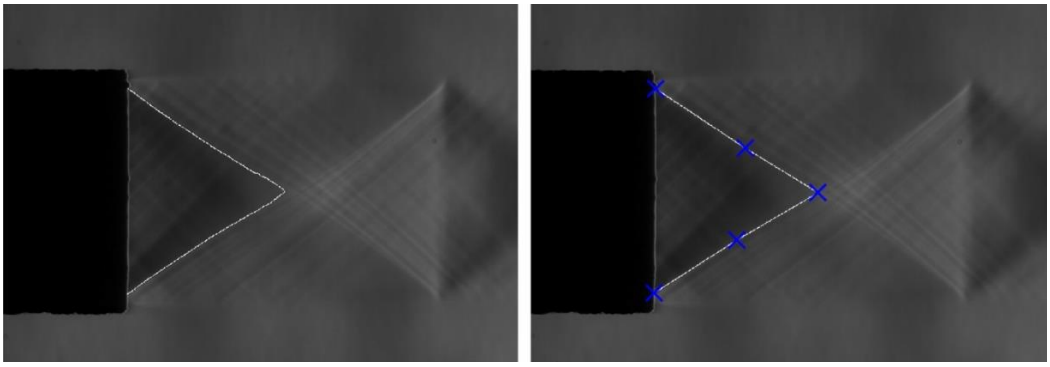

(a) (b)

Figure 4.15: Edge map obtained from (a) edge detection method (b) manual spline fitting method

of the camera matrix's principal point. Again, no VH was reconstructed and the reconstruction fails at the camera with the wrong parameters. With these test results, there is sufficient evidence to conclude that the semi-synthetic camera matrices are performing as designed, and errors of the reconstructed shock structures originated solely from the image processing procedure.

4.3.2.2 Image processing procedures

The image processing procedures are assessed next. Since the edge detection and manual spline fitting method was used interchangeably, a comparison will be provided here. The edge maps of the baseline NPR=4 jet obtained from the edge detection method is shown in Figure 4.15(a), and with the manual spline fitting method as shown in Figure 4.15(b). The blue crosses in Figure 4.15(b) mark the locations that were manually selected on the image, and it must be highlighted that they were not part of the edge map. The edge maps generated from both methods were then further processed to obtain their corresponding silhouette image, before proceeding to volume carving.

The VH results for both methods are shown in Figure 4.16, with no observable difference between them. This suggests that the two methods are equally accurate for visualization purposes. The geometrical properties of both reconstructed shocks were extracted and presented in Table 4.4. It can be observed that there are differences in results between the two methods, though it is not immediately obvious which method performs better. The diameter of the shock cone obtained from edge detection method appears to be closer to the dimensions obtained directly from the schlieren images, while the manual spline fitting method offers lower errors for the reflection point location. The discrepancy of the parameters is a clear indicator that that the image processing procedure is a source of errors for the reconstructed VH.

The edge detection method is a precise method that offers edge maps to be generated in a consistent and efficient manner under ideal conditions, or when the input images have a high SNR. If the input images have a low SNR, the edge detection method will not be robust and can no longer be considered efficient as images from multiple views cannot be processed with the same set of parameters anymore. Finding the set of optimal parameters which includes the edge threshold, standard deviation for the Gaussian filter and area opening threshold all requires experience and judgement that cannot be replaced by algorithms easily. A possible future direction to automate the process can be to integrate machine learning concepts and train these parameters with huge datasets but that is beyond the scope of the current study. Hence, for images that have low SNR, generation of the edge map using the edge detection method becomes a time-consuming and inefficient process.

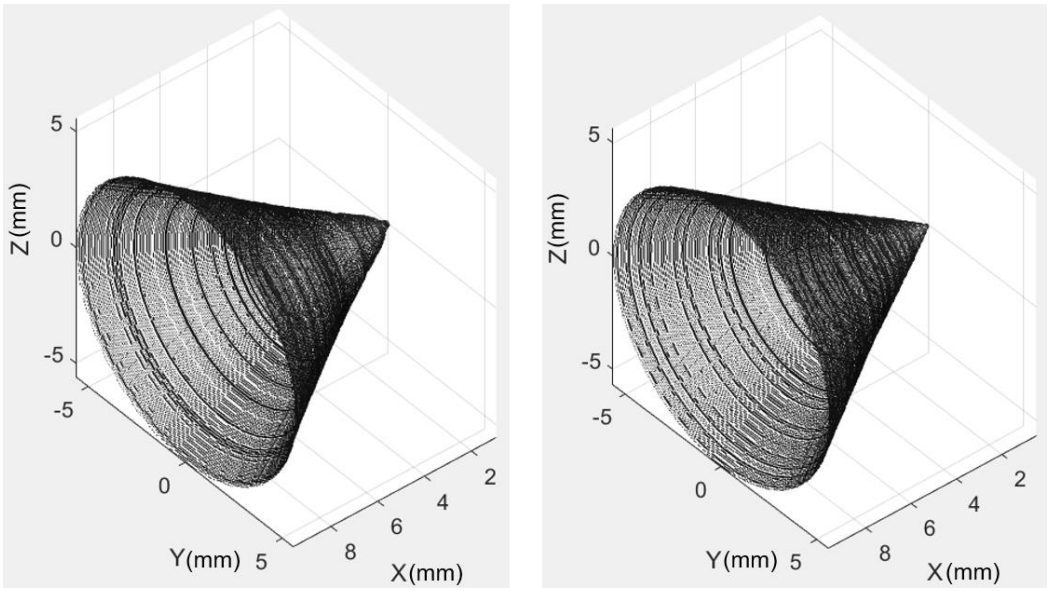

(a) (b)

Figure 4.16: Reconstruction results obtained from (a) edge detection method (b) manual spline fitting method

Table 4.4: Comparison of geometrical properties for baseline nozzle at NPR=4

	Schlieren images	Reconstructed shock cone	Percentage error
Edge detection method			
D_{SC}	11.55 mm	11.34 mm	1.82%
X_{RP}	9.20 mm	8.70 mm	5.43%
θ_{IS}	33.6°	33.1°	-
Manual spline fitting method			
D_{SC}	11.55 mm	11.25 mm	2.60%
X_{RP}	9.20 mm	9.23 mm	0.33%
θ_{IS}	33.6°	31.1°	-

In contrast, while the manual spline fitting method appears to be cumbersome and not as systematic, they do hold certain advantages over the edge detection method. For input images that are not ideal for edge detection algorithms, the manual spline fitting method is more robust and allows the user to incorporate posteriori knowledge directly in the post-processing of the schlieren image. This is advantageous as the human perception is still widely conceived as the most efficient and powerful image processor [113, 114] even after decades of computer vision research. The manual spline fitting method will also be robust for a vastly different study, such as in supersonic impinging jet applications, while the same cannot be said for the edge detection method which was specially developed for the current application. Furthermore, little time is required to pick out selected points lying along a shock wave in an image. While manual spline fitting method leads to a certain degree of subjectivity associated with the selection of the points to fit the splines, this can be minimized with careful selection of the shock wave points, and the random error associated with this subjectivity is estimated to be at ±4 pixels within the present study.

4.4 Summary

A novel approach for 3D shock wave reconstruction was proposed, based on schlieren images and a shape-from-silhouette image-processing technique known as voxel-based visual hull. Due to the very small dimensions of the shock structures with relatively large projection distances, precise camera parameters were found to be crucial in obtaining accurate reconstructed shocks. This provided the motivation behind the present approach of integrating a conventional camera calibration process

with synthetically generated camera parameters to obtain semi-synthetic camera matrices. By making use of the experimentally calibrated focal length during the synthetic camera parameters generation process, useful geometrical information can be numerically extracted from the reconstructed shock structures.

Shock structures for baseline and bevelled jets were reconstructed under the assumptions of no geometrical concavities and steady shock systems, with extracted key parameters of the reconstructed baseline and bevelled jet having an average error of 2.5%. Extending the technique to more complicated flow scenario such as the bevelled jet brings about an additional challenge due to the schlieren line-of-sight blockage from the nozzle. This was overcome with a heuristic linear extrapolation of the shock wave edge maps during the silhouette image generation process. The accuracy of the technique is strongly dependent on the quality of the schlieren images, with high shock wave contrast and clearly defined edges offering the best reconstruction results. The presence of multiple weak shocks decreases the SNR of the acquired images while strong shocks have the most potential in generating schlieren images of shock waves with high image contrast when the schlieren system is appropriately over-ranged.

The performance of the semi-synthetic camera parameters and the image processing procedures were evaluated, and error sources were identified to be solely originating from the image processing procedures. By directly reconstructing the shock waves without the need to measure the global velocity or density field, this provides the advantage of low hardware requirements, low computational time, and high-resolution reconstructed shock waves. The proposed technique is particularly well

suited for steady compressible flow scenarios with optical access to conduct schlieren experiments, with the presence of strong shocks to obtain optimal schlieren images for best reconstruction results. The success of the present unique approach highlights the potential of its application towards more complex 3D shock reconstructions in future studies, particularly in strong shocks application whereby existing 3D experimental techniques are not particularly well suited for. Examples of potential application includes optimization of multi-shock designs at supersonic inlet, study of shock geometries in hypersonic flows and formation of shock systems in supersonic impinging jets.

Chapter 5 On the Effects of Bevelled Nozzles on Standoff Shocks in Supersonic Impinging Jets

5.1 Overview

Impinging jets are directly relevant in applications such as spacecraft launches, gas turbine cooling, cold-spray technologies, aeroacoustics, thrust vectoring systems, among many others [115-119]. Depending on the velocities of the jets used, the resulting impinging flow phenomena can be very different, particularly between subsonic and supersonic jets [120, 121]. Supersonic impinging jets are typically characterized by extremely high flow shear, high levels of aeroacoustics noise, distinct shock structures within the supersonic jet bodies and the formation of standoff shocks. It is now known that the flow field produced by a supersonic impinging jet can be categorized into three main flow regions - (1) the primary jet flow, (2) the impingement zone, and (3) the radial wall jet [120]. The highly complex impingement zone has been the subject of many studies due to their strong influences upon the most important flow characteristics of the supersonic impinging jet [16, 122, 123]. It is also in this region where standoff shocks are formed.

In the classical work of Donaldson and Snedeker [120] and Donaldson et al. [121], flow structures and heat transfer properties of a jet impinging under various configurations were investigated using selected experimental techniques such as schlieren photography. Subsequent studies by Kalghatgi and Hunt [123] focused on the impingement zone at small nozzle-to-plate separation distances, where schlieren photography and pressure measurement results indicate a close relationship between

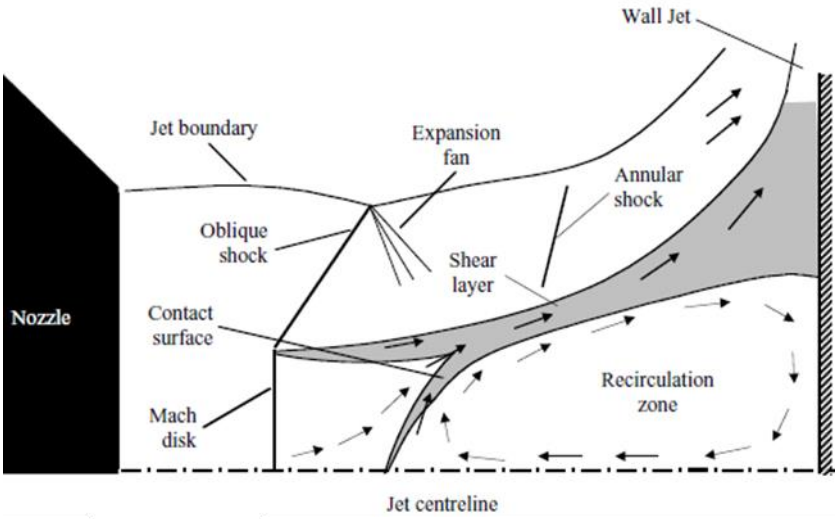

Figure 5.1: Flow schematic of a supersonic impinging jet [122]

the formation of a stagnation bubble and the standoff shocks and jet shock waves. The stagnation bubble, a region of slow recirculating flow under the standoff shock, was observed to exert strong influences upon the impingement surface pressure and heat transfer characteristics. Further impingement studies were also conducted based on normal [124] and inclined flat plates [16] at small separation distances. Through schlieren visualizations and other quantitative results, these studies reaffirmed the complexity of the interactions between the supersonic jet and standoff shocks, as well as their importance in determining the occurrence of the stagnation bubble. The study by Lamont and Hunt [16] further revealed that the complex shock interactions are able to result in much greater maximum impingement pressures on the inclined flat plates as compared to the normal flat plates.

In addition, Krothapalli et al. [125] revealed that the jet shock structures confer strong influences upon pertinent flow features at small separation distances, based on

nonlinear lift loss with NPR variation. Furthermore, it was also speculated that the precise geometries of the standoff shock and stagnation bubble both play important roles in the resulting impinging behaviour. The crucial roles played by the supersonic jet shocks and standoff shocks have also been ascertained in the study of impinging jet aeroacoustics [19, 126]. Through the use of conventional and phase-locked schlieren photography alongside acoustics and plate pressure measurements, large plate impulsive tones were detected when the standoff shock was observed to collapse during its oscillation cycle [127]. Furthermore, the occurrence of a Mach disk upstream of the standoff shock was found to contribute towards the tonal production, while tonal mitigation occurs when the first or second jet shock takes on a conical shape. Subsequently, the strength of the standoff shock and the upstream velocity gradients were found to significantly influence jet stability conditions [122], while zones of silence were observed when the standoff shocks were located close to the impingement plate.

Since the primary jet shocks and standoff shocks have been established to have strong influences on the key properties (aeroacoustics, plate pressure and heat transfer) of an impinging jet, appropriate control of the shock structures can lead to desirable impingement properties in engineering applications. This can be achieved through the use of non-conventional IO nozzles [39], which has been shown in Chapter 4 to be particularly effective in introducing 3D distortions to the jet shock structures. Nonetheless, despite the possibility of manipulating the flow and shock characteristics associated with the impingement behaviour favourably through the use of non-conventional nozzles, there appears to be very limited research and

discussions focusing on the use of such nozzles in supersonic impinging jet conditions.

The current study [128] aims to feature this knowledge in the field of asymmetric supersonic jet flow impingement by experimentally studying the flow characteristics of moderately under-expanded supersonic impinging IO jets at small nozzle-to-plate separation distances. In addition, while traditional schlieren visualizations of shock structures are commonly used in supersonic impinging jet studies, 3D schlieren techniques could prove to be more appropriate and insightful in cases where the resulting shocks are expected to be non-axisymmetric and highly three-dimensional. A new 3D shock reconstruction approach based on the visual hull image processing technique was proposed and demonstrated in an asymmetric free jet application [42] in Chapter 4. As such, it will be useful to utilize this technique to shed more light upon the differences between standoff shocks produced by different supersonic impinging IO jets. The current study presents a unique opportunity in extending the scope of application of this novel technique. To the best of the author's knowledge, it is the first time this technique is used for the study of highly complex supersonic impinging jet flows.

5.2 Experimental setup and reconstruction procedures

5.2.1 Experimental setup

The experiments were performed using the supersonic jet apparatus presented in Section 3.1. For the impingement surface, an aluminium, 6 mm thick, 30D × 30D square plate was mounted on a rigid fixture anchored against the laboratory wall. It

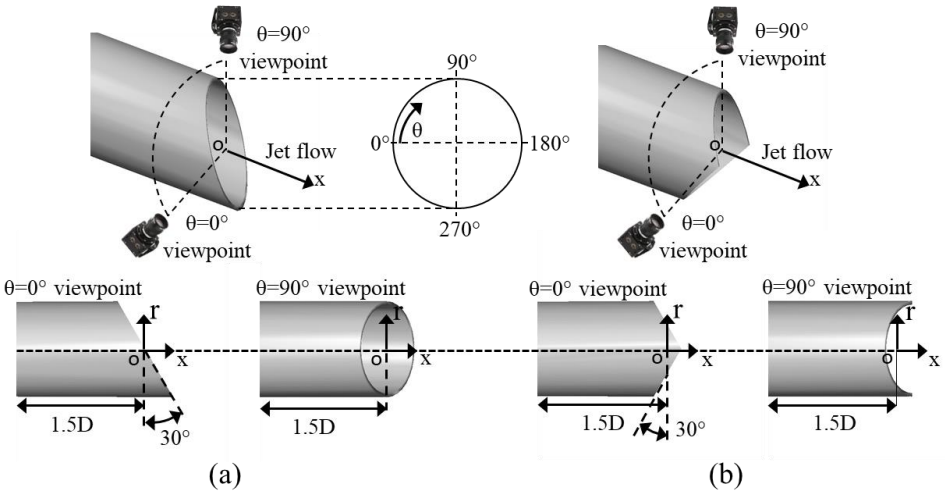

Figure 5.2: Schematics of the camera viewpoints and coordinate system for the (a) 30° bevelled and (b) 30° double-bevelled nozzles

was positioned such that the jets impinged upon it perpendicularly and in the centre at two different separation distances (h) of h/D=1 and 1.5. The use of relatively small separation distances limits the influence of mixing effects, which can generally be ignored at small separation distances since the effects of shock structures interactions are much more dominant [16].

The circular baseline, 30° bevelled and 30° double-bevelled nozzles were investigated in this study, and their design details had been presented in Section 3.2. Throughout the present study, the jet was operated at two different moderately under-expanded conditions of NPR=4 and 5. By investigating the two IO nozzles with similar bevel angles, influences upon the flow imposed by different number of bevels can be explored here. The camera viewpoints and cylindrical coordinate system (r, θ, x) adopted in the current study are defined in the schematic as shown in Figure 5.2.

Schlieren experiments were performed using the setup presented in Section 3.2. The knife-edge was placed in the vertical configuration normal to the jet flow and adjusted to about 80% cut-off to over-range the schlieren system and better highlight the shock structures. An IDT NX4-S1 camera with a Nikon AF Micro-Nikkor 200 mm f/4D IF-ED lens was used to capture the schlieren images. To compensate for the image brightness levels and reduce turbulence effects, a relatively long frame exposure time of 200 μs was used for the impinging jets and over 400 μs was used for the free jets, unless otherwise stated. All images were captured at 1000 FPS.

5.2.2 3D shock reconstruction procedures

As the 3D shock reconstruction principle and procedures have been described in great detail in Chapter 4 [42], this section will only highlight the most important features of the reconstruction procedures adopted in the present study. To perform the reconstruction on the standoff shocks, two pieces of information are required – Firstly, the silhouette images of the standoff shock and secondly, the corresponding camera matrices which defines the position and orientation of the cameras capturing the images. Ideally, an infinite number of silhouette images with its corresponding camera matrices (i.e. images of the standoff shock and the corresponding camera information at infinite number of different viewing angles) is required. Clearly, this is not possible in practice. Instead, the bevelled nozzles were rotated at 10° intervals such that schlieren images were captured at 10 different viewing angles for the range of $\theta=[0°, 90°]$. Image post-processing was subsequently performed to convert these images into silhouette images necessary for the shock reconstructions.

In accordance to the procedures described in Chapter 4 [42], the image post-processing mainly consists of binary decisions performed at the location of the standoff shocks, which classifies the image pixels as part of the standoff shock silhouettes or not. For the current study, since the standoff shocks display excellent image intensity contrast with the background, the acceptance criterion is based on a pre-defined image intensity threshold. The camera matrices were obtained through a combination of standard external camera calibration procedure and synthetically generated camera parameters, which followed the processes described in Chapter 4 [42]. Through the preceding steps, the two important pieces of information necessary for the shock reconstruction were obtained. With this information, volume carving operation was performed on a pre-defined tessellation of cubic voxels, and the reconstructed 3D shock structures were extracted for subsequent analysis.

5.3 Results and discussions

5.3.1 Free-jet configurations

Comparisons between impinging jets and their corresponding free-jet counterparts are often performed in earlier studies [120, 122] as a starting point of discussion. Similarly, shock patterns associated with M_d=1.45 freely-exhausting supersonic jets from the baseline and two IO nozzles at NPR=5 and 4 are presented in Figure 5.3 and Figure 5.4 respectively. Since detailed discussions of these freely-exhausting supersonic jets have been covered in earlier studies [27, 41], only the most important features relevant to the present study will be highlighted here. It should be noted that structurally speaking, both NPRs produce qualitatively similar shock structures under free-jet configurations. Discrepancies of interest exist only in terms of quantitative

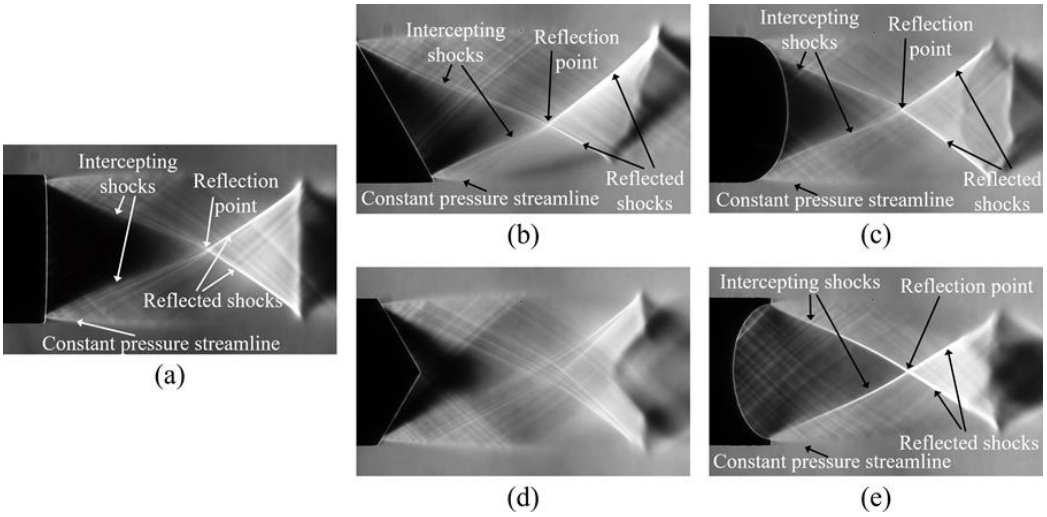

Figure 5.3: Schlieren images of M_d=1.45 freely-exhausting jets at NPR=5 for (a) baseline, (b) 30° bevelled (θ=0°), (c) 30° bevelled (θ=90°), (d) 30° double-bevelled (θ=0°) and (e) 30° double-bevelled (θ=90°) nozzles

characteristics such as shock cell lengths and locations of the reflection point, which will be discussed later.

With reference to both figures, high-speed schlieren imaging results show that all test nozzles produce quasi-steady shock systems. In Figure 5.3(a), intercepting oblique shocks emanating from the baseline nozzle lip can be seen to reflect off each other at the reflection point to form two reflected shocks that end at the terminating line of the first shock cell. No Mach disk is present at the reflection point due to the conservative under-expansion exhaust conditions used here. For the 30° bevelled nozzle, image captured with respect to the θ=0° viewpoint of the jet is shown in Figure 5.3(b) while that of the θ=90° viewpoint is shown in Figure 5.3(c). As compared to the baseline test case shown in Figure 5.3(a), the first shock cell has undergone significant changes, with what appears to be a slight upward vectoring of the jet body and shocks in the direction of the shorter nozzle lips. The reflection

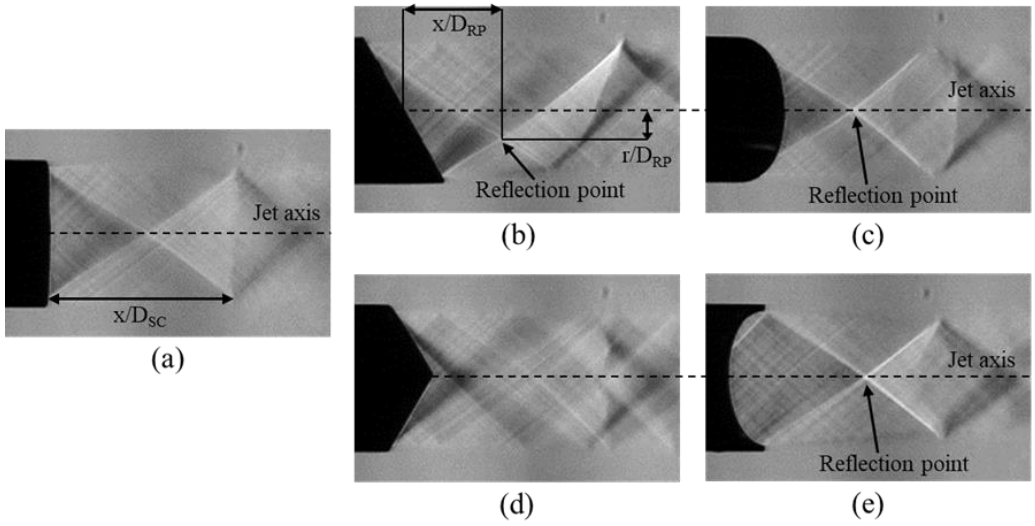

Figure 5.4: Schlieren images of M_d=1.45 freely-exhausting jets at NPR=4 for (a) baseline, (b) 30° bevelled (θ=0°), (c) 30° bevelled (θ=90°), (d) 30° double-bevelled (θ=0°) and (e) 30° double-bevelled (θ=90°) nozzles. Note that the brightness of these images has been enhanced.

point has also shifted away from the jet axis and towards the longer nozzle lips region. This could be due to the intercepting shocks originating from different axial positions but with similar intercepting shock angles – which is not too surprising since it is still a circular nozzle. Indeed, it can be observed that when the intercepting shock starts to form at the longer nozzle lip, the intercepting shock from the shorter nozzle lip has already almost reached the jet centreline. A 3D representation and geometrical information of this shock system can be found in Lim et al. [42]. For the 30° double-bevelled nozzle, the reflection point appears clearly in Figure 5.3(e) but less so in Figure 5.3(d), due to the existence of numerous weak shocks in the latter. In this case where the 30° double-bevelled nozzle was designed such that it is symmetrical about the jet axis along both θ=0° and 90° viewpoints, the reflection point maintains its location along the jet axis, with no vectoring of the shock systems observed.

Table 5.1: Non-dimensional parameters of M_d=1.45 freely-exhausting supersonic jets

Nozzle type	Shock cell length (x/D_{SC})	Reflection point axial location (x/D_{RP})	Reflection point radial location (r/D_{RP})	Quasi-steady
NPR=5				
Baseline	1.86	1.19	0	Yes
30° bevelled	1.79	1.14	0.11 (θ=270°, towards longer lips)	Yes
30° double-bevelled	1.83	1.17	0	Yes
NPR=4				
Baseline	1.34	0.71	0	Yes
30° bevelled	1.35	0.76	0.21 (θ=270°, towards longer lips)	Yes
30° double-bevelled	1.28	0.91	0	Yes

Table 5.1 summarizes the shock cell lengths and reflection point locations with respect to the jet origin, as well as the shock stability conditions determined from the high-speed schlieren images and will be relevant to the discussions later. All values were normalized by the jet inner diameter (D) and averaged across θ=0° and 90° image viewpoints for the 30° bevelled and 30° double-bevelled test nozzles, except for the reflection point of the 30° double-bevelled nozzle whereby only the θ=90° viewpoint (see Figure 5.3(e) and Figure 5.4(e)) information was considered. Shock systems are deemed to be quasi-steady since there is no image blurring in the schlieren images, and there is less than 0.05D change in the position of the shock

systems across the time-series images captured at 1000 FPS (shown in Appendix A1). This observation is also consistent with the results in past studies [27, 41]. The error of the parameters in Table 5.1 is estimated to be ±0.05D.

5.3.2 Impinging jet – Effects of NPR

5.3.2.1 Configuration 1: h/D=1 and NPR=5

Schlieren images of under-expanded jets at NPR=5 impinging upon the impingement surface at a separation distance of h/D=1 are presented in Figure 5.5. Based on Table 5.1, it can be discerned that the separation distance is shorter than the first shock cell length, with the *impingement surface upstream of the reflection point location*. For the baseline nozzle shown in Figure 5.5(a), the standoff shock resembles that of a convex disk with a Mach disk on the top surface. Note that similar standoff shocks had been observed earlier in past studies [129, 130] despite some differences in the test conditions. This unique disk geometry has been observed to manifest when standoff shocks are located within the initial expansion region near the nozzle lips [16], which is certainly the case for the present test configuration. The apparent finite "thickness" of the standoff shock can be attributed to its inherent 3D geometry and the integrative nature of schlieren photography. Additionally, it should also be mentioned that the region of intense pixel intensity adjacent to the impingement surface represents the radial wall jet region, where a series of compression and expansion waves extend away from the impingement point. However, the most important aspect of the baseline nozzle standoff shock is that its features and outlines are invariant even if the nozzle were to be rotated to another angle during the high-speed schlieren imaging.

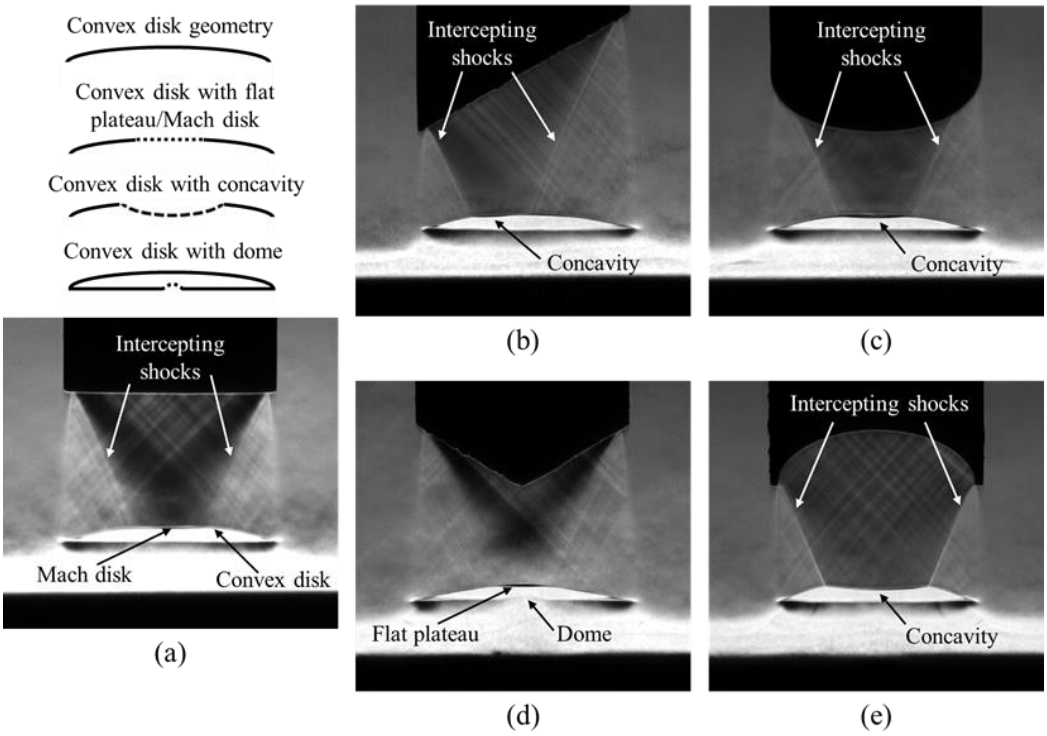

Figure 5.5: Schlieren images of M_d=1.45 impinging jets at h/D=1 and NPR=5 (i.e. configuration 1) for (a) baseline, (b) 30° bevelled (θ=0°), (c) 30° bevelled (θ=90°), (d) 30° double-bevelled (θ=0°) and (e) 30° double-bevelled (θ=90°) nozzles

For the 30° bevelled nozzle shown in Figure 5.5(b) and Figure 5.5(c), the overall geometry and position of the standoff shock remains very similar to the baseline test case; a convex disk. Possibly, the standoff shock is located too far upstream within the initial expansion region near the nozzle lips and is hence comparatively invariant to the influence of the nozzle exit geometry. Nonetheless, some minute changes in the form of a concavity (slight depression) along the top surface of the standoff shock can still be observed due to the asymmetric nozzle design. Along θ=0° viewpoint, the asymmetric intercepting oblique shocks produced a small concavity that is tilted slightly towards the longer nozzle lip region (i.e. towards the left of the jet axis in Figure 5.5(b)). In contrast, they remain symmetric along the θ=90° viewpoint.

Clearly, the original standoff shock geometry from the baseline nozzle has been modified in an asymmetric fashion by the use of the bevelled nozzle.

As for the 30° double-bevelled nozzle, even though the overall geometry takes on the shape of a convex disk, the outlines of the top surface of the standoff shock differ greatly between θ=0° and 90° viewpoints. There appears to be no clear pair of intercepting shocks in the θ=0° viewpoint, in contrast to the symmetrical intercepting shocks observed to clearly intersect the standoff shock in the θ=90° viewpoint. The result is the formation of a small flat plateau and a significantly large concavity on top of the standoff shock along θ=0° and 90° viewpoints respectively, as shown in Figure 5.5(d) and Figure 5.5(e). Like the previous test cases, the concavity is always bounded by the intercepting oblique shocks. While it is convenient to regard the geometry on the top surface here as a Mach disk, it will be erroneous to do so since the concavity in the θ=90° viewpoint is depressed downward instead of taking on a flat plateau geometry like the θ=0° viewpoint. In addition, a small dome can be observed at the base of the standoff shock in Figure 5.5(d). Since the standoff shock thickness represents the three-dimensionality of the shock, the dome is likely to exist at the peripheral of the base of the standoff shock. The standoff shock geometries across the two viewpoints are very different, indicating that the 30° double-bevelled nozzle is effective in introducing asymmetry to the geometry of the standoff shock.

Based on the high-speed schlieren imaging experiments, the standoff shocks produced by all three nozzles were observed to be quasi-steady, where qualitatively the positions of the standoff shocks remain relatively invariant between the different

Table 5.2: Non-dimensional dimensions and characteristics of standoff shocks at h/D=1 and NPR=5 (configuration 1)

Nozzle type	Standoff shock distance (s/D)	Standoff shock thickness (t/D)	Standoff shock geometry
Baseline	0.33	0.08	Axisymmetric convex disk with Mach disk in the centre.
30° bevelled	0.31	0.08	Convex disk with concavity shifted and tilted towards longer nozzle lip.
30° double-bevelled	0.35	0.08	Disk with "saddle point" geometry along top surface. Two small domes in the same plane as the nozzle longer lips.

nozzle designs. The standoff shock thicknesses, indication of its overall three-dimensionality, do not differ too drastically among the three different nozzles. A summary of the state and geometrical information of the standoff shocks is provided in Table 5.2, whereby the standoff shock distance (s) is defined to be the distance between the impingement surface and top-most point on the standoff shock, and the standoff shock thickness (t) is defined as the distance between the top-most and bottom-most points of the standoff shock. The estimated uncertainty of these parameters is below 2% of the jet diameter.

5.3.2.2 Configuration 2: h/D=1 and NPR=4

To look into the effects of NPR upon the structure of the standoff shocks, NPR=4 was used while maintaining the same separation distance of h/D=1 and the corresponding schlieren images are shown in Figure 5.6. The primary difference between the flow scenarios at NPR=5 and 4 (i.e. configurations 1 and 2 respectively)

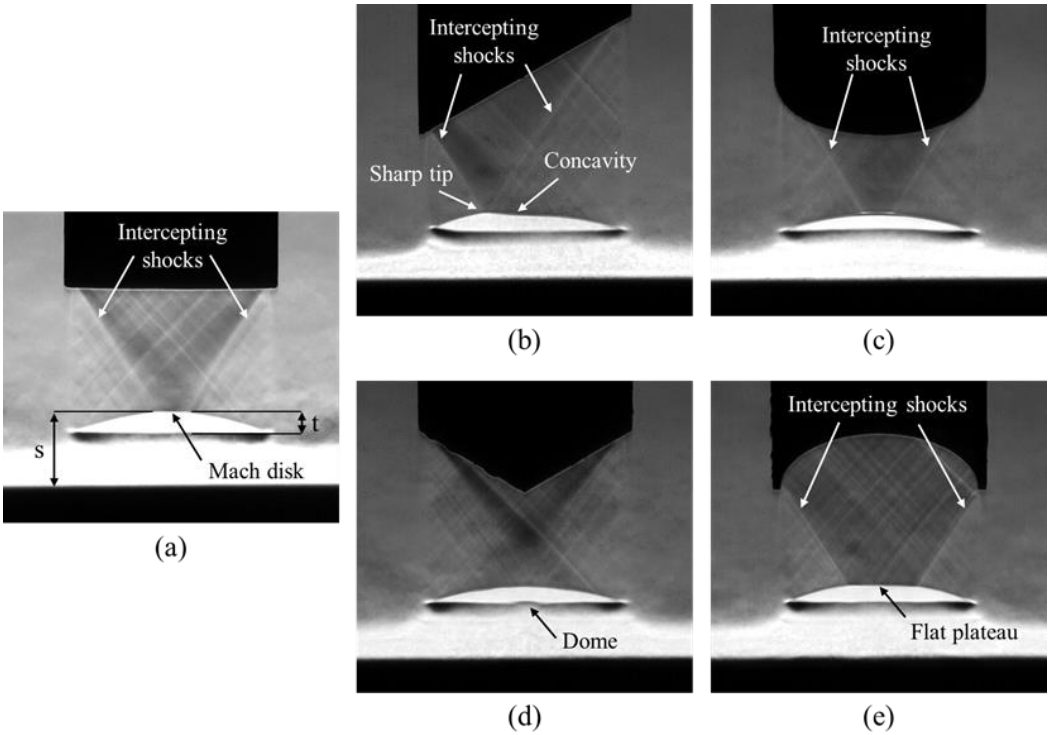

Figure 5.6: Schlieren images of M_d=1.45 impinging jets at h/D=1 and NPR=4 (i.e. configuration 2) for (a) baseline, (b) 30° bevelled (θ=0°), (c) 30° bevelled (θ=90°), (d) 30° double-bevelled (θ=0°) and (e) 30° double-bevelled (θ=90°) nozzles

is that the *impingement surface is now situated downstream of the reflection point location* but still within the first jet shock cell in all three test cases. Since the under-expansion is more conservative, the adverse pressure gradient across the reflection point is also expected to be weaker. For the baseline nozzle as shown in Figure 5.6(a), the standoff shock has a small flat plateau (i.e. Mach disk) along its top surface. The diameter of the Mach disk is also significantly smaller as compared to the one shown in Figure 5.5(a) and could possibly be due to the intercepting oblique shocks meeting the standoff shock much closer to the jet axis at NPR=4. The overall standoff shock thickness is also visibly greater than its NPR=5 counterpart in configuration 1, signifying a greater extent of three-dimensionality present in the overall geometry.

For the 30° bevelled nozzle, the standoff shock along θ=0° viewpoint as depicted in Figure 5.6(b) has a sharp tip pointing towards the longer nozzle lip, which coincides with the position of the reflection point formed by the intercepting oblique shocks. The concavity interestingly remains approximately at the centre but tilted towards the shorter nozzle lip. Hence, the tilt of the concavity is opposite to that observed at NPR=5 condition. Along θ=90° viewpoint shown in Figure 5.6(c), the standoff shock resembles that of the baseline nozzle in Figure 5.6(a), except that it is thinner. Comparing with its NPR=5 counterpart in configuration 1 (see Figure 5.5(c)), the concavity does not appear to exist anymore. Finally, for the 30° double-bevelled nozzle presented in Figure 5.6(d) and Figure 5.6(e), the standoff shocks are symmetrical about the jet axis. Along θ=0° viewpoint, the standoff shock takes on the geometry of a convex disk and the top surface does not appear to form any concavity or flat plateau. This is likely because there are numerous weak shocks emanating from the nozzle instead of a pair of strong intercepting oblique shocks forming the reflection point. On the other hand, a flat plateau bounded by the intercepting oblique shocks exists on the top surface of the standoff shock along the θ=90° viewpoint. As compared to its NPR=5 counterpart in configuration 1 (see Figure 5.5(e)), the decrease in concavity/plateau diameter is likely caused by the intercepting oblique shocks meeting the standoff shock closer to the jet axis. Similar to the NPR=5 counterpart, a small dome can once again be observed at the base of the standoff shock, as shown in Figure 5.6(d). A summary of the standoff shock characteristics for h/D=1 and NPR=4 (configuration 2) is presented in Table 5.3.

Table 5.3: Non-dimensional dimensions and characteristics of standoff shocks at h/D=1 and NPR=4 (configuration 2)

Nozzle type	Standoff shock distance (s/D)	Standoff shock thickness (t/D)	Standoff shock geometry
Baseline	0.38	0.12	Axisymmetric convex disk with Mach disk in the centre.
30° bevelled	0.33	0.09	Convex disk with an "edge" feature tilted towards longer nozzle lip, coinciding with intercepting shocks. Concavity shifted towards jet axis and tilted towards shorter nozzle lip.
30° double-bevelled	0.36	0.09	Disk resembling a "2D bow shock" along top surface. Two small domes in the same plane as the nozzle longer lips.

Throughout both test configurations, the IO jets have demonstrated their capabilities in influencing the standoff shock geometry. In view of the high degree of asymmetry in the standoff shocks, 3D shock wave reconstruction was applied to all the preceding test cases to shed more light on the standoff shocks' geometry. Nonetheless, as the geometrical difference was small to begin with, the results also reflected as such and it was not meaningful to present the reconstruction results directly. In order to allow the reader to better discern the key shock structure differences, the results were carefully analysed and schematics of the standoff shock with exaggerated key features are presented in Figure 5.7 and Figure 5.8.

Based on the results, it becomes very clear how the standoff shock has changed its 3D geometry as the NPR was reduced across the two test configurations. For the baseline test case, while the features remain axisymmetric, the Mach disk has reduced

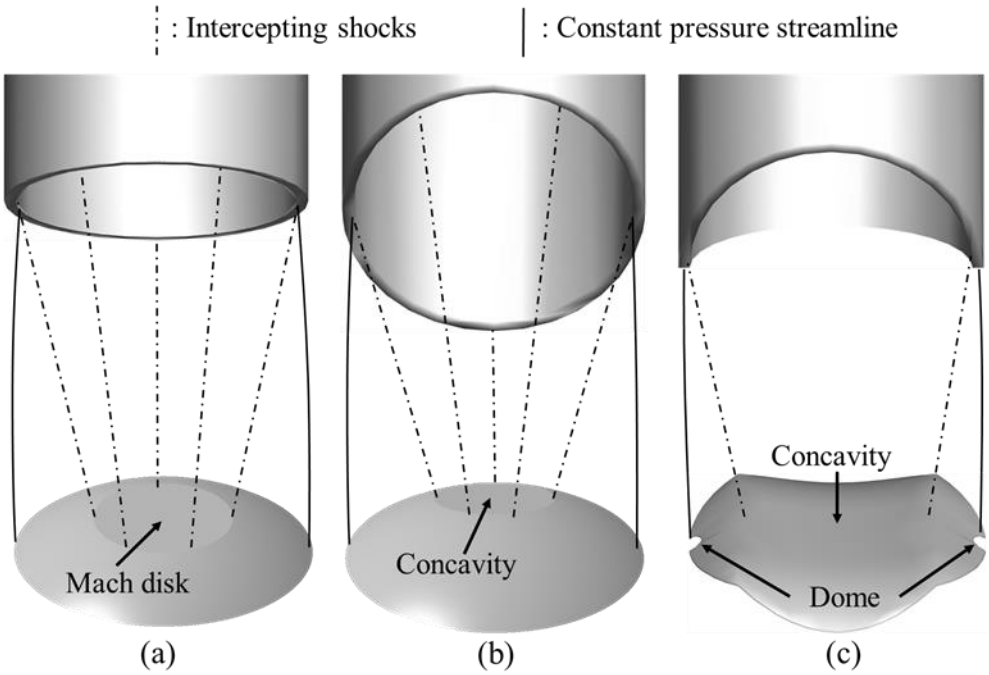

Figure 5.7: Schematics of standoff shock at the impingement condition of h/D=1 and NPR=5 (i.e. configuration 1) for (a) baseline, (b) 30° bevelled and (c) 30° double-bevelled nozzles. *Note that the key features are not drawn to scale*.

its diameter from what is shown in Figure 5.7(a) to that of Figure 5.8(a). For the 30° bevelled test case, the concavity in Figure 5.7(b) was initially pointing towards the longer lips of the nozzle but shifted towards the jet axis and pointed towards the shorter nozzle lips with the decrease in NPR as shown in Figure 5.8(b). The sharp tip that was observed in Figure 5.6(b) is now highlighted in Figure 5.8(b) and appears to belong to an "edge" that coincides with the intercepting shocks. Note that this edge feature also manifested itself in Figure 5.6(c), at the tip of the standoff shock bounded by the intercepting shocks. For the 30° double-bevelled test case, the standoff shock in configuration 1 resembles that of a "saddle point" geometry as shown in Figure 5.7(c). The small dome at the base of the standoff shock observed in Figure 5.5(d) appears to be in the same plane as the nozzle longer lips as indicated

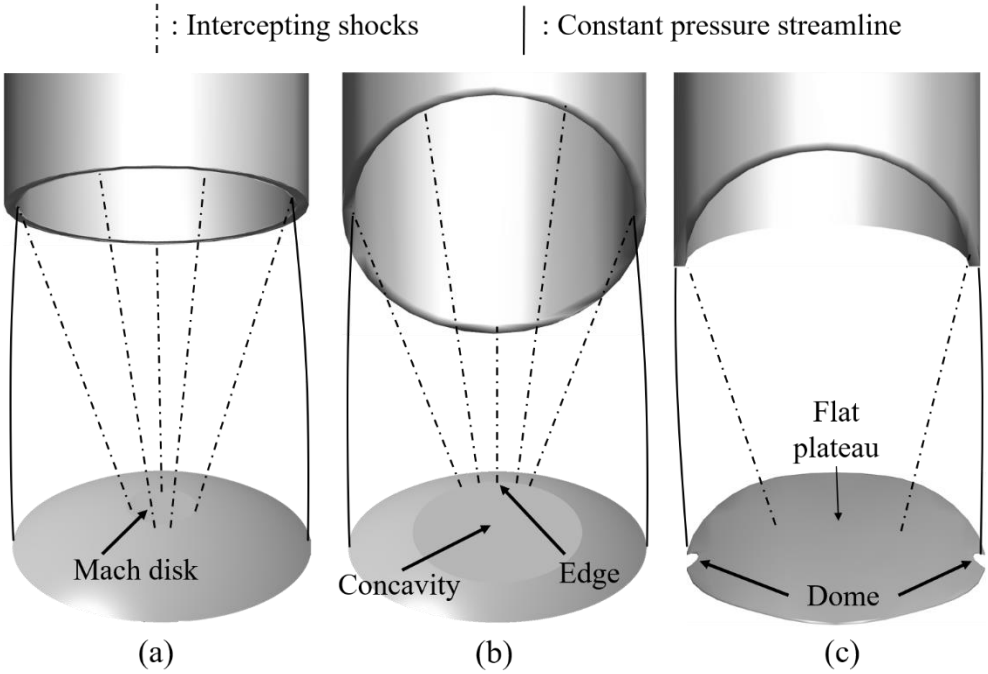

Figure 5.8: Schematics of standoff shock at the impingement condition of h/D=1 and NPR=4 (i.e. configuration 2) for (a) baseline, (b) 30° bevelled and (c) 30° double-bevelled nozzles. *Note that the key features are not drawn to scale*.

in Figure 5.7(c). For the same test case in configuration 2, the standoff shock appears to look more like a 2D bow shock instead, due to the combination of the convex disk and flat plateau in the θ=0° and 90° viewpoints respectively.

5.3.3 Impinging jet – Effects of separation distance

5.3.3.1 Configuration 3: h/D=1.5 and NPR=5

To look into the effects of separation distance, the nozzle-to-plate distance was increased to h/D=1.5 while maintaining NPR=5. This allows direct comparisons with the h/D=1 and NPR=5 configuration (configuration 1) presented earlier. This configuration also ensures that the *impingement surface is situated downstream of the reflection point location* but still within the first jet shock cell in all three test cases.

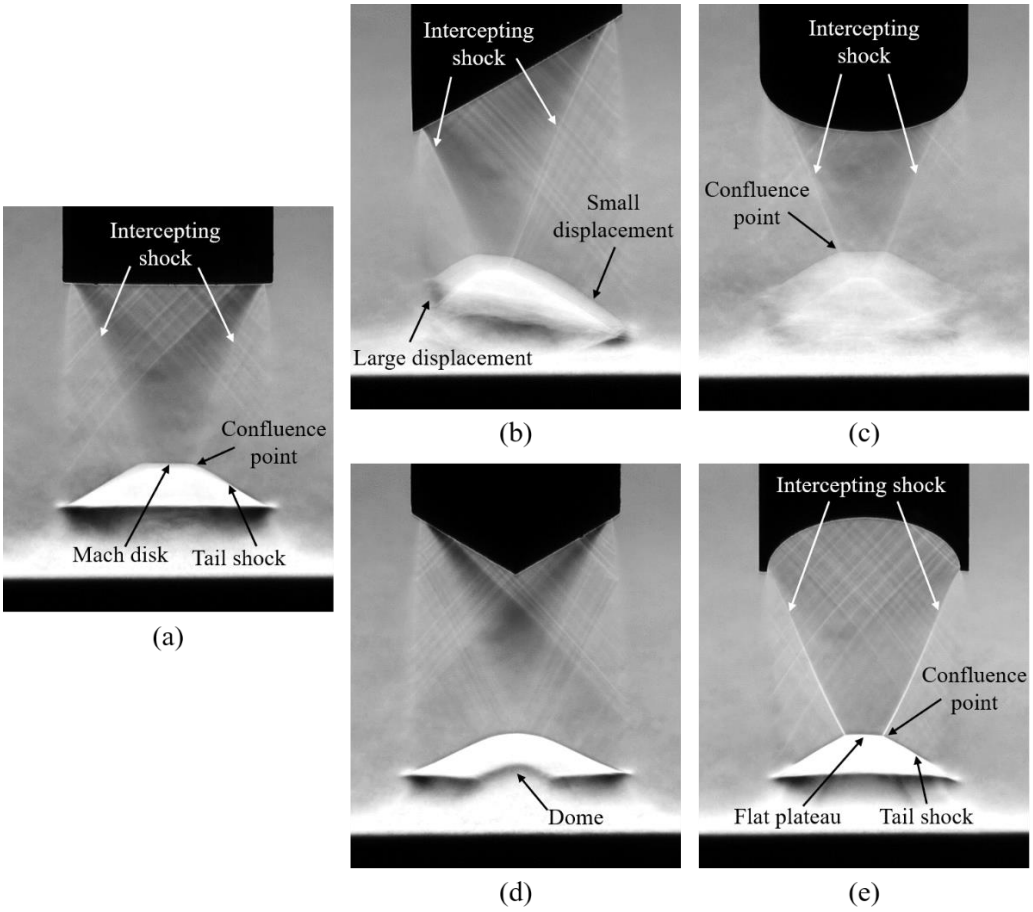

Figure 5.9: Schlieren images of M_d=1.45 impinging jets at h/D=1.5 and NPR=5 (i.e. configuration 3) for (a) baseline, (b) 30° bevelled (θ=0°), (c) 30° bevelled (θ=90°), (d) 30° double-bevelled (θ=0°) and (e) 30° double-bevelled (θ=90°) nozzles

The schlieren results of all three test cases for test configuration 3 are shown in Figure 5.9. As compared to the results in the previous two test configurations, much more significant changes to the location and geometry of the standoff shocks can now be observed. For the baseline test case shown in Figure 5.9(a), the standoff shock thickness has increased from t/D=0.08 in configuration 1 and t/D=0.12 in configuration 2 to t/D=0.23 in the current test configuration, indicating a significant increase in the three-dimensionality of the shock. There is also a drastic increase in

standoff shock distance, from s/D=0.33 in configuration 1 and s/D=0.38 in configuration 2, to s/D=0.59 in the current test configuration.

The increase in standoff shock distance is closely related to the standoff shock thickness. The underlying mechanism is likely to be related to the instability mechanism proposed by Ginzburg et al. [15], and is closely relevant to the interaction between the jet shock structures and the standoff shock. In Figure 5.9(a), a Mach disk has now clearly appeared at the centre of the standoff shock, and together with the nozzle intercepting oblique shocks as well as the tail shocks on the outer edge of the standoff shock, the three-shock confluence point is produced. According to Ginzburg et al. [15] and Kalghatgi and Hunt [123], a shear layer forms along the slip-line originating from the three-shock confluence point. As this approaches the subsonic plate boundary layer, it causes an increase in the flow pressure, leading to the occurrence of plate boundary layer separation and the formation of the stagnation bubble. Occurrence of a peripheral static pressure maximum often associated with the formation of a stagnation bubble leads to a static pressure build up behind the Mach disk when the flow in the central domain is trapped and cannot enter the mixing zone. As the pressure behind the Mach disk rises, upstream displacement of the standoff shock occurs. This motion is counteracted by the primary jet momentum and static pressure upstream of the Mach disk until a dynamic equilibrium is attained. The pressure in the central domain does not rise above the peripheral maximum, hence flow in the central domain cannot enter the mixing zone and the standoff shock remains displaced upstream.

In the case of the 30° bevelled nozzle, the schlieren images in Figure 5.9(b) and Figure 5.9(c) capture two prominent flow features not observed in any of the other test cases. Firstly, modification of the nozzle exit appears to have a much stronger and pronounced effect in influencing the geometry of the standoff shock as compared to the previous two configurations. The standoff shock appears to be severely distorted, with the tip of the standoff shock attracted to the reflection point located nearer to the longer lips of the asymmetric nozzle. Similar to the shock structures observed in the baseline case, formation of the three-shock confluence point connecting the nozzle intercepting oblique shocks, Mach disk, and tail shock can be observed. Though, it must be noted that due to considerable standoff shock instabilities, it was difficult to accurately determine if the tip of the standoff shock actually constitutes the geometry of a Mach disk. Secondly, the schlieren images captured highly unsteady behaviour of the standoff shock at multiple positions throughout its oscillation cycle. While minor oscillations or instabilities can be expected due to the local influence of turbulence, jet mixing layer, or the wall jet, this was the only test case in the entire study whereby the standoff shock waves were unstable with such a huge oscillation amplitude. In terms of oscillation amplitude, the axial displacement was observed to be much greater on the segment of the standoff shock that is nearer to the longer nozzle lip. For the same segment of the oscillating standoff shock, it does not oscillate at the same amplitude across the observed oscillation cycles. Specifically, the oscillation amplitude appears to fluctuate between low and high amplitudes between different oscillation cycles. This could also be due to the relatively low 1000 Hz image acquisition rate used here, where the camera framerate was unable to fully resolve the oscillation amplitudes.

Due to the hardware constraint, it was not possible to accurately determine the oscillation amplitude and frequency in the current study. The intercepting oblique shocks were observed to be steady throughout this entire process and did not appear to have any correlation with the motions of the standoff shock.

There could be a few possible causes of the shock instability. Unsteadiness with frequencies of below 10 Hz can occur if the stagnation bubble is repeatedly formed and swept away [123]. This does not appear to be the case in the present study, as instantaneous schlieren images with an image exposure time of 10 μs and an image acquisition rate of 1000 Hz proved insufficient in capturing time-resolved information on the oscillations. Lamont and Hunt [16] reported on the possibility of acoustic standing waves set up between the plate and any parallel surface near the nozzle, which can lead to higher frequency unsteadiness. This also does not appear to be the case as the experimental rig used in the present study did not have any parallel plates near the nozzle vicinity. Finally, the instability mechanism proposed by Ginzburg et al. [15] seemed the most likely based on similar smudged features in the schlieren images as well as the observation of strong acoustics in the surrounding space [131] during the course of the experiments in this study.

Displacement of the standoff shock is likely to be due to the occurrence of a peripheral static pressure maximum often associated with the formation of a stagnation bubble, which leads to a static pressure build up behind the Mach disk when the flow in the central domain is trapped and cannot enter the mixing zone. As the pressure behind the Mach disk rises, upstream displacement of the standoff shock occurs until the pressure in the central domain has risen to greater than the peripheral

maximum. Flow in the central domain may then enter the mixing zone, thus leading to pressure relief in the central domain and the standoff shock displaces downstream back to its original position. The entire process repeats itself, leading to the observed oscillations. Keeping in mind that all three nozzles were designed with a circumferential variation of the axial length of the nozzle lips, the pressure relief that occurs when the flow exits the nozzle is expected to be different for all three nozzles. This affects the pressure field near the standoff shock, which is closely linked to the physical mechanism involved in the upstream displacement/instability characteristics of the standoff shock. Hence, it is unsurprising that the shock instability was observed only for the bevelled nozzle.

For the 30° double-bevelled nozzle as shown in Figure 5.9(d) and Figure 5.9(e), the standoff shock in both viewpoints clearly exhibits differing geometries which are much more pronounced than the previous two configurations. At the top surface of the standoff shock, a dome geometry and a flat plateau can be observed in the θ=0° and 90° viewpoint respectively. This observation is reminiscent of the 30° double-bevelled configuration 2 test case, and the top of the standoff shock should resemble the geometry shown in Figure 5.8(c), that of a 2D bow shock. At the base of the standoff shock, a smaller dome can be observed in the θ=0° viewpoint as shown in Figure 5.9(d). While domes at a similar position have been observed in both configurations 1 and 2, the current configuration has the largest and most distinct dome formation. In the θ=90° viewpoint shown in Figure 5.9(e), the three-shock confluence point is observed although this was not the case for the θ=0° viewpoint in Figure 5.9(d). Similar to configurations 1 and 2, this is likely to be due to a lack of

well-defined intercepting shocks in the θ=0° viewpoint. Nonetheless, drastic displacement of the standoff shock has occurred with the standoff shock distance increasing from s/D=0.35 and 0.36 in configurations 1 and 2 respectively to s/D=0.52 in the current test configuration. The thickness of the standoff shock has also drastically increased from t/D=0.08 and 0.09 in configurations 1 and 2 respectively to t/D=0.23 in the current test configuration. Based on the mechanism in which the shock upstream displacement occurred, it is highly likely that a stagnation bubble has formed in the current test case, although the cross-section of the stagnation bubble is unlikely to be axisymmetric. Table 5.4 summarizes the geometrical information of the standoff shock across the three test cases in the current configuration.

Since the standoff shock in the 30° double-bevelled test case has been observed to take on a much different 3D geometry, the 3D reconstruction procedure [42] was again performed to ascertain the geometry of the standoff shock. The results from the reconstruction are shown in Figure 5.10. Some spurious surfaces at the peripheral of the reconstruction can be observed for the 30° double-bevelled test case in Figure 5.10(b) and at the bottom of Figure 5.10(d). This is an artefact of the image-processing approach adopted in the reconstruction algorithm and is not part of the shock structures. Interested readers can refer to Chapter 4 for detailed discussions on the associated reconstruction errors [42].

Based on the 3D reconstruction results, there is an obvious eccentricity in the cross-section of the 30° double-bevelled standoff shock, with much narrower shock structures in the θ=90° plane as compared to the θ=0° plane. The narrow shock structures did not even reach the nozzle throat diameter and manifested itself in

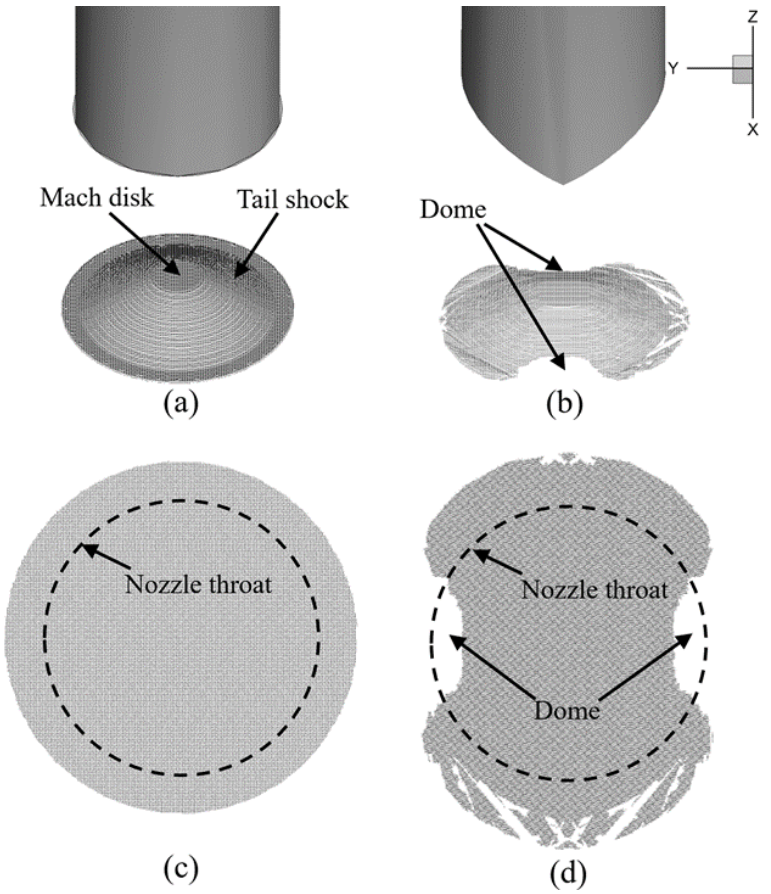

Figure 5.10: Reconstructed standoff shock geometries associated with (a) baseline and (b) 30° double-bevelled nozzles in isometric view, as well as (c) baseline and (d) 30° double-bevelled nozzle cross-sections, for h/D=1.5 and NPR=5 (i.e. configuration 3).

Figure 5.10(d) as the small dome at the base of the standoff shock. Upon closer inspection of Figure 5.9(e), the constant pressure streamlines which bound the formation of the tail shock in the θ=90° viewpoint appears to form inward towards the jet axis as compared to that in Figure 5.9(d) which forms outwards away from the jet axis. This behaviour can also be observed in the freely-exhausting jet shock structures shown in Figure 5.3. The elliptical cross-section of the constant pressure streamlines was produced due to the asymmetrical nozzle design and likely led to the asymmetric cross-section geometry of the standoff shock. Possibly, the nozzle

Table 5.4: Non-dimensional dimensions and characteristics of standoff shocks at h/D=1.5 and NPR=5 (configuration 3)

Nozzle type	Standoff shock distance (s/D)	Standoff shock thickness (t/D)	Standoff shock geometry
Baseline	0.59	0.23	Quasi-steady. Significant upstream displacement with formation of a distinct Mach disk and the three-shock confluence point.
30° bevelled	N.A.	N.A.	Highly unsteady behaviour. Largest displacement observed at the longer nozzle lips.
30° double-bevelled	0.52	0.23	Quasi-steady. Significant upstream displacement with narrower shock structures on the plane of the longer nozzle lips (θ=90° plane).

asymmetry led to an earlier flow expansion in the θ=0° plane as compared to the in the θ=90° plane. Hence, at any axial distance before the occurrence of the reflection point in the first shock cell, flow in the θ=0° plane should have a higher Mach number and lower static pressure than those along the θ=90° plane. This implies that the tail shock in the in the θ=90° plane should be weaker than that of the in the θ=0° plane, which can be achieved by either decreasing the oblique shock angle with respect to the flow, or in this case a reduction in the cross-section area of the tail shock. With the standoff shock's cross-section as shown in Figure 5.10(d), it is likely that the formation and cross-section of the stagnation bubble under the standoff shock is also affected, though there is currently no pressure data to confirm this postulation.

5.3.4 Reflection point and standoff shock relationship

Thus far, the standoff shock had been investigated by varying the independent variables; namely NPR, nozzle exit geometry and separation distance. Varying the NPR has the effect of shifting the axial position of the reflection point relative to the impingement surface and standoff shock, leading to a change in the static pressure distribution at the position of the standoff shock. The use of IO jet nozzles directly affects the overall jet shock structures emanating from the nozzles and can introduce significant variations particularly to the radial position of the reflection point. Separation distance dictates the relative distance of the standoff shocks with respect to the reflection point. Evidently, the reflection point is the dependent variable with its characteristics determined by the aforementioned independent variables. To better understand changes observed in the standoff shock properties, it is necessary to consider from the perspective of the reflection point.

For the under-expanded freely-exhausting jet as shown in Figure 5.11(a), a detailed explanation on the shock wave formations and pressure distributions have already been presented in Section 1.2.2. The two most important takeaways relevant to this section are: (1) Flow in region 3 continually undergoes expansion as it travels downstream, until it passes through the intercepting and reflected shocks to arrive at region 4 and 5 with higher static pressures of P_4 and P_5 respectively. (2) There is an adverse pressure gradient across the reflection point, and the location of the lowest static pressure lies just upstream of the reflection point. To facilitate discussions, hereinafter, the magnitude of this adverse pressure gradient will simply be referred to as the "strength" of the reflection point.

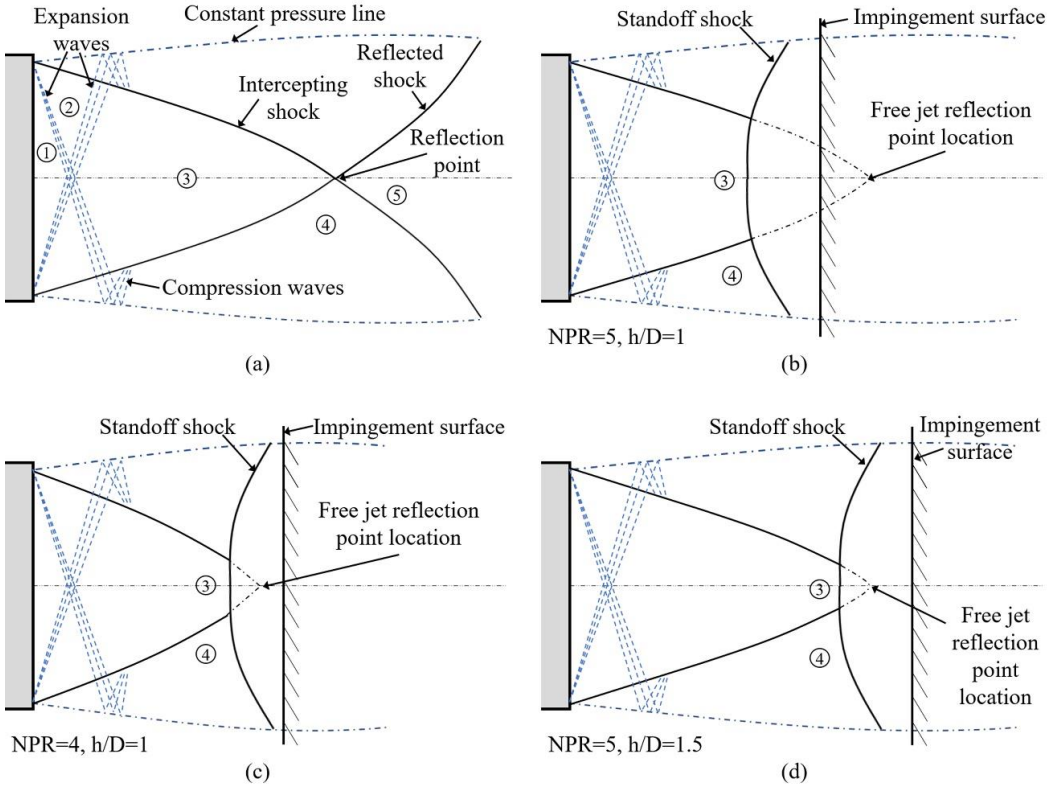

Figure 5.11: Flow schematics of an under-expanded jet under (a) freely-exhausting condition, (b) configuration 1, (c) configuration 2 and (d) configuration 3. *Not drawn to exact scale.*

In an impinging jet, a standoff shock forms ahead of the impingement surface, leading to a change in flow direction away from the central region of the impingement surface. This is shown in Figure 5.11(b), Figure 5.11(c) and Figure 5.11(d) which corresponds to flow configuration 1, 2 and 3 respectively. Since the position and strength of the reflection point determines the static pressure distribution upstream of the standoff shock, it is unsurprising that the standoff shock characteristics are dependent on it. The effects of varying the axial position, radial position, and strength of the reflection point on the standoff shock are further discussed based on the results of the three flow configurations presented in Figure 5.5, Figure 5.6 and Figure 5.9.

5.3.4.1 Effects of reflection point position

In terms of the axial position of the reflection point, configurations 1 and 3 as illustrated in Figure 5.11(b) and Figure 5.11(d) may be considered, which consist of the same jet exhausting at NPR=5 but with different relative axial position of the reflection point with respect to the impingement surface and standoff shock. For the baseline impinging jet in configuration 1, the reflection point is *downstream* of the impingement surface as shown in Figure 5.11(b). In this situation, a comparatively large diameter at the centre of the standoff shock is subjected to a lower static pressure (P_3) than its peripheral (P_4), hence leading to a stronger upstream "suction" effect in the central region of the standoff shock. The geometry of the standoff shock is affected by this pressure distribution, resulting in the convex disk geometry as observed in Figure 5.5(a). The standoff shock tapers off at the constant pressure line where the static pressure equals the ambient pressure.

In comparison, although configuration 3 has the jet exhausting at the same NPR, the reflection point is now *upstream* of the impingement surface as shown in Figure 5.11(d). The change in the relative position of the reflection point with the impingement surface (and standoff shock) led to very significant differences in the standoff shock's geometry and position. A smaller diameter of the standoff shock is now subjected to the low static pressure region 3, resulting in the formation of a smaller diameter flat plateau (i.e. Mach disk) as shown in Figure 5.9(a). Furthermore, since the relative position of the standoff shock is now much closer to the position of the reflection point, and that the static pressure P_3 is at its lowest just upstream of the reflection point, the standoff shock in configuration 3 is subjected to a stronger

upstream suction effect as compared to the flow scenario in configuration 1. This led to a greater degree of three-dimensionality in the standoff shock as previously discussed, with particularly distinct observations of the Mach disk, tail shocks and three-shock confluence point. The stronger upstream suction effect along with the build-up of static pressure behind the standoff shock as discussed earlier both contributed to the observation of a significant upstream displacement of the standoff shock.

Similar characteristics of the standoff shock in terms of upstream displacement, three-dimensionality and localized distortions to the geometry were also observed in the IO jet test cases. For the double-bevelled jet in configuration 3 as shown in Figure 5.9(d) and Figure 5.9(e), the standoff shock has undergone upstream displacement with a greater degree of three-dimensionality relative to its counterpart in configuration 1 (see Figure 5.5(d) and Figure 5.5(e)). Furthermore, in the $\theta=90°$ viewpoint as shown in both Figure 5.5(e) and Figure 5.9(e), the most upstream position of the standoff shock is always bounded by the intercepting oblique shocks at the three-shock confluence point, consistent with the hypothesis of a lower static pressure and stronger upstream suction effect in the central region of the jet as compared to its peripheral when a reflection point is present. In contrast, the $\theta=0°$ viewpoint shown in both Figure 5.5(d) and Figure 5.9(d) has no clear pair of intercepting shock, resulting in a much more gradual radial variation of the static pressure upstream of the standoff shock. The effects on the standoff shock are reflected by the formation of a smooth convex disk geometry with no sharp kinks that is indicative of the three-shock confluence point.

In terms of the radial position of the reflection point and its influence on the standoff shock, this is best exemplified by the θ=0° viewpoint of the bevelled nozzle. Results from all three configurations indicated a shift of the standoff shock in the direction of the longer nozzle lip towards where the reflection point is biased. From the results presented in Figure 5.5(b) and Figure 5.6(b), the shift in standoff shock appears to be greater and much more apparent in configuration 2 than in configuration 1. This agrees well with the non-dimensional parameters provided in Table 5.1, which indicates that the NPR=4 jet used in configuration 2 possessed a greater radial shift of the reflection point away from the jet axis as compared to the NPR=5 jet used in configuration 1. The part of the standoff shock that is exposed to the low-pressure region upstream of the reflection point is always at the most upstream position and bounded by the intercepting shock, which is again consistent with what is to be expected to occur from the upstream suction effect of the reflection point. The preceding arguments indicate that the effects of the reflection point location on the standoff shock are applicable across all test nozzles investigated in this study.

Schlieren videos were taken to further understand the exact process in which upstream displacement of the standoff shock occurred. At the separation distance of h/D=1.5, the NPR was gradually increased from NPR=4 to NPR=5 and schlieren videos were taken at 1000 FPS. In the baseline nozzle, changes to both geometry and position of the standoff shock was gradual as the NPR was increased. At approximately NPR=4.7, the thickness and position of the standoff shock undergo a very sudden and abrupt jump. The reflection point was observed to be just upstream and about to intersect with the standoff shock when the jump occurred, as shown in

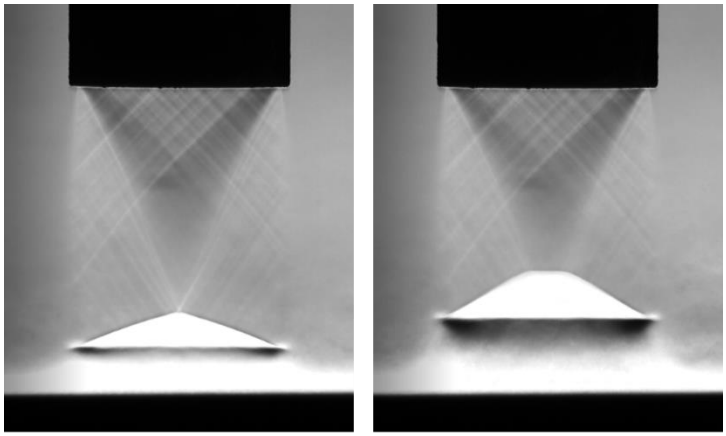

(a) (b)

Figure 5.12: Time-sequenced images of M_d=1.45 baseline impinging jet at h/D=1.5, (a) just before (b) just after shock jump

Figure 5.12(a). Interestingly, when the experiments were repeated in reverse order by decreasing the NPR starting from NPR=5, a sudden and abrupt decrease in standoff shock thickness and distance occurred at NPR=4.5 instead. Below this value, the standoff shock thickness and distance slowly decreased with the NPR. This observation suggests the presence of a hysteresis effect associated with the standoff shock, although the underlying physical mechanism is still unclear at this point.

For the 30° bevelled nozzle, the instability started to occur between NPR=4.8 to 4.85 as the NPR was increased, with the frequency and amplitude of the oscillations visually observed to increase at higher NPRs. The reflection point was approximately 0.12D upstream of the tip of the standoff shock (see Figure 5.13(a)) when low frequency and small amplitude instabilities started occurring. Figure 5.13(a) and Figure 5.13(b) show the approximate minimal and maximal positions of the small amplitude oscillations. As the NPR further increases from NPR=4.8 to 4.85, large amplitude oscillations at much higher frequencies were observed, based on

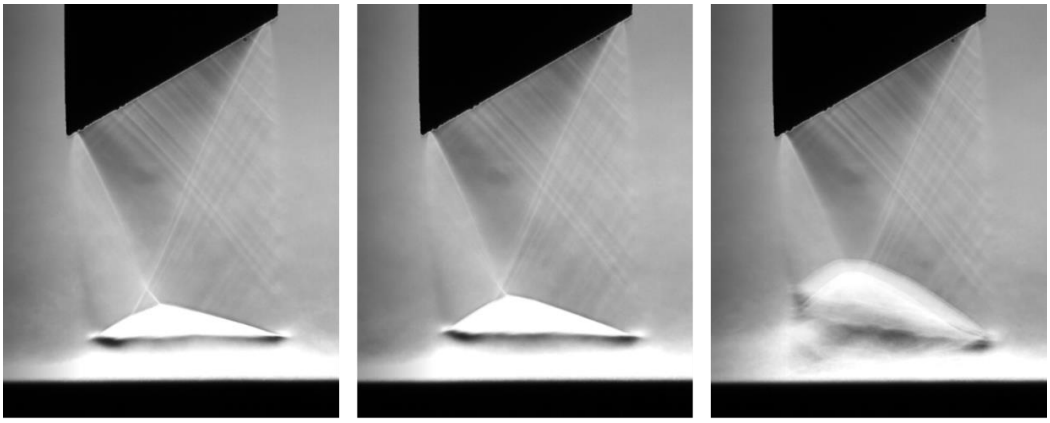

Figure 5.13: Time-sequenced images of M_d=1.45 30° bevelled impinging jet at h/D=1.5 for θ=0°, (a) minimal position of small amplitude and low frequency oscillations (b) maximal position of small amplitude and low frequency oscillations, also just before large amplitude and high frequency oscillations (c) large amplitude and high frequency oscillations.

significant image blurring as shown in Figure 5.13(c). Note that Figure 5.13(b) illustrates the reflection point just upstream of the tip of the standoff shock and is also just before the onset of the large amplitude and high frequency oscillations. When the experiments were carried out in reverse order by reducing the NPR from 5, the unstable standoff shock became stable again at the same NPR range of 4.8 to 4.85.

For the 30° double-bevelled nozzle, the sudden and abrupt increase in standoff shock thickness and distance occurred at NPR=4.92 as the NPR was increased, and similar to the baseline test case, the reflection point was just upstream and about to intersect the standoff shock when it occurred (see Figure 5.14(a)). The abrupt decrement was observed at NPR=4.8 when the experiments were conducted in reverse order. Similar to the baseline test case, there appears to be a hysteresis effect associated with the standoff shock jump phenomenon. In all test cases, the reflection points clearly had

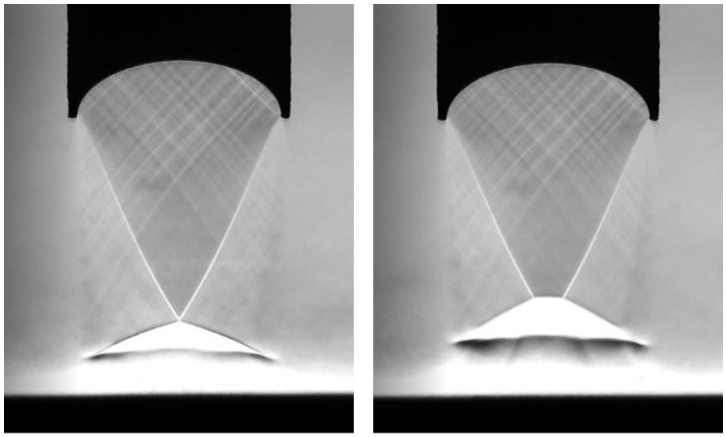

(a) (b)

Figure 5.14: Time-sequenced images of M_d=1.45 30° double-bevelled impinging jet at h/D=1.5 for θ=90°, (a) just before (b) just after shock jump

a significant role leading up to the onset of standoff shock thicknesses and distances jump in the baseline and 30° double-bevelled test cases, and standoff shock instabilities for the 30° bevelled test case. Since just upstream of the reflection point there is a region of low static pressure, it is perhaps unsurprising for the observed changes to occur when the reflection point approaches very close to the standoff shock. Nonetheless, the manner in which it occurred remains very intriguing, particularly for the observation of the hysteresis effect associated with the baseline and double-bevelled standoff shocks, as well as a change in the oscillatory behaviour of the bevelled standoff shock when the NPR was further increased. Note that orthogonal views for the IO jets did not reveal additional information and were therefore not included in the discussions of the results.

5.3.4.2 Effects of reflection point strength

The strength of the reflection point is influenced through variation of the NPR. Since the axial position of the reflection point can also lead to different pressure

distributions in front of the standoff shock, it is necessary to compare two configurations that have similar reflection point axial location with respect to the standoff shock, but with differing pressure gradients across the reflection point. Configurations 2 and 3 both ensures that the impingement surface is situated downstream of the reflection point location but still within the first jet shock cell in all three test cases, as seen in the flow schematics presented in Figure 5.11(c) and Figure 5.11(d). This was intentionally designed based on the available geometric information in Table 5.1, Table 5.2 and Table 5.3. Since the higher under-expansion exhaust condition of the jet in configuration 3 will create a stronger reflection point, the strength of the reflection point may then be investigated.

Results presented in the preceding sections (see Figure 5.6 and Figure 5.9) have already demonstrated significant changes in the standoff shock properties across configurations 2 and 3. In particular, the baseline test cases display qualitatively similar standoff shock structures with the formation of a Mach disk, tail shocks and the three-shock confluence point observed, albeit with configuration 3 having much more distinct shock features than configuration 2. Based on Ginzburg et al. [15] and Kalghatgi and Hunt [123], the flow dynamics behind the standoff shock should be very similar, where the shear layer originating from the three-shock confluence point eventually leads to a build-up of static pressure behind the standoff shock. Nonetheless, the standoff shock features in configuration 3 were much more accentuated, with a significantly higher standoff shock thickness and distance as compared to configuration 2. With similar flow dynamics occurring behind the standoff shock, it is very likely that the static pressure in front of the standoff shock

played a significant role in leading up to the observed key differences of the standoff shock features between configurations 2 and 3. The same argument can be made for the 30° double-bevelled test case, where the standoff shock in configuration 3 had larger standoff shock thickness and distance as compared to that in configuration 2.

For the 30° bevelled nozzle, the standoff shock in configuration 3 (Figure 5.9(b) and Figure 5.9(c)) was highly unsteady and display large amplitude oscillations near the longer nozzle lip with relatively smaller amplitude oscillations on the shorter nozzle lip side. It may be possible that the difference in upstream static pressure distribution contributed to the difference in oscillation amplitude on the two sides of the nozzle lips. Overall, due to very significant changes in the properties of the standoff shock when comparing across configurations 2 and 3, it is likely that the behaviour of the standoff shock is highly dependent on the strength of the reflection point, whereby a stronger reflection point is expected to lead to more significant changes in terms of standoff shock geometry, position and stability conditions.

5.4 Summary

The properties of the standoff shock have been known to be a strong function of NPR and separation distance based on the literature of supersonic impinging jets. In this study, traditional schlieren visualization and a novel 3D shock reconstruction technique were performed on moderately under-expanded IO jets impinging normally upon a flat plate at small separation distances. By examining the geometry, position and stability properties of the standoff shock at three different flow configurations, there are conclusive evidences that the standoff shock is also sensitive

to the nozzle exit geometry. Some of the more notable observations were made in flow configuration 3, where eccentric cross-section of the standoff shock was observed for the 30° double-bevelled nozzle, and large amplitude and asymmetric standoff shock oscillation was observed for the 30° bevelled nozzle.

The strength and location of the reflection point were identified as the major contributing factors leading to the observed changes in the standoff shock properties. The reflection point is formed when the initial oblique shocks intercept to form the reflected shocks. Hence, there is an adverse pressure gradient across the reflection point, and the location just upstream of the reflection point must have the lowest static pressure. As a result, the reflection point acts as a region of low pressure on the top side of the standoff shock, leading to a localized upstream suction effect. This conjecture is consistent with the schlieren visualization results where the standoff shocks were observed to be attracted to the reflection point. In the case of the IO jet nozzles, this led to asymmetric distortions of the standoff shock, and the distortion was more pronounced when a stronger reflection point was present.

At the separation distance of h/D=1.5, schlieren videos of the standoff shock were taken as the NPR was slowly increased from NPR=4 to NPR=5. When the reflection point was initially far from the standoff shock but gradually moving towards it, the standoff shock from all three nozzles revealed gradual upstream displacement and geometrical modifications. As the NPR increases further, the reflection point approaches the standoff shock until it is just upstream of it, and a sudden and abrupt jump in both the position and geometry of the standoff shock was observed for the baseline and 30° double-bevelled nozzle. For the 30° bevelled nozzle, small

amplitude oscillations were found to occur when the reflection point was about 0.12D from the standoff shock, and as the reflection point approaches even closer, large amplitude oscillations start to occur. These observations strongly suggest the importance of the reflection point in determining the characteristics of the standoff shock. Future studies on the impingement zone based on surface plate pressure and 3D-3C PIV measurements could shed more light on the above observations.

Chapter 6 Schlieren Image Velocimetry Based on the Variational Optical Flow Technique

6.1 Overview

Schlieren image velocimetry based on the optical flow technique is totally non-intrusive and has the potential to measure a dense velocity field. Physics or empirical observations can also be incorporated into the objective function which allows the solutions to be physically meaningful. There are two main aspects that must be considered in order to achieve accurate SIVOF. The first aspect is related to optimization of the schlieren images based on the requirements of the optical flow technique, which is generally not as robust as cross-correlation based techniques. Since schlieren images are inherently different from the rigid body motion images which optical flow typically handles, it is important to optimize the images in a systematic manner in order to ensure a well-conditioned problem. In Section 6.2, this will be explored by considering the limitations of optical flow and the stringent requirements a supersonic flow places upon the experimental design.

The second aspect is the optical flow algorithm which originated from the computer vision community, hence necessitating further development in order to apply it for SIV of supersonic jet flows. In Section 6.3, the in-house optical flow algorithm is presented by sub-dividing it into the *model* and the *method* following the conventions of Sun et al. [89] for better clarity. The *model* refers to the optical flow's objective function and the *method* refers to the numerical schemes involved in minimizing it. Validation of the optical flow algorithm based on synthetic schlieren images is also presented, and the in-house optical flow algorithm is benchmarked against a

competitive open source optical flow algorithm. In Section 6.4, the optical flow algorithm is applied to time-resolved schlieren images of an over-expanded supersonic jet operated at NPR=2.8. The SIVOF results are compared with double-frame PIV results.

6.2 Optimization of schlieren images for SIVOF

6.2.1 Preliminary analyses

Optimization of speckle- [52] and particle-images [132] for optical flow analysis have been studied in the context of low speed flows. Schlieren images are very different from speckle- or particle-images due to the integrative nature of schlieren systems. For jet flow issuing from a circular nozzle, the flow field is inherently 3D, and the integrative nature of schlieren may be problematic as there is no extra degree of freedom to decompose schlieren images into 2D planes at specific locations. This integrative effect is particularly severe near the jet core region, where the light rays passes through the jet potential core and both sides of the shear layer. In other words, for a schlieren image, spatial structures near the jet centreline cannot be expected to provide information on the jet centreline velocity, as it also contains information of the shear layers. The integrative effect is less severe at the outer shear layers away from the jet centreline, since the integrated distance of the light path through the disturbance created by the jet flow is relatively smaller. In fact, the jet peripheral is where only the jet shear layers are imaged. Fortunately, this is also the region where convective Mach number of spatial structures are of interest. In addition, for time-resolved schlieren images of supersonic jets, it has been observed that turbulent structures may disappear and cannot be faithfully tracked for extended number of

image frames. This may possibly be attributed to the integrative effect of schlieren systems, diffusive behaviour of fluid flows or 3D effects of turbulence. Regardless of the cause, this represents a deviation from the basic optical flow assumption whereby brightness constancy is assumed.

In this study, the circular nozzle has a design Mach number of 1.45 at NPR=3.4. Under the perfectly expanded exhaust condition, the convective velocity of spatial structures was estimated to be approximately u_c =400 ms^{-1}. Based on these parameters, a systematic study to optimize schlieren images for SIVOF is presented in Section 6.2.2, where the focus will be on the image spatial resolution, exposure time and framing rate requirements. In Section 6.2.3, an alternate experimental setup is proposed to obtain images well-suited for optical flow.

6.2.2 Image acquisition procedures

6.2.2.1 Image spatial resolution

In this systematic study, a 1024px × 1024px resolution IDT NX4-S1 camera with 105 mm camera lens was used in the modified Z-type schlieren set-up previously presented in Section 3.2. Based on Eq. (6.1), the pixel-to-world magnification factor, M, was experimentally determined to be approximately 0.195 mm/pixel. Since optical flow is capable of generating one velocity vector per pixel, the velocity vector field is expected to have a resolution of 0.015D. The tomographic PIV performed on a supersonic jet at similar flow conditions [48] had a slightly lower resolution of 0.017D, hence it appears that the required spatial resolution can be easily achieved without additional efforts to optimize it. Note that even for ultrahigh-speed cameras such as the Photron SAX2 or Phantom v2512, the magnification factor of captured

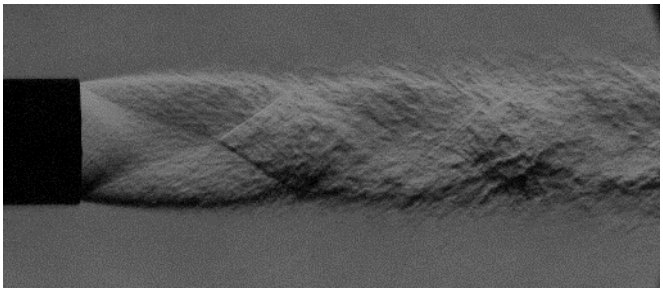

Figure 6.1: Schlieren image of under-expanded jet at NPR=5, captured using the Phantom v2512 ultrahigh-speed camera, with an exposure time of 0.77 µs

schlieren images based on the existing modified Z-type schlieren set-up was approximately 0.13-0.17 mm/pixel, translating to an even higher vector resolution of 0.01-0.013D. An example of the image captured using the Phantom v2512 at 166 kHz image acquisition rate is presented in Figure 6.1. Finally, it must be mentioned that it is not reasonable to expect a spatial structure to be represented using a single velocity vector even though optical flow can achieve one vector per pixel. A more conservative and reasonable estimate for the size of the smallest spatial structure that can be accurately resolved with the optical flow technique would be 5px × 5px.

$$M = \frac{Real\ world\ reference\ object\ (mm)}{No.\ of\ pixels\ of\ reference\ object\ (px)} \tag{6.1}$$

6.2.2.2 Image exposure time

The image exposure time is typically limited by the camera and LED light source. For supersonic jet applications, a lower exposure time is required to freeze the motion of turbulent structures and prevent image blurring. In this study, a continuous LED light source was used, and the smallest exposure time available to the IDT NX4-S1 camera was 1 µs. This appears to be sufficient based on the schlieren images of both

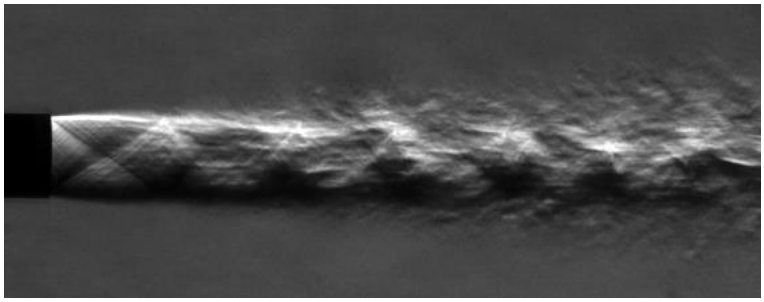

(a)

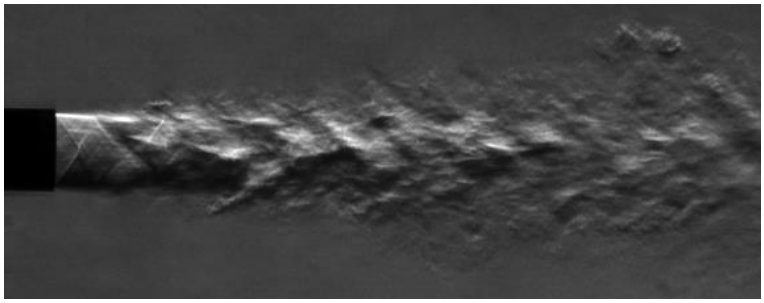

(b)

Figure 6.2: Schlieren images with 1 μs exposure time. (a) Under-expanded jet at NPR=4 and (b) over-expanded jet at NPR=2.8.

under-expanded and over-expanded test cases (Figure 6.2), with turbulent structures captured without blurring effects.

6.2.2.3 Image framing rate

The optical flow technique required much higher image framing rates as compared to cross-correlation methods in order to accurately recover the velocity of small turbulent structures. This can be attributed to two main aspects of the optical flow algorithm. (#1) The *intrinsic limitation of the multi-resolution scheme*, which consists of image pyramids built using image subsampling. The image subsampling can lead to a loss of image details, particularly when the size of the spatial structures is smaller than its displacement in the next image frame. This is an intrinsic limitation of optical flow algorithms that adopts the multi-resolution scheme, and it implies that

there is a relationship between the size of turbulent structures and the camera framing rate. (#2) The *optimum pixel displacement for optical flow*. At any single image pyramid level, the image velocities can be obtained by minimizing the optical flow objective function presented in Eq. (2.14). Since Eq. (2.14) consist of image derivatives (i.e. I_x and I_y), the pixel displacement across two image frames cannot be too large. The optimum pixel displacement for optical flow will be illustrated with a simple numerical experiment.

For the first consideration (#1), it is important to ensure that the size of the spatial structures is larger than their motions due to the limitations of the multi-resolution scheme previously discussed in the literature review. Based on this requirement, the relationship between the camera framing rate and the magnification factor, convective velocity and size of the smallest spatial structures that is to be resolved can be given as :

$$f_s = \frac{u_c}{spatial\ size\ (mm)} = \frac{u_c}{M \times spatial\ size\ (px)} \tag{6.2}$$

Based on the same experimental set-up in Section 6.2.2.1 where the magnification factor was determined to be approximately M =0.195 mm/pixel, and using a convective velocity estimate of 400 ms^{-1}, the relationship between the size of spatial structures and framing rate requirements calculated based on Eq. (6.2) is presented in Table 6.1.

Having presented the framing rate requirements based on the intrinsic limitations of multi-resolution schemes, the attention is now directed towards the second

Table 6.1: Framing rate requirements with corresponding spatial structure size, based upon intrinsic limitations of multi-resolution schemes

Size of spatial structures (mm)	Size of spatial structures (pixels)	Framing rate required (kHz)
1	5	400
3	15	133
5	26	80
7	36	57
9	46	44

consideration (#2) – understanding the optimum pixel displacements for best optical flow performance. At the coarsest image resolution of the image pyramid, the largest motions of the spatial structures in an image can be recovered. Using a standard subsampling factor of 0.5 and a maximum limit of pixel motions to be approximately 0.5 pixels for best results, the largest magnitude of image motion that can be recovered accurately for *k* number of pyramid levels is given by:

$$u_{max} = 0.5 * 2^{k-1} \tag{6.3}$$

$$k - 1 = \frac{log\left(\frac{min(Im\ size)}{16}\right)}{log(2)} + 1 \tag{6.4}$$

Numerical tests involving synthetic particle-image data were performed to illustrate the errors associated with pixel motions that are larger than 0.5 pixels. A 800px × 600px synthetic particle-image pair (i.e. Img1 and Img2) was generated from PIVlab 1.4 [133], with the particle simulation parameters presented in Table 6.2. Optical

Table 6.2: Synthetic particle-image generation parameters

Particle simulation parameters	Value
Flow simulation	Single rankine vortex
Core radius [px]	100
Maximum displacement [px]	5
Vortex centre (x, y)	(200, 300)
Image size (x, y) [px]	(800, 600)
No. of particles	200,000
Particle diameter [px]	3
Size variation [px]	0.5
Sheet thickness	0.5
Noise	0.001
Random z-position [%]	10

flow based on the procedures laid out by Sun et al. [89] was performed on the synthetic particle-image pair to obtain a 800px × 600px velocity field (i.e. ground truth, uv_{gt}). The ground truth was then scaled by a factor of 1, 2, 3 and 4, and using the scaled ground truths, image warping was performed on the first image of the synthetic particle-image pair (Img1) using bi-cubic interpolation, leading to synthetically generated particle-images (i.e. syn_Img2). Optical flow analysis was then performed on Img1 and syn_Img2 for each of the 4 sets of synthetic particle-image pair, and the velocity fields obtained (i.e. uv*1, uv*2, uv*3 and uv*4) were compared against its corresponding scaled ground truth. The average endpoint error (AEPE), defined as the average Euclidean distance between the computed and

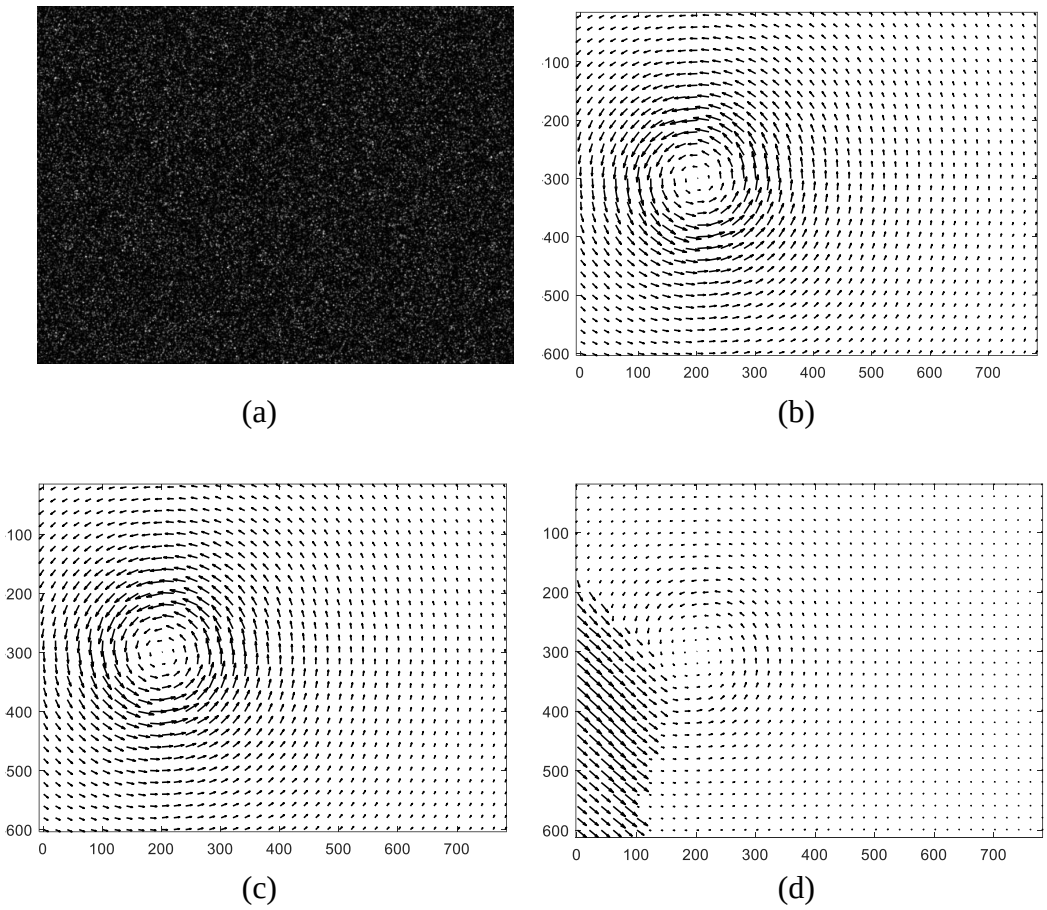

Figure 6.3: Numerical test using synthetic data. (a) Synthetic particle-image (Img1), (b) ground truth velocity vector field (uv_{gt}), (c) uv*3 and (d) uv*4. *All velocity fields obtained from optical flow technique are illustrated at reduced resolution*.

Table 6.3: Error estimates against pixel displacements

	Pixel max. displacement in original 800 x 600 image	Pixel max. displacement in coarsest level of 6-level pyramid	AEPE
uv*1	5	0.16	0.077
uv*2	10	0.31	0.189
uv*3	15	0.47	0.377
uv*4	20	0.63	4.126

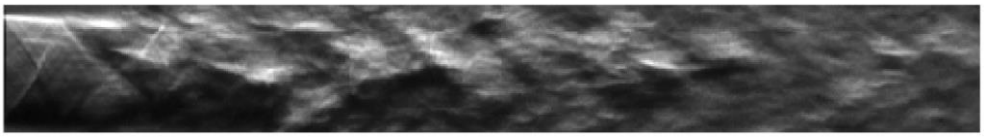

Figure 6.4: Schlieren image of an over-expanded jet (NPR=2.8)

ground truth vectors (L2-norm), is computed and presented in Table 6.3, along with information on the maximum pixel displacement at the coarsest resolution level.

From the qualitative vector results presented in Figure 6.3, uv*3 appears to be very close to the ground truth while uv*4 has obvious errors and deviates sharply from the ground truth. From Table 6.3, uv*3 has a pixel displacement of lower than 0.5 at the coarsest level of the image pyramid, with an AEPE of less than 1. In contrast, uv*4 has a pixel displacement of 0.63 which is above the optimal value of 0.5, and it can be observed that the AEPE has increased drastically. These results indicate that the optimal pixel displacement should be 0.5 or lower for multi-resolution based optical flow algorithms.

Based on a 0.5-pixel displacement at the coarsest pyramid level for best optical flow performance, Table 6.4 which relates the number of pyramid levels to framing rate requirements is presented. It can be readily observed that an increase in the number of pyramid levels leads to lower framing rate requirements. At this point, it is necessary to comment on an important aspect of the multi-resolution schemes. Velocities in the streamwise direction of the supersonic jet are expected to be much larger than velocities in the radial direction. The use of a highly rectangular experimental image such as the one shown in Figure 6.4 is common as a reduction in

Table 6.4: Number of pyramid levels and framing rate requirements for average AEPE of less than 1, based upon 0.5-pixel displacement at coarsest pyramid level for best performance

Number of pyramid levels	Max. displacement in original image (pixels)	Framing rate requirements
2	1	>2,000,000
3	2	1,020,000
4	4	510,000
5	8	255,000
6	16	128,000
7	32	64,000
8	64	32,000

the image field-of-view can increase camera framing rates for high speed applications. However, this tends to limit the number of pyramid levels as it is determined based on the dimension of the shorter image length. Hence, in order to ensure sufficient pyramid levels in the longitudinal direction, different subsampling factors in the longitudinal and transverse direction can be useful when highly rectangular experimental images are used. This approach deviates from traditional optical flow algorithms whereby subsampling factors tend to be the same in both directions. It should be noted that the use of different subsampling factors in both directions can be replaced by padding the image such that the length in both directions are the same. This strategy can increase the number of image pyramid levels, leading to lower framing rate requirements as shown in Table 6.4. However, it should be noted that the increase in pyramid levels can also lead to larger round off and interpolation errors. The intrinsic limitation of multi-resolution schemes does not change as the

requirement of the motion of the spatial structure being smaller than the size of the spatial structure itself still holds.

Based on the above analysis, the minimum framing rate of camera for accurate optical flow analysis can be determined by the following steps:

1. Determine number of pyramid levels available from images.
2. Assuming an AEPE of less than 1 is desirable, determine framing rate requirement from Table 6.4.
3. Determine size of smallest spatial structure (pixels) observed in schlieren images.
4. From Table 6.1, determine framing rate requirement based on size of smallest spatial structure (pixels).
5. From step 2 and 4, select the higher framing rate requirement.

For the current experimental set-up, the optimal camera framing rate is approximately 400,000 FPS. This corresponds to approximately 2.5 μs time delay between two consecutive images.

6.2.3 Double-camera schlieren setup

The requirement of a high framing rate camera has been established in the previous section. While there are cameras that are able to provide over 1,000,000 FPS at reduced resolutions, it is a very cost-prohibitive option to most researchers. To circumvent this problem, a modified Z-type double-camera schlieren experimental set-up reminiscent of the two-spark schlieren system of Papamoschou [49] is

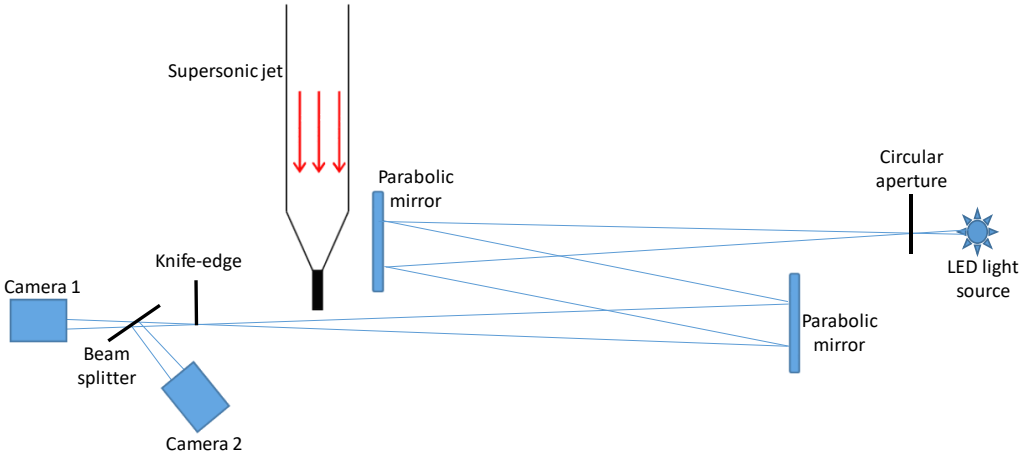

Figure 6.5: Single knife-edge with double camera configuration of modified Z-type schlieren set-up

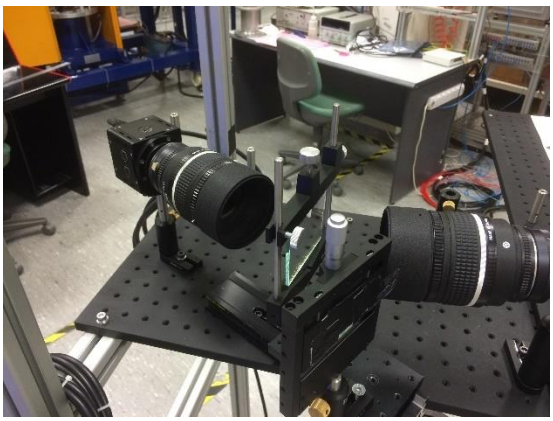

Figure 6.6: Experimental set-up for 27^{o} angle of incidence at beam splitter

proposed, based on the modified Z-type single-camera schlieren setup previously presented in Section 3.2. An additional IDT NX4-S1 cameras fitted with 105 mm lens and a 50-50 plate beam splitter are introduced into the schlieren system. As shown in Figure 6.5, a beam splitter and an additional camera are added to the schlieren setup after the knife-edge. The beam splitter transmits 50% of light into camera 1 and reflects 50% of light into camera 2. The two cameras can be triggered independently with a BNC model 575 pulse generator. By triggering both cameras

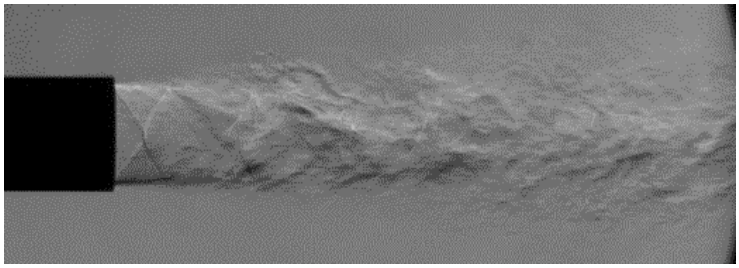

(a)

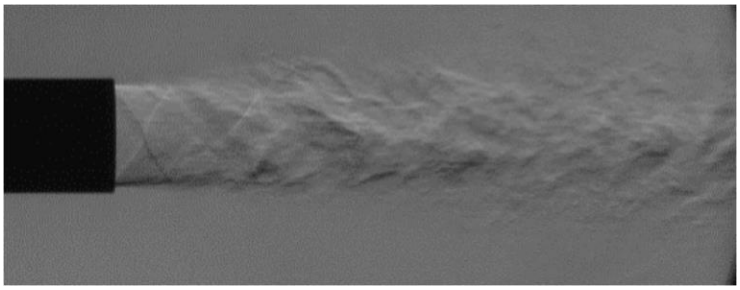

(b)

Figure 6.7: Sample schlieren images from (a) camera 1 and (b) camera 2, with a time delay of 5 μs

with a short time delay, successive images of the supersonic jet flow which fulfils the framing rate requirement of 2.5 μs time delay can be obtained. Note that Figure 6.5 is not drawn to scale.

This experimental set-up is attractive because any two similar cameras of the same make and model that allows external triggering can be used, thus offering a relatively cost-effective optical flow platform. Extending this concept to two double-frame PIV cameras with a synchronised pulsed light source can allow for a "4-frame time-resolved schlieren", while making use of high-speed cameras can allow framing rates to be increased. A sample of schlieren images captured with this experimental setup is presented in Figure 6.7. Notably, while the same structures can be observed in both images, the two images are still slightly different in terms of the overall image

contrast and brightness. This can be attributed to factory miscalibration of the two same model cameras and as such, the captured images were of little use in optical flow analysis for the current study. Nonetheless, there is potential in the proposed alternative double-camera schlieren setup if well-calibrated cameras are available.

6.3 Variational optical flow algorithm

6.3.1 Optical flow model

The optical flow *model* was derived based on the work of Horn and Schunck [78] and Corpetti et al. [83]. The energy functional can be subdivided into the data (E_D) and regularization term (E_S):

$$E = E_D + \tau E_S \tag{6.5}$$

where τ represents the relative weight assigned to the regularization term. For the data term, the original Horn and Schunck's formulation previously presented in Eq. (2.14) was replaced with:

$$E_D = \int \rho_D\{I_t + I_x u + I_y v\}\, dxdy \tag{6.6}$$

where ρ_D is a robust penalty function in place of the original quadratic penalty function. For the regularization term, the original Horn and Schunck's assumption of a smoothly varying velocity was replaced with:

$$E_S = \int \begin{Bmatrix} |\nabla \cdot \vec{u} - \xi|^2 + \lambda_1 \rho_S(|\xi - \xi_c|) + \\ |\nabla \times \vec{u} - \zeta|^2 + \lambda_2 \rho_S(|\zeta - \zeta_c|) \end{Bmatrix} dxdy \tag{6.7}$$

$$\nabla \cdot \vec{u} = u_x + v_y \tag{6.8}$$

$$\nabla \times \vec{u} = v_x - u_y \tag{6.9}$$

The terms on the left of Eq. (6.7) are a least squares minimization that enforces the auxiliary field variables ξ and ζ to comply with the divergence estimates, $\nabla \cdot \vec{u}$, and vorticity estimates, $\nabla \times \vec{u}$, respectively. The terms on the right of Eq. (6.7) are a smoothness assumption of ξ and ζ, where the subscript c represents the immediate neighbourhood of pixels. ρ_s represents the robust penalty function associated with the smoothness assumption of ξ and ζ, λ_1 represents the weight assigned for a smooth divergence field and λ_2 represents the weight assigned for a smooth vorticity field.

As compared to the original Horn and Schunck's objective function (Eq. (2.14)), two main differences can be observed for the current model. Firstly, the regularization term E_S is now derived based on a second order div-curl regularizer [134], which is advantageous for fluid flow applications as it can avoid penalizing divergence and vorticity estimates [82, 83]. In terms of implementation, two auxiliary field variables in ξ and ζ were introduced to replace the second order div-curl regularizer [134] with coupled first order regularizers [82, 83], at the expense of the additional field variables. This increases the number of computations but effectively reduces the Euler-Lagrange equations from fourth order PDEs to coupled second order PDEs, which has better numerical stability and is much easier to solve. Secondly, the introduction of robust penalty functions [90] in ρ_D and ρ_S, in place of quadratic

penalty functions, allow for abrupt deviations in the data or regularization term. The penalty functions used for both data (ρ_D) and regularization term (ρ_S) were the same – the slightly non-convex Charbonnier penalty function which can be expressed as:

$$\rho(x) = (x^2 + \varepsilon^2)^\sigma \tag{6.10}$$

where $\varepsilon = 0.001$ and $\sigma = 0.45$. The slightly non-convex Charbonnier penalty function was selected as it has been demonstrated to have the best performance based on past parametric studies [89, 96].

6.3.2 Optical flow method

The *method* used in the in-house optical flow algorithm closely followed the work of Sun et al. [89, 96] and Corpetti et al. [83], and a pseudo-code that highlights the key features of the in-house optical flow algorithm is presented in Appendix A2. Raw schlieren images obtained directly from the experiments were first pre-processed using the structure-texture decomposition method [94, 95]. The structural part is given by the solution of:

$$\min_{I_{struct}} \int \left\{ |\nabla I_{struct}| + \frac{1}{2\theta}(I_{struct} - I_{raw})^2 \right\} dxdy \tag{6.11}$$

where θ =0.125, a small value hyperparameter assigned to ensure a good approximation of the structural part with the original raw image, and the blended textural part (pre-processed image) was obtained by:

$$I = I_{raw} - \lambda_3 I_{struct} \tag{6.12}$$

where λ_3=0.95 represents the blending factor. With the pre-processed images, image pyramids were built for the coarse-to-fine multi-resolution scheme, using a subsampling factor of 0.5 for the first GNC loop and 0.8 for subsequent GNC loops (refer to Appendix A2).

The robust penalty functions as described in Eqs. (6.6) and (6.7) can be minimized directly, or it can be replaced by a classical half-quadratic minimization problem. The second option was preferable as it allowed sparse and linear systems to be formulated, for which efficient solvers already existed in MATLAB. Following the procedures as described in Black and Rangarajan [90], the robust penalty function can be expressed as:

$$\rho(x) = \min_{z} zx^2 + \psi(z) \tag{6.13}$$

The expression for $\psi(z)$ is not central to the discussion here and can be found in Black and Rangarajan [90]. z is a weighting variable and its closed form solutions for fixed x [90] is given by:

$$z = \frac{\rho'(x)}{2x} \tag{6.14}$$

Hence, this allowed the minimization problem of $\rho(x)$ in Eq. (6.13) to be solved by the iteratively reweighted least squares (IRLS) approach. For fixed weighting variable z, the minimization with respect to x is a least squares problem, and for fixed x, the optimal solution to z which satisfy Eq. (6.13) is given in Eq. (6.14).

For the four field variables u, v, ξ and ζ, alternate minimization can be performed on the respective Euler-Lagrange PDEs that satisfies Eq. (6.5). The Euler-Lagrange PDEs that satisfies Eq. (6.5), with respect to u, v, ξ and ζ are:

$$z_D\big(I_t + I_x u + I_y v\big)I_x - \tau\big(u_{xx} + u_{yy} + \zeta_y - \xi_x\big) = 0 \tag{6.15}$$

$$z_D\big(I_t + I_x u + I_y v\big)I_y - \tau\big(v_{xx} + v_{yy} - \zeta_x - \xi_y\big) = 0 \tag{6.16}$$

$$\xi - \lambda_1 z_\xi\big(\xi_{xx} + \xi_{yy}\big) = u_x + v_y \tag{6.17}$$

$$\zeta - \lambda_2 z_\zeta\big(\zeta_{xx} + \zeta_{yy}\big) = v_x - u_y \tag{6.18}$$

where z_D, z_ξ and z_ζ are the sets of weights associated with the three robust penalty functions in Eqs. (6.6) and (6.7). z_D is related to the data term which contains u and v, and z_ξ and z_ζ are related to regularization of the auxiliary field variables ξ and ζ respectively. The three set of weights were updated using the IRLS procedure as described earlier, and this is presented as IRLS 1, 2 and 3 in the pseudo-code (see Appendix A2). In order to solve the PDEs, discretization was performed, and MATLAB built in linear solver were used.

In addition, a linearization step was introduced for the image velocity. Using uv to represent the velocity matrix containing both u and v:

$$uv = \widetilde{u}\widetilde{v} + duv \tag{6.19}$$

where $\widetilde{uv}$ represents current velocity estimates, and duv represents the flow increment to be calculated. This step was necessary as the image velocities can be highly nonlinear. 5 linearization iterations were performed and were terminated early if there was no substantial increment in the flow velocity. At the end of the linearization iterations, the updated flow increment duv was obtained, and the image velocity, uv, for a single image pyramid level was updated via Eq. (6.19). With the image velocity, uv, bi-cubic interpolation was used to warp the second image towards the first image. 5 warping iterations were used for a single image pyramid level. Image derivatives were recomputed after every image warping iteration.

For the coarse-to-fine multi-resolution scheme, as the iteration progressed from the coarsest to the finest resolution, the image velocities were up-sampled using bilinear interpolation, and used as initial velocity estimates to perform image warping for the first warping iteration. In addition, the GNC technique was also implemented to better handle the non-convex penalty function and nonlinear data term. 3 GNC iterations were used. In the first iteration, the penalty function was fully quadratic, and the three sets of weights z_D, z_ξ and z_ζ were not computed at the IRLS level since it is equal to unity based on Eq. (6.14). In the second iteration, the robust penalty function (see Eq. (6.10)) and quadratic function were linearly combined in equal weightage. The last iteration consisted of the fully robust penalty function.

6.3.3 Validation of optical flow algorithm

Schlieren image velocimetry (SIV) is a relatively new concept that is not as well established as techniques such as PIV. As such, the optical flow algorithm can be difficult to validate or benchmark in SIV applications. One of the main problems is

that existing methods such as the cross-correlation window matching algorithms adopted in PIV tend to fare poorly in SIV applications and is hardly a worthy competitor for optical flow. This is further aggravated by the lack of high-fidelity numerical results or ground truths that are publicly available for SIV applications. The current situation is in stark contrast to the computer vision community where ground truths and training datasets are readily available on the optical flow Middlebury Flow site [77]. In view of the current state of development of SIV and the necessity to perform some form of validation on the in-house optical flow algorithm, the following validation test was designed and performed.

6.3.3.1 Synthetic schlieren images with ground truth

A schlieren image pair with ground truth is necessary for optical flow algorithm validation. In order to generate the ground truth data, procedures similar to Section 6.2.2 were adopted. A pair of schlieren images obtained from ultrahigh-speed schlieren experiments are presented in Figure 6.8(a) and Figure 6.8(b), where the image sampling frequency was 166 kHz and image exposure time was 0.77 μs. These images were processed using the in-house optical flow code and the resulting velocity field was then treated as the ground truth. The ground truth was used to perform image warping on the first schlieren image (see Figure 6.8(a)) with bi-cubic interpolation, leading to a synthetically generated schlieren image as shown in Figure 6.8(c). Optical flow was then performed on the new image pair (Figure 6.8(a) and (c)) and compared against the ground truth. In addition, the open source optical flow code [89] which implemented the original Horn and Schunck's model was performed on the new image pair as well for benchmarking purposes. Note that the open source

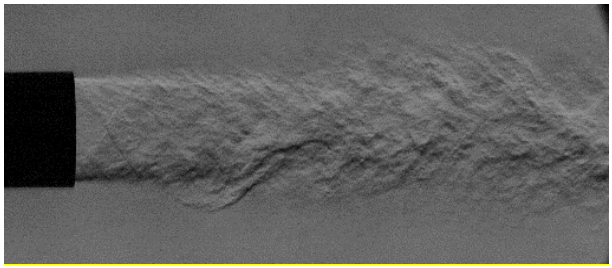

(a)

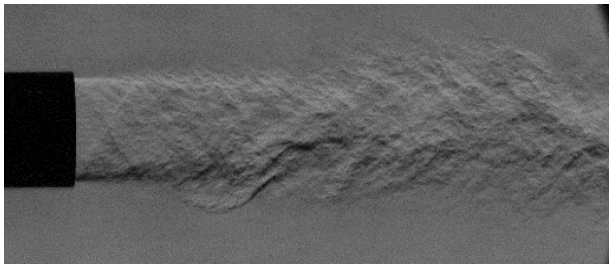

(b)

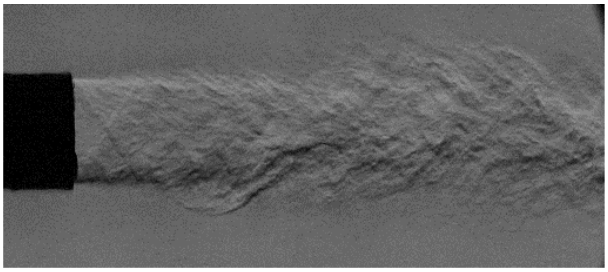

(c)

Figure 6.8: (a) Schlieren image #1, (b) schlieren image #2 and (c) synthetic schlieren image #2

code is a fairly competitive optical flow code in computer vision applications and was ranked at the top of the Middlebury benchmark in year 2010.

From the results shown in Table 6.5, the in-house optical flow algorithm appears to perform better than the open source code. This can be attributed to the difference in the optical flow model for the in-house and open source code. The open source code's model follows the original Horn and Schunck's model closely, which was originally developed for rigid body motions and had been shown to penalize vorticity and

Table 6.5: Performance of the in-house optical flow algorithm

Image description	Code	AEPE
Synthetic schlieren image with ground truth	In-house	0.701
	Open source	0.725

divergence estimates. In contrast, the in-house optical flow model uses a different regularization term that does not penalize vorticity and divergence estimate and is therefore more suitable for fluid flow applications. When comparing the error estimates of the in-house optical flow algorithm with those presented in Table 6.3, the errors appear to lie between the results of uv*3 and uv*4, indicating that a higher camera framing rate is desirable for better results.

6.4 Application in over-expanded baseline and bevelled jets

6.4.1 Experimental setup

In this study, the experiments were performed using the supersonic jet apparatus presented in Section 3.1. The circular baseline and 30˚ bevelled nozzles were investigated using SIVOF at over-expanded flow conditions with an NPR of 2.8 and jet Mach number of M_j=1.31. The over-expanded flow condition was selected due to hardware limitations of the PIV equipment, which will be explained in greater detail later. The horizontal knife-edge was used at the sagittal focus since the shear layer is of interest. Time-resolved schlieren images were captured with an ultrahigh-speed Photron SAX2 camera. The image sampling frequency was f_s=160 kHz and an exposure time of 2.5 μs was used. The in-house optical flow code was then used

to process the schlieren images to obtain the velocity fields at a vector resolution of one velocity vector per pixel. It is noted that the optimal image sampling frequency has been determined to be much higher (at approximately 400 kHz) based on the study presented in Section 6.2. This was, however, not achievable due to practical hardware limitations.

To compare the results of SIVOF, 2D PIV measurements were conducted based on the same jet apparatus and flow conditions. PIV seeding was achieved with a Laskin nozzle oil droplet generator operated at its maximum safe operating pressure of 5.5 bars. This limited the maximum jet NPR that can be investigated in the current study to NPR=2.8. Standard cooking olive oil was used to produce the seeding particles. The nominal mean diameter of these seeds was 0.9 μm. Laser beams from a 15 Hz, 200 mJ/pulse, double-pulsed Litron Nd:YAG laser and sheet-forming optics were used to provide 2D sheet illuminations, and two Dantec Dynamics FlowSense EO 2M cameras with Nikon AF Micro-Nikkor 200 mm f/4D IF-ED Lens were placed side-by-side to increase the field-of-view during image-capturing. The resulting particle image-pairs were subsequently stitched together to provide 3200px × 1200px particle images for post-processing. Multi-grid cross-correlations with a deforming interrogation window were used, with an initial and final window size of 256px × 256px and 64px × 64px. Peak and range validations were used and rejected vectors were substituted with a 3point × 3point neighbourhood averaging scheme.

6.4.2 Results and discussion

Instantaneous velocity vectors and vorticity contours of the baseline and bevelled nozzles as determined by the present SIVOF technique are shown in Figure 6.9. Note

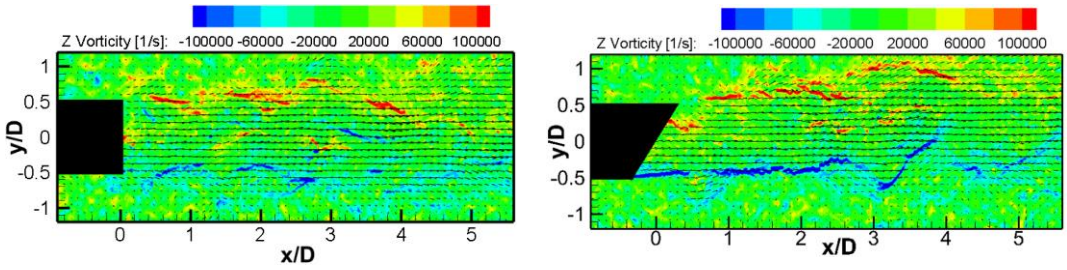

Figure 6.9: SIVOF's velocity vectors and vorticity contours of M_d=1.45 and NPR=2.8 jets for the (a) baseline and (b) 30˚ bevelled nozzles.

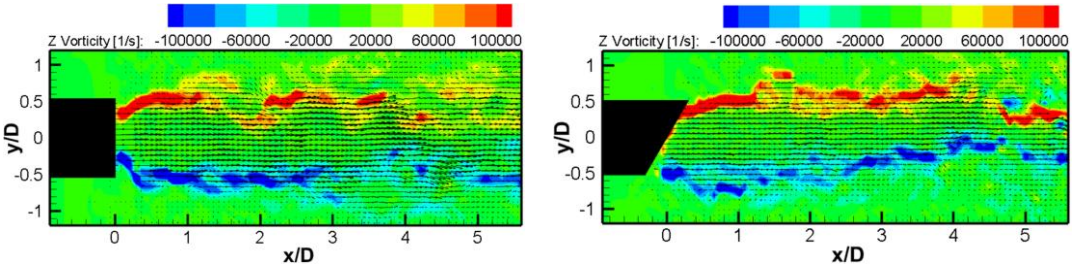

Figure 6.10: PIV's velocity vectors and vorticity contours of M_d=1.45 and NPR=2.8 jets for the (a) baseline and (b) 30˚ bevelled nozzles.

that only every fifth vector was shown to avoid data-cluttering. Instantaneous velocity vectors and vorticity contours for the same nozzle as determined through PIV technique are presented in Figure 6.10. It should also be clear that the flow fields captured in both Figure 6.9 and Figure 6.10 are not from the same time instance. The vorticity estimates were computed using the central finite difference scheme with second order accuracy and implemented via a convolution matrix (i.e. kernel).

For all schlieren image-pairs processed, SIVOF technique was able to consistently produce sharper and clearer vortical structures, thus allowing reasonably accurate tracking of individual vortical structures across multiple time frames. In particular,

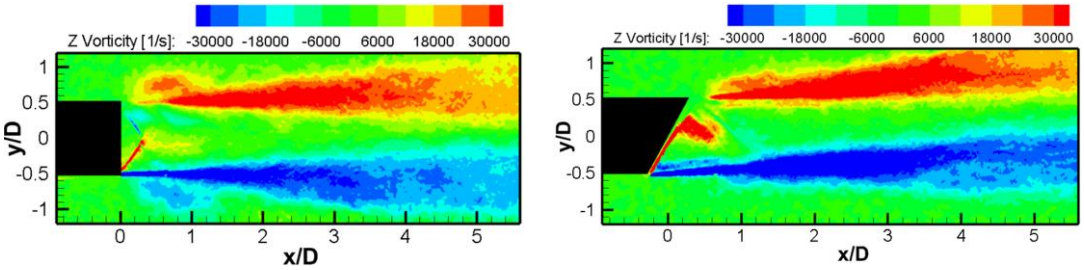

(a) (b)

Figure 6.11: SIVOF's time-averaged vorticity contours of M_d=1.45 and NPR=2.8 jets for the (a) baseline and (b) 30˚ bevelled nozzles.

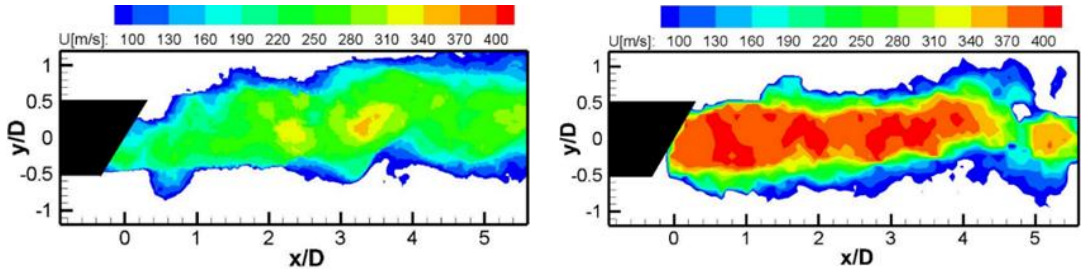

(a) (b)

Figure 6.12: Velocity contours of M_d=1.45 and NPR=2.8 jets for the 30˚ bevelled nozzle, obtained from (a) SIVOF and (b) PIV techniques.

coupled with velocity information, time-resolved convective velocities of these tracked vortical structures may be recovered. In contrast, it was not possible to accurately identify and track structures across multiple time frames for PIV, due to the lower spatial and temporal resolution of the extracted velocity fields. In Figure 6.9(b), between x/D=3 to 4 locations, a vortical structure may be clearly discerned. The time-resolved results reveal convection of such structures with correspondingly decreasing vorticity magnitudes. These structures appear to be inert and preserve their outlines even when it is subjected to strong flow shears. The inert behaviour of eddies generally agrees well with past studies where the behaviour of large eddies in compressible shear layers was studied [17, 33]. After several frames, the structures

appear to decay rapidly, and tracking was no longer possible. Such an observation may be attributed to different vorticity dissipation rates for different parts of the flow structures. This assertion is supported in Figure 6.11(b), which illustrates vorticity dissipation in the streamwise direction and different levels of vorticity magnitude in the traverse direction. For the case of the baseline nozzle in Figure 6.9(a), it appears to be more difficult to track these structures across time frames, possibly due to more rapid and different dissipation rate of vorticity in a structure.

The vorticity along the shear layers appears to be much stronger in the PIV plots as shown in Figure 6.10 than the SIVOF plots as shown in Figure 6.9. The magnitude of the vorticity is related to the strength of the roll-ups, and PIV will always capture stronger roll-ups as compared to schlieren-based techniques. This difference can be attributed to the differences between a schlieren image and a particle image. The post-processing method, be it cross-correlation or optical flow, is not the reason behind the observed differences. In particle-images captured in PIV experiments, assuming the seeding particles track the air flow faithfully, the velocities obtained will represent the true velocity of the fluid flow. For example, if a vortex is present in the shear layer, seeding particles will track the roll-up motion as well as the convection of the vortex structure. Hence, the velocity obtained will represent the roll-up velocity and its convective velocity. It may be difficult to separate these two components from each other.

In contrast, for the exact same flow scenario, schlieren images can capture the vortex convective motion very accurately. However, it is not able to image the roll-up motion easily due to a lack of density variations. As such, the extracted velocity is

representative of the *convective velocity* of the structure. This is the reason schlieren images have been and can be used to extract convective velocities directly in high-speed free shear layer experiments [49]. This is also the reason why eddies are reported to be relatively inert even though they are subjected to significant shear, and in Papamoschou & Bunyajitradulya exact words, "*it helps to think of the structure as a wave front in this respect"* [33]. This very issue has also been reported in more recent literature [135].

In addition, significant velocity and vorticity can also be observed just beside the nozzle at x/D<0 in Figure 6.9. This does not appear to be realistic. For the same region, the PIV results shown in Figure 6.10 have close to zero velocity and vorticity. The observations in Figure 6.9 is likely caused by density variations in the environment that was captured in the schlieren images. In general, schlieren image noise has been observed to be higher than particle-images obtained from PIV, and this is one of the limitations of SIVOF.

Time-averaged vorticity contours from 200 datasets produced by the SIVOF technique are shown in Figure 6.11. The growth rate of the shear layer for the circular and 30˚ bevelled nozzle appears to be linear, and slight jet vectoring may also be observed in the 30˚ bevelled nozzle. For the circular nozzle between x/D=0 to 1 location, there are two discernible non-zero vorticity regions adjacent to the shear layers close to the nozzle exit. However, note that the averaged vorticity magnitude for these ejections was low, and instantaneous vorticity contours in Figure 6.9(a) suggested no such behaviour. Hence, either this is an artefact of the optical flow technique, or it is associated with an unsteady near-field flow process that only optical

flow technique has the necessary resolution to resolve it. Intriguingly, shock structures in the immediate vicinity of the nozzle exits appeared to be captured in both nozzles through the technique and manifest themselves in the form of distinct sharp lines of strong localized vorticities. Their locations were also noted to be consistent with the shock waves observed in the schlieren images. From Figure 6.11(a), downstream of the Mach disk connecting the oblique shocks, a localized region of vorticity may be observed. This is likely to be a slipstream, which is an embedded shear layer that is subsonic from the flow downstream of the Mach disk. Further downstream, the shear layers from opposite sides of the potential core start to approach each other, leading to a reduced potential core region. Extrapolation of the potential core boundary estimates the potential core length at approximately x/D=9 for both baseline and bevelled nozzles. This is consistent with results observed in an earlier study based on the same nozzle design and NPR value [27].

SIVOF and PIV instantaneous velocity contours are shown in Figure 6.12. Interestingly, SIVOF technique was found to arrive at lower centreline velocities as compared to PIV technique. However, this is not too surprising as PIV images were taken with a nominally 2D thin laser sheets aligned along the jet axis. In contrast, schlieren images integrate all density gradient information along the light path. Hence, centreline velocity information recovered by SIVOF technique does not actually reveal flow behaviour in the potential core. Rather, it reveals information regarding the jet potential core and two sides of the shear layer. Because of this reason, SIVOF technique appears to be more useful in regions closer to the edge of the shear layer where the integrative nature of schlieren is minimized. Going by this

line of thought, density fields that have been perturbed by the presence of acoustic waves and jet-induced convection currents may be one of the reasons contributing to the presence of spurious velocity vectors found in the SIVOF results.

From the above results and discussions, it should be clear that the velocities obtained from the SIVOF technique (or schlieren-based velocimetry in general) is representative of the convective velocities of the structures and not the true velocity of the flow. However, it should also be mentioned that most of the empirical observations and flow and noise models of supersonic jets were developed based on schlieren images and its velocimetry. For example, the convective velocity from schlieren images have been used to characterize the compressibility effect of supersonic shear layers [49], in jet screech frequency prediction models [21], and for developing Mach wave elimination strategies [35]. As such, despite the limitations of SIVOF, it is still an invaluable toolkit in high-speed flow diagnostics.

6.5 Summary

Time-resolved SIVOF technique was proposed as a viable velocimetry technique in the study of supersonic jet shear layers. A systematic study on the optimization of schlieren images was performed and the results indicated high framing rate requirements of approximately f_s=400 kHz for optimal optical flow performance. As a result, the modified Z-type double-camera schlieren setup was proposed as an alternative experimental setup that is cost effective and can achieve the required framing rate. This involved capturing schlieren image pairs with two cameras that can be independently triggered with a short time delay. The schlieren image pair that

were obtained were successful in capturing the same turbulent structures that were spatially shifted. Nonetheless, slight differences in terms of image intensity in the image pair due to factory miscalibration of the cameras meant that the images were not useful for optical flow analysis in the current study.

An in-house variational optical flow technique was developed for extraction of the velocity field. Key features of the in-house algorithm were presented in terms of the optical flow model and the method used to minimize the objective function. The algorithm replaced the standard Horn and Schunck [78] regularization term with a second order div-curl regularizer, introduced robust penalty functions and made use of modern methods to minimize the objective function. Validation was performed by using synthetically generated schlieren images with ground truth and benchmarked against an open source optical flow algorithm which ranked at the top of the Middlebury benchmark in year 2010. The results indicate improved performance of the in-house algorithm as compared to the open source algorithm.

Time-resolved schlieren images of over-expanded baseline and bevelled jets were captured at f_s=160 kHz using the modified Z-type single-camera schlieren setup and the ultrahigh-speed Photron SAX2 camera. The results show that SIVOF offers much higher spatial resolution of the velocity fields as compared to PIV, resulting in sharper and clearer vortical structures that may be tracked across multiple time frames. The inert behaviour of time-resolved eddies found in the supersonic jet shear layer, shear layer growth rate, shock structure patterns and potential core length indicate good agreements with earlier studies. Key differences between SIVOF and PIV results, particularly in the jet centreline region, can be attributed to the 2D laser sheet

employed in PIV technique which differs significantly from the integrative nature of schlieren imaging. Finally, it is noted that the schlieren images were not optimized for optical flow analysis. A higher image acquisition frequency would have been much more desirable and is expected to lead to even more accurate SIVOF results.

Chapter 7 Jet Screech Characterization using Time-resolved Schlieren-based Proper Orthogonal Decomposition

7.1 Overview

Of the three jet noise components, the jet screech is a discrete tone that can lead to sonic fatigue failure of the airframe if the nozzle is poorly designed. As such, there had been several studies dedicated to understanding jet screech and developing methods to mitigate it. There are four key processes involved in jet screech production (receptivity, growth and propagation of vortices, shock-vortex interaction, feedback). In particular, the shock-vortex interaction is responsible in producing the acoustic waves and had been described using a geometrical theory that is analogous to geometrical acoustics (see Figure 7.1) [136]. The study showed large-scale vortices interacting with shock fronts which resulted in shock leakages at the saddle points of the vortices. This indicates the tendency of jet screech to be produced in an unsteady manner along the shear layer near where the incident wave reflects. The results of the study agreed well with the jet screech frequency prediction model of Powell [21], which linked the convective velocity of the structures to the screech frequency. The unsteady nature of jet screech had also been observed based on a waterfall plot of instantaneous SPL spectra contrasted with time-averaged SPL spectra [137], and excessive expansion of the barrel shocks at high jet Mach numbers was observed to lead to aerodynamic blocking of feedback, resulting in cessation of jet screech. Studies on jet screech have also revealed that the feedback and receptivity

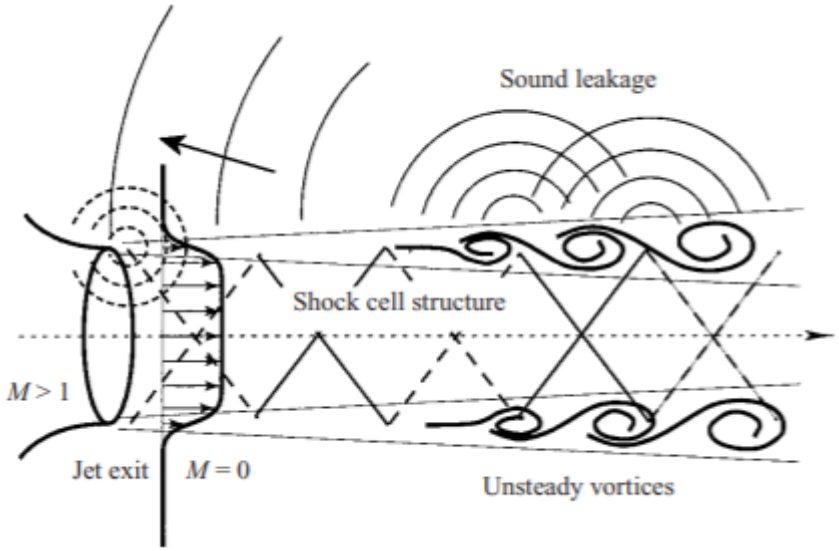

Figure 7.1: Diagram of jet screech generation and the leakage process [136]

processes depended strongly on the nozzle exit geometry, with screech intensity observed to increase drastically simply by using thicker lips at the nozzle exit [138].

In terms of flow and noise control, modification of the nozzle exit geometry has been a popular choice due to its passive capabilities, ease of implementation and effectiveness in influencing key processes of jet screech production. These modifications were first termed as indeterminate-origin (IO) nozzles [39], and past studies have shown that circular [39, 40] and rectangular [45, 139] IO nozzles can significantly alter the shock structures, shear layer and jet screech characteristics in imperfectly expanded jets. Multiple screech tones existing simultaneously had also been observed [45], and this phenomenon was modelled using a waveguide shock cell theory [139] which allows for multiple feedback loops and screech tones to coexist simultaneously in moderately imperfectly expanded jets, resulting in predicted screech frequencies that were in good agreement with experimental measurements. Other jet noise reduction studies performed on IO jets include the use

of bevelled [140, 141] and chevron jet nozzles [142], with results indicating significant changes in the noise characteristics and that the noise reduction is also strongly dependent on the directivity and frequency range.

For many jet screech studies, schlieren experiments are very popular as it is non-intrusive, easy to implement and offers high quality insights into the pertinent flow features. Schlieren images can offer important parameters such as the shock cell length and convective velocity estimates (with schlieren image velocimetry) which are required to predict the screech frequency based on the jet screech frequency prediction model of Powell [21]. Recent studies have seen efforts to post-process schlieren images in order to extract more information from them. In particular, modal decomposition techniques are of interest as they have been applied to time-resolved schlieren images of supersonic jets, and the spectral analysis of the mode coefficients have led to accurate jet screech frequency. For example, in the study of a supersonic single expansion ramp nozzle [143], POD and Dynamic Mode Decomposition (DMD) analyses were performed on time-resolved shadowgraphs, and the extracted frequencies agreed remarkably well with those obtained using traditional microphone measurements made in the same study. Other studies that have applied POD upon time-resolved schlieren images of supersonic jets had also been reported in recent literature [108, 144, 145]. These studies share similar methodology in that the frequencies that were extracted were based on spectral analysis of the POD mode coefficients. Although the POD modes were able to capture acoustic waves, the jet screech was not the focus of these studies. In addition, the methods adopted by these studies are not capable of revealing the transient nature of jet screech, and the POD

computations is not scalable when handling huge image datasets that is available to most ultrahigh-speed schlieren setups. Finally, it should be mentioned that POD has also been applied to schlieren images for other purposes such as obtaining the convective velocities [146], but this is not within the scope of the current study.

While there have been many examples of POD applications in fluid mechanics studies, such as those associated with the vortex-shedding frequency of flow past a shallow cylinder [109], shear layer generated by a groyne in shallow flow [109] and in turbulent jets [101, 102, 147], applications of POD upon time-resolved schlieren images have only been reported in recent literature [108, 143-145]. To the best of the author's knowledge, schlieren-based POD methods for jet screech studies of circular bevelled nozzles remain relatively scarce. Hence, this study aims to further develop and illustrate the application of short-time POD analysis with time-resolved schlieren images, for the purpose of characterizing the jet screech frequency (or the absence of) and its transient behaviour. The significance of the key parameters extracted from the proposed technique will be discussed, and results of supersonic jets emanating from a circular baseline and two bevelled nozzles with differing acoustic characteristics are compared and analysed in detail here. The contribution of the proposed technique includes extending the amount of information available from an existing schlieren setup/dataset, replacing the need for microphone measurements when only the screech frequency and transient behaviour is desired, and gains in computational efficiency over standard POD analysis when handling huge image datasets. The continual improvements in computational efficiency is

necessary in order to keep up with the capabilities of state-of-the-art camera hardware which is now capable of generating data at several Gigabytes per second.

7.2 Experimental setup and post-processing procedures

7.2.1 Supersonic jet facility and nozzle designs

The schlieren experiments were performed using the supersonic jet apparatus presented in Section 3.1. Three circular nozzles with different nozzle exit geometries were used in this study: baseline, 30° bevelled and 60° bevelled nozzles. The coordinate system, azimuthal angles, θ, and polar angles, ϕ, are defined on schematics of the nozzles in Figure 7.2. All test cases in the current study involved moderately under-expanded jets freely exhausting at NPR=5.

7.2.2 Time-resolved schlieren imaging and POD

High speed schlieren imaging was performed using a Phantom v2512 ultrahigh-speed camera in the modified Z-type schlieren setup presented in Section 3.2. The focus was on capturing the supersonic jet turbulent structures, hence a horizontal knife-edge relative to the jet flows was used along with a 0.77 μs image exposure time. Images were captured at f_s=166,200 FPS, which was deemed to be sufficient based on the Nyquist rate of the noise emission frequencies obtained from the acoustics measurements. The full image sequence for a single nozzle test case consisted of 80,000 time-resolved images.

POD for fluid mechanics applications and its implementation procedures has been discussed in Section 2.3, hence only a brief overview relevant to the current study will be provided here. The implementation of POD in this study was based on the

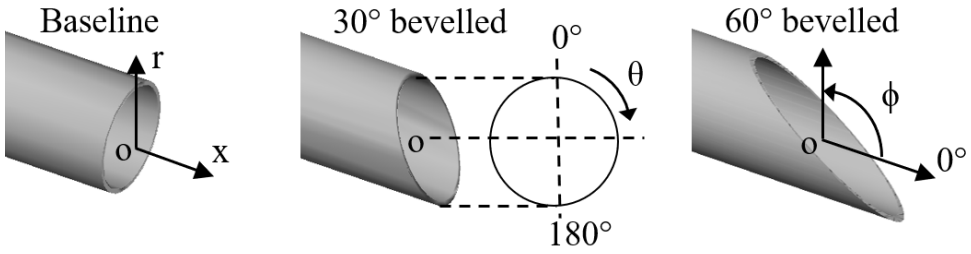

Figure 7.2: Schematics of the test nozzles and definition of the coordinate systems

SVD approach and performed on MATLAB. For an image-series with *n* number of images, with each image comprising of *q* number of image pixels, the image matrix can be formulated as:

$$\boldsymbol{X}(j,t) = \begin{bmatrix} u_1^1 & \dots & u_1^n \\ \vdots & \ddots & \vdots \\ u_q^1 & \dots & u_q^n \end{bmatrix}, \tag{7.1}$$

where j denotes the pixel index and t denotes time. The fluctuating image matrix can then be obtained by:

$$\widetilde{\boldsymbol{X}} = \boldsymbol{X} - \overline{\boldsymbol{X}} \tag{7.2}$$

where the overbar denotes time-averaging. The economy-size SVD of the fluctuating image matrix is then obtained by

$$\widetilde{\boldsymbol{X}} = \boldsymbol{U\Sigma V}^*, \tag{7.3}$$

where $\boldsymbol{U}$ represents the POD modes, $\boldsymbol{\Sigma}$ is the diagonal matrix containing information on the eigenvalues, and $\boldsymbol{V}$ contains the temporal information for the corresponding POD modes.

The frequency information of a particular POD mode was then obtained by performing Welch's power spectral density (PSD) estimate on a selected column vector of $\boldsymbol{V}$ (i.e. a selected POD mode). The lowest order mode is selected as it typically represents the strongest contribution to the overall flow field. For Welch's PSD procedure, the image-series was divided into equal-length segments with a segment length of 90% of the image-series length (rounded to nearest whole number). From segment to segment, an overlap of 80% of the image-series length (rounded to nearest whole number) was used. Each segment was windowed with a Hamming window function and the modified periodograms were averaged to obtain the PSD estimates. The number of discrete Fourier transform (DFT) points used in the PSD estimate was 2^{17}. From the PSD estimate, the frequency corresponding to the peak amplitude was extracted and non-dimensionalized to the Strouhal number based on the definition:

$$St = \frac{f}{f_c} = \frac{f D_j}{u_j} \tag{7.4}$$

where f_c is the jet plume characteristic frequency, $D_j = 1.09D$ is the jet column average diameter calculated based on Tam's definition [148], and $u_j = 471m/s$ is the jet velocity. The Strouhal number is then rounded to 2 decimal points with an uncertainty of ±170Hz.

7.3 Results and discussions

7.3.1 POD of time-resolved schlieren

Based on the jet noise literature, a preliminary assessment of using schlieren-based POD technique for jet noise identification is performed. Firstly, turbulent mixing noise occurs at a wide range of frequencies across all polar angles. Since the schlieren-based POD technique is based on extracting distinct frequencies which have the greatest PSD amplitudes, it is ill-suited for identification of turbulent mixing noise. Secondly, BSAN exists as a broadband hump with a distinct peak. It is possible for the schlieren-based POD method to identify the frequency occurring at the peak of the broadband hump. However, this frequency changes with the polar angle, and the POD modes cannot be decomposed further in terms of wave directivity. Hence, it is believed that the schlieren-based POD method is also ill-suited for BSAN identification. Realistically speaking, the screech tone is the only jet noise component that can be identified with its frequency characterized using the proposed schlieren-based POD technique, since it has a very distinct narrow peak that remains at the same frequency across all polar angles.

Samples of time-resolved schlieren images for the three different nozzles that were subsequently processed by POD are presented in Figure 7.3. Note that the bevelled nozzles shown in Figure 7.3(b) and Figure 7.3(c) were located slightly lower in the images than their baseline counterpart to capture the upward tilt (i.e. vectoring) of the jets. Additionally, it should be noted that the focus was on the turbulent structures and shock cells located within approximately the first 5D from the jet origin of the three test nozzles. This streamwise range is where large instability waves of the jet

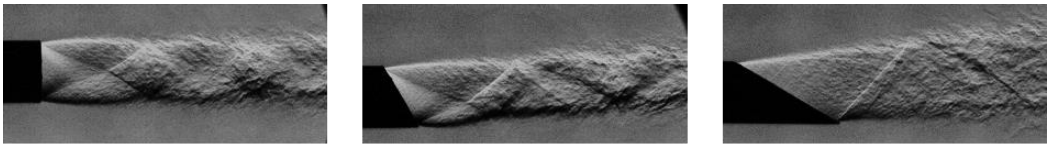

(a) (b) (c)

Figure 7.3: Schlieren image samples taken for the (a) baseline, (b) 30° bevelled and (c) 60° bevelled nozzles used for POD post-processing.

exist, which has been suggested to have the strongest influence on the mode shape and tone intensity of jet screech [4]. Acoustic waves were not captured by limiting the image field-of-view selectively and making appropriate adjustments to the schlieren system. This was essential in the current study. By performing POD on schlieren images containing only the turbulent structures within the first 5D from the nozzle origins, the frequency corresponding to the peak amplitude of the resulting PSD for each nozzle can then be directly attributed to these structures. If this frequency agrees well with the microphone measurements performed on the same jet, a link between the jet turbulent structures and acoustic characteristics can then be established. Other than characterizing the nature and frequency of jet screech through this approach, application of schlieren-based POD in this manner has the additional advantage of complementing traditional acoustic measurements to gather more insights into the jet screech phenomenon.

At this stage, it is necessary to provide a brief summary of the acoustic measurements performed on the same jet nozzles, but by a different researcher in the same research group. Readers are advised to refer to an earlier study for further details on the acoustic setup and post-processing procedures [149]. The near-field noise spectra and wavelet transform analyses of the acoustic signal indicate an intermittent jet

screech with SPL of 165 dB occurring at St=0.25 for the baseline nozzle, an intermittent jet screech with SPL of 152 dB occurring at St=0.25 for the 30° bevelled nozzle and no jet screech for the 60° bevelled nozzle.

7.3.1.1 Spectral analysis of POD coefficients

Based on the acoustic measurements, the baseline and 30° bevelled jets have been revealed to display intermittent jet screech, while none was observed for the 60° bevelled jet. Before POD can be performed on an image-series, a suitable image-series length (i.e. sample size) and subsampling frequency must be determined. While the selection of these parameters is usually straightforward, intermittent jet screech behaviour such as the ones observed here may complicate the procedures, especially if no prior acoustic information on the jet screech is available. This can in fact be demonstrated by a systematic study performed on the baseline nozzle, where both the subsampling frequency and sample size are varied to understand their impact on the PSD results of the intermittent jet screech problem at hand.

Data subsampling was performed by keeping every P^{th} image from the full image sequence comprising of 80,000 images, which in turn leads to a subsampled frequency of f_s/P. The data was subsampled at P=1, 2, 4 and 8 to obtain frequencies of f_s, $f_s/2$, $f_s/4$ and $f_s/8$ for a sample size of n=8000, and POD was performed on all four datasets following the same implementation procedures. Note that the lowest subsampling frequency of $f_s/8$ translates to a Nyquist frequency of $f_s/16$ (i.e. St=0.3), which is still higher than the jet screech tone detected at St=0.25 from the acoustic measurements. The temporal coefficients of the first POD mode (first column of $\boldsymbol{V}$) were used for frequency extraction as they represent the strongest contribution

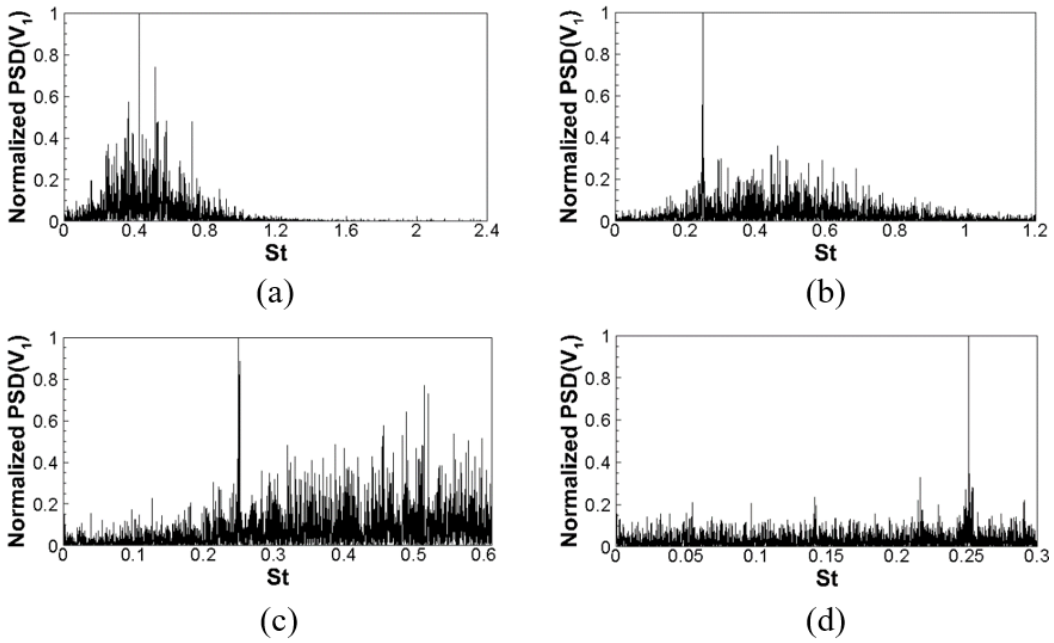

Figure 7.4: Normalized PSDs of the first POD mode temporal coefficients using the baseline nozzle data subsampled at (a) f_s, (b) $f_s/2$, (c) $f_s/4$ and (d) $f_s/8$ for a sample size of n=8000.

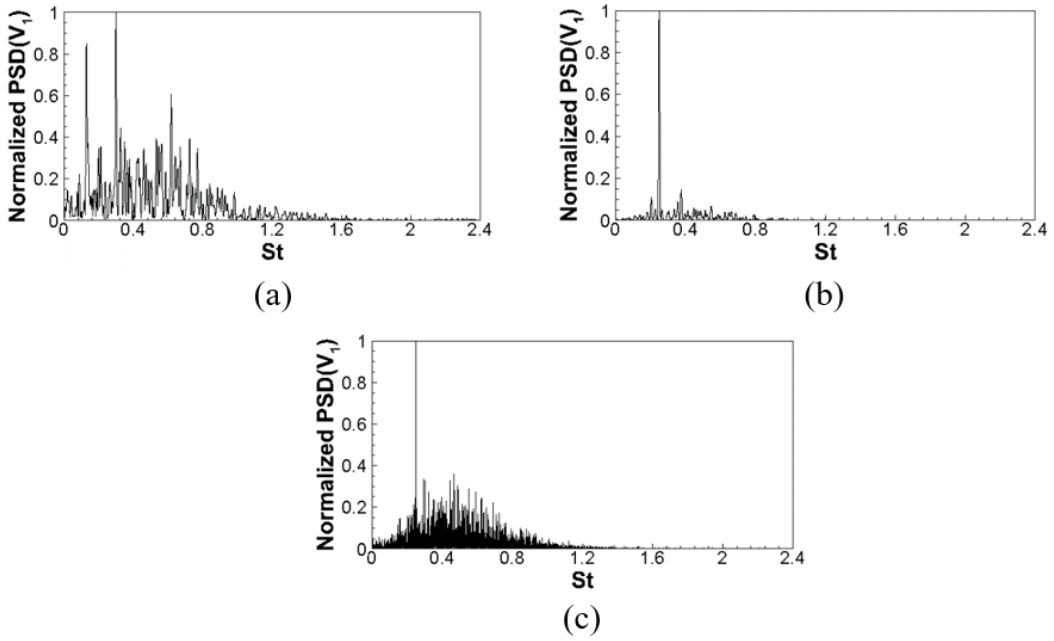

Figure 7.5: Normalized PSDs of first POD mode temporal coefficients based on the baseline nozzle data subsampled at f_s for images (a) #1-1000, (b) #9001-#10,000 (c) and #1-16,000.

towards the schlieren images. The associated PSDs normalized by its maximum value for the baseline nozzle are presented in Figure 7.4.

Based on the PSD results shown in Figure 7.4(b) to Figure 7.4(d), the most dominant peak occurs at St=0.25 when the subsampling frequencies are at $f_s/2$ and below. These results not only agree remarkably well with each other but more importantly, with the screech tone obtained from the acoustic measurements, indicating the existence of a correlation between the jet screech tone and POD filtered turbulent structures. In contrast, the PSD for sampling frequency f_s as shown in Figure 7.4(a) displays a peak at St=0.42, which clearly deviates from the results of subsampled frequencies at $f_s/2$ and below, as well as the acoustically-measured screech tone.

It seems counter-intuitive that using the highest sampling frequency of f_s with a sample size of n=8000 results in a peak Strouhal number (i.e. Strouhal number corresponding to the peak amplitude of the PSD) which differs significantly from the acoustically-measured jet screech, when this is otherwise clearly observed in the PSD of the data subsampled at lower frequencies. Note that f_s is almost 20 times higher than that of the screech frequency and most certainly fulfils the Nyquist criterion. To investigate further, POD was performed on smaller and larger sample sizes of n=1000 and 16,000 respectively at the same sampling frequency of f_s. The results shown in Figure 7.5(a) and Figure 7.5(b) correspond to the normalized PSDs obtained for a sample size of n=1000, for images #1-1000 and #9001-10,000 respectively. Intriguingly, the peak Strouhal number corresponds to the jet screech frequency in Figure 7.5(b) but not in Figure 7.5(a), indicating that the choice of image samples also play an important role in determining the peak Strouhal number.

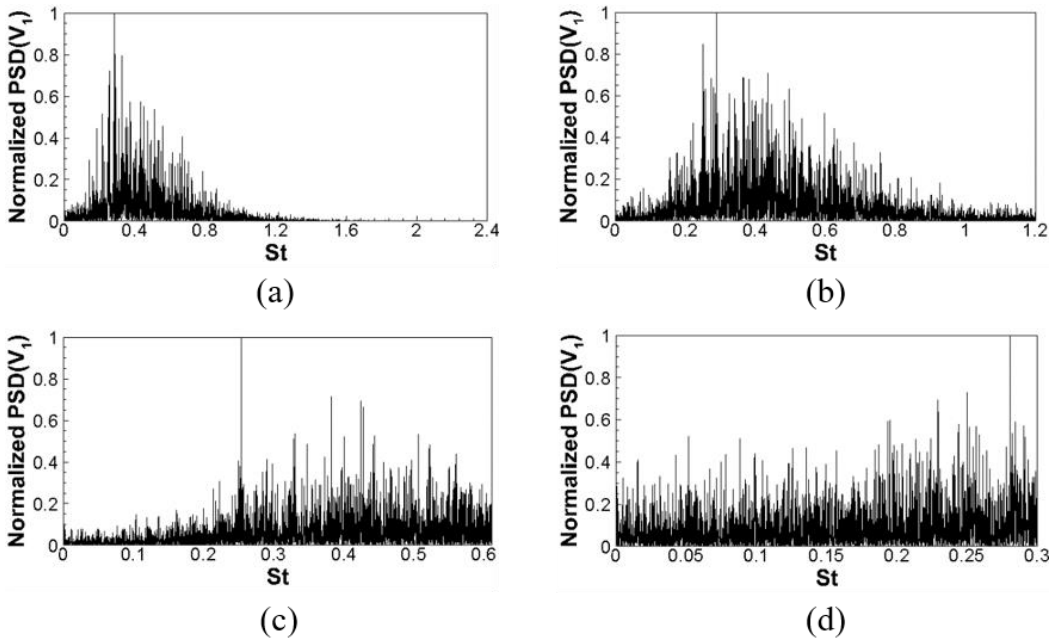

Figure 7.6: Normalized PSDs of the first POD mode temporal coefficients based on the 30° bevelled nozzle data subsampled at (a) f_s, (b) $f_s/2$, (c) $f_s/4$ and (d) $f_s/8$ for a sample size of n=8000.

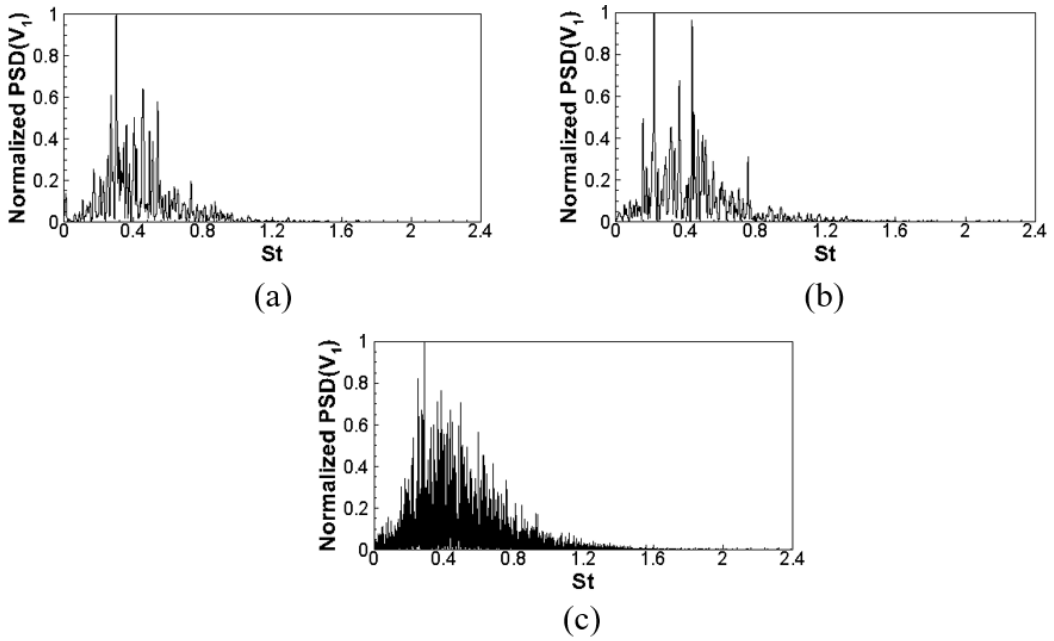

Figure 7.7: Normalized PSDs of the first POD mode temporal coefficients based on the 30° bevelled nozzle data subsampled at f_s for images (a) #1-1000, (b) #9001-#10,000 (c) and #1-16,000.

Table 7.1: Summary of tests conducted on the baseline jet based on varying the subsampling frequency and sample size. (✓) indicates peak St corresponding to jet screech, (✗) indicates otherwise.

Fig.	**Sample size**	**Subsampling frequency Index of the range of sampled images (#)**			
		f_s	$f_s/2$	$f_s/4$	$f_s/8$
8	n=8000	#1-8000 (✗)	#1-16,000 (✓)	#1-32,000 (✓)	#1-64,000 (✓)
9	n=1000	#1-1000 (✗)	N.A.		
	n=1000	#9001-10,000 (✓)			
	n=16000	#1-16,000 (✓)			

Figure 7.5(c) shows the PSD for a sample size of n=16,000, for images #1-16,000, and the peak Strouhal number is again observed to correspond to the jet screech frequency. These observations show that the turbulent structures lead to a peak Strouhal number which agrees well with the jet screech frequency but only intermittently, thereby reinforcing the notion that the jet screech is intermittent indeed. Table 7.1 summarizes the tests based on varying the subsampling frequency and sample size, with the index of the range of sampled images provided for further details. A "tick" indicates the PSD displayed a peak Strouhal number corresponding to the jet screech and a "cross" indicates otherwise.

The same tests as described for the baseline nozzle earlier were performed on the 30° bevelled jet, where an intermittent screech tone with lower SPL occurring at St=0.25 was acoustically measured. The PSD results based on varying the subsampling frequency with a sample size of n=8000 are presented in Figure 7.6, while those based on varying the sample size with a subsampling frequency of f_s are shown in

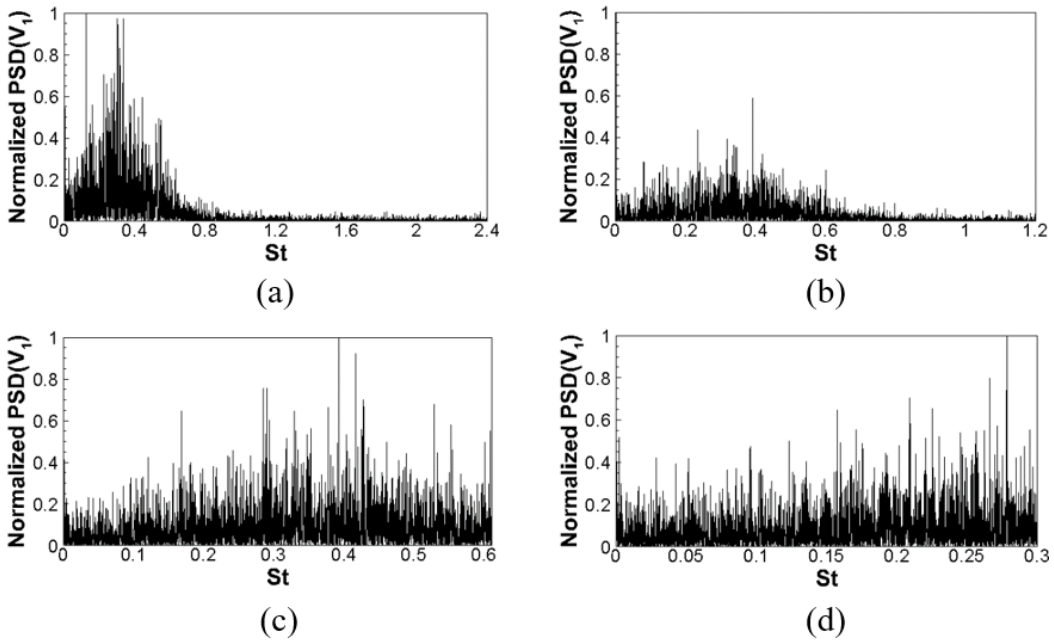

Figure 7.8: Normalized PSDs of the first POD mode temporal coefficients based on the 60° bevelled nozzle data subsampled at (a) f_s, (b) $f_s/2$, (c) $f_s/4$ and (d) $f_s/8$ for a sample size of n=8000.

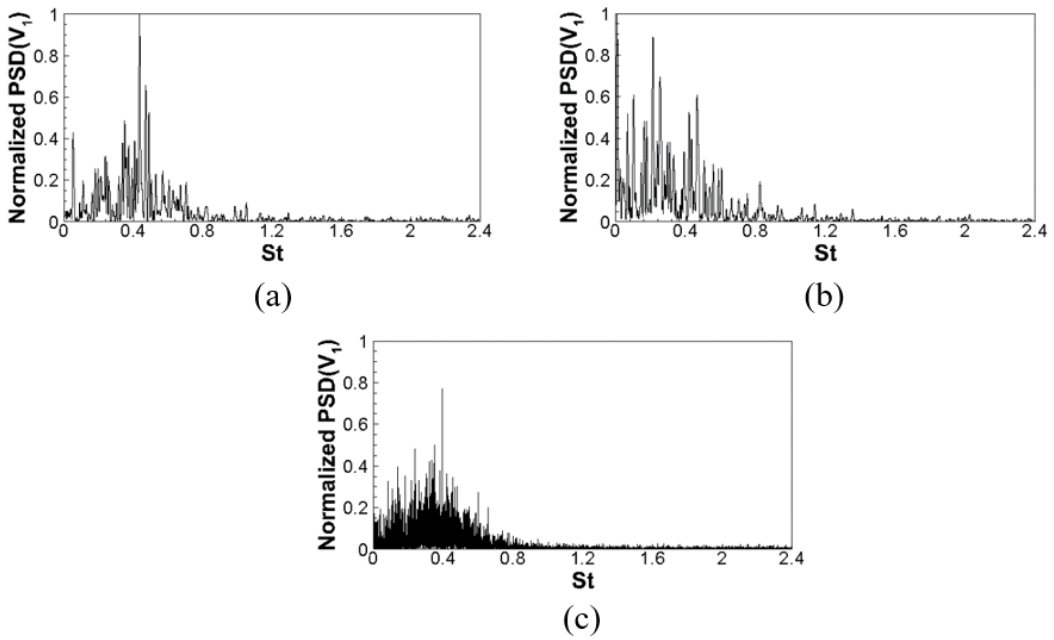

Figure 7.9: Normalized PSDs of first POD mode temporal coefficients based on the 60° bevelled nozzle data subsampled at f_s for images (a) #1-1000, (b) #9001-#10,000 (c) and #1-16,000.

Figure 7.7. From Figure 7.6 and Figure 7.7, the PSDs are visibly noisier, and the observed dominant peaks are unlike the ones observed for the baseline nozzle (see Figure 7.4(b), Figure 7.4(d), Figure 7.5(b) and Figure 7.5(c)) where the normalized amplitude of the next highest peak is at most 0.5. In addition, the peak amplitudes do not occur at the same Strouhal number across the different test cases, where Figure 7.6(c) shows the only PSD that displays a peak Strouhal number of 0.25 corresponding to the intermittent jet screech frequency.

For the 60° non-screeching bevelled nozzle, results based on varying the subsampling frequency and sample size are shown in Figure 7.8 and Figure 7.9 respectively. These results are similar to those of the 30° bevelled nozzle, in that the PSDs are noisy and there is no common peak Strouhal number existing across the different test cases. In a way, these results also reinforces the notion that the jet screech and turbulent flow structures are related, since an intermittent jet screech with lower SPL (i.e. 30° bevelled nozzle) and a non-screeching jet (i.e. 60° bevelled nozzle) both lead to PSDs (i.e. a derivative of the turbulent flow structures) that are less likely to reveal the correct screech frequency.

Several important points can be highlighted here based on the observations made in this section. Firstly, it is clear that for an intermittent jet screech problem (i.e. baseline nozzle), performing POD on a large sample size may lead to erroneous results (see Figure 7.4(a)). To further aggravate the problem, performing POD on a small sample size does not necessarily lead to the correct results either, as it is dependent on the choice of images selected to form the image samples (see Figure 7.5(a) and Figure 7.5(b)). If anything, these results show that for an intermittent

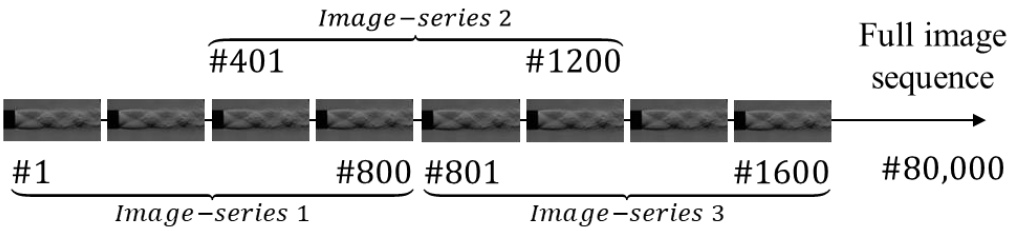

Figure 7.10: Short-time POD performed on overlapping image-series

screech tone, the PSDs are highly dependent upon the choice of sample size, subsampling frequency and image samples. Secondly, for an intermittent jet screech with lower SPL (i.e. 30° bevelled nozzle), the PSDs are much less reliable than those observed for the baseline nozzle. It is challenging to accurately characterize the nature and frequency of the jet screech based on spectra analysis of the POD coefficients without prior knowledge of the acoustic field. Finally, for a non-screeching jet (i.e. 60° bevelled nozzle), the PSD results alone are not sufficient to confirm the lack of screech tones.

7.3.1.2 Short-time POD

Based on the results presented in Section 7.3.1.1, a more robust method is required in order to accurately characterize the nature and frequency of the jet screech. The ideal scenario is to use the maximum data sampling frequency on the smallest possible sample size so as to localize the influence of transient effects in a single POD analysis. Multiple PODs can then be performed with the same data sampling frequency and sample size but with a time-shifted series of images. This is conceptually similar to the short-time Fourier transform (STFT) method and it also offers computational advantages as the multiple POD computations can be easily parallelized.

For all three nozzles, short-time POD was performed by dividing the full image sequence comprising of 80,000 images into shorter image-series of length n=800, with a sampling frequency of f_s. Each image-series overlapped with the next series by 50% of the image-series length, and 199 image-series were processed using POD. The first 3 image-series are shown in Figure 7.10 for better clarity. Peak frequencies from the 199 PSD estimates were then non-dimensionalized as Strouhal numbers and plotted against their corresponding image-series indices in Figure 7.11(i). The corresponding histogram with a bin width of St=0.01 is subsequently plotted in Figure 7.11(ii) to reveal the frequency of occurrence (out of a total of 199 PSDs) for a single Strouhal number bin.

For the baseline nozzle results shown in Figure 7.11(a), the statistical mode ($Mo = 1$) occurs at St=0.25 which agrees well with the acoustically-measured jet screech frequency. The frequency of occurrence of the statistical mode, $F(Mo = 1)$, is at 30.7% with 61 out of 199 PSDs falling within the St=0.25 bin. In contrast, the next highest frequency of occurrence, $F(Mo = 2)$, is at 4% only with 8 PSDs falling within the St=0.01 bin. For the 30° bevelled nozzle results shown in Figure 7.11(b), the statistical mode ($Mo = 1$) occurs at St=0.25 which agrees well with the acoustically-measured jet screech frequency, and $F(Mo = 1)$ is 10.1% with 20 PSDs falling within the St=0.25 bin. The next highest frequency of occurrence, $F(Mo = 2)$, is 6% with 12 PSDs falling within the St=0.32 bin. For the 60° bevelled nozzle results, the statistical mode ($Mo = 1$) occurs at St=0.01, $F(Mo = 1)$ is 7.5% with 15 PSDs falling within the St=0.01 bin, and $F(Mo = 2)$ is 6% with 12 PSDs falling

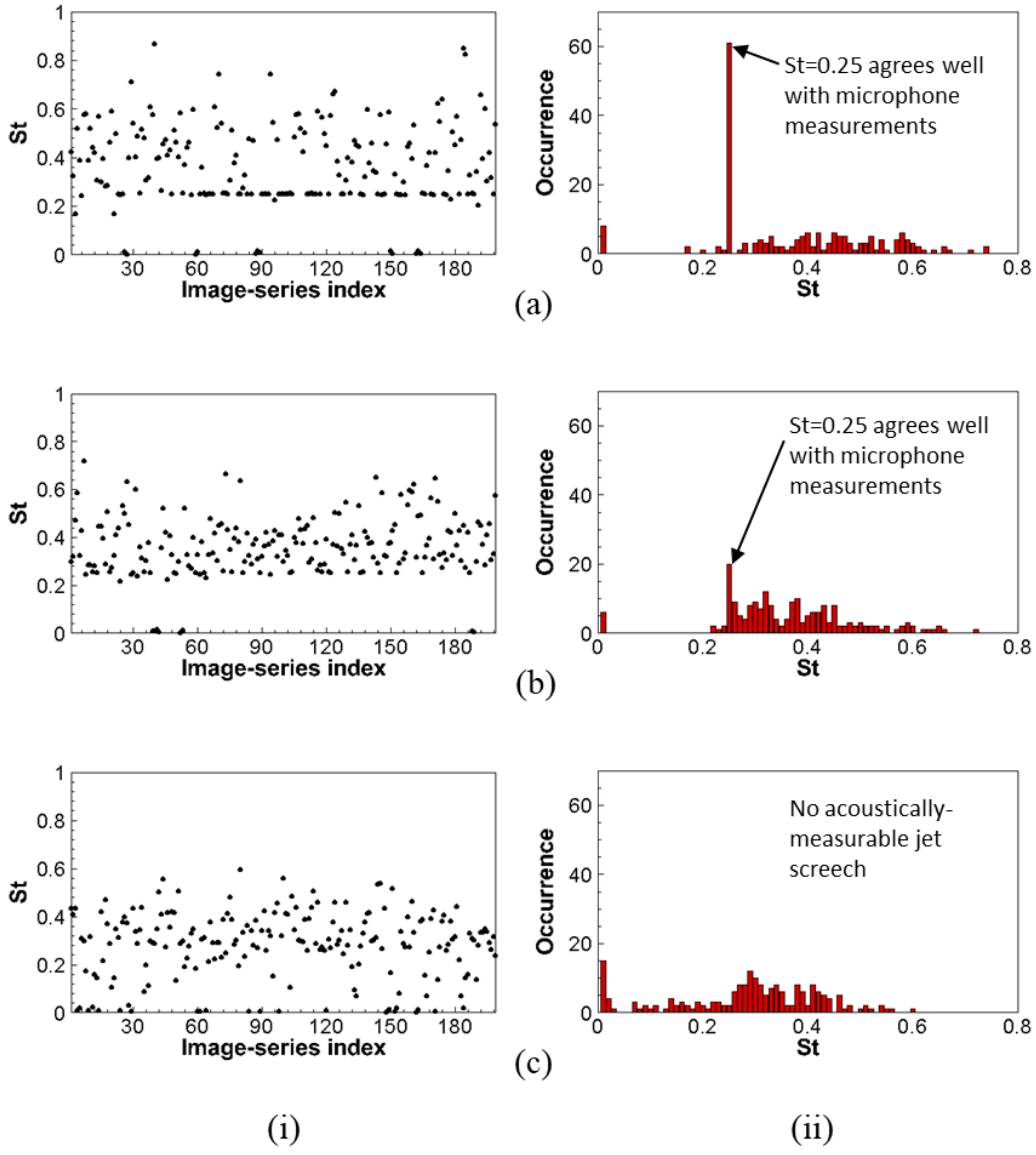

Figure 7.11: Short-time POD for (a) baseline, (b) 30° bevelled and (c) 60° bevelled nozzles. (i) Peak St for each image-series and (ii) the corresponding histogram.

within the St=0.29 bin. A summary of the top four highest frequency of occurrence for each of the test jet is tabulated in Table 7.2.

These results indicate that the frequency of occurrence for the statistical mode, hereinafter referred to as $F(Mo = 1)$, may be a suitable parameter for characterizing

Table 7.2: Summary of the top four highest frequency of occurrence for the screeching baseline nozzle, screeching 30° bevelled nozzle and non-screeching 60° bevelled nozzle.

	Baseline nozzle	30° bevelled nozzle	60° bevelled nozzle
$F(Mo = 1)$	30.7%	10.1%	7.5%
$F(Mo = 2)$	4%	6%	6%
$F(Mo = 3)$	3%	5%	5%
$F(Mo = 4)$	3%	4.5%	4%

the nature of the jet screech, particularly when comparisons are made with $F(Mo = 2)$. With reference to Table 7.2, when no jet screech is present (i.e. 60° bevelled nozzle), $F(Mo = 1)$ is low and comparable to $F(Mo = 2)$. For an intermittent jet screech with low SPL (i.e. 30° bevelled nozzle), $F(Mo = 1)$ is relatively higher and at least 1.5 times larger than $F(Mo = 2)$. For an intermittent jet screech (i.e. baseline nozzle), data points tend to cluster about a single Strouhal number with very high values of $F(Mo = 1)$, and the ratio of $F(Mo = 1) \Big/ F(Mo = 2)$ is much higher than those observed in the other two bevelled nozzles. Based on these observations, it is postulated that for a steady jet screech problem where flow structures associated with screech would be present in all image-series, $F(Mo = 1)$ and $F(Mo = 1) \Big/ F(Mo = 2)$ are both expected to be much higher than what was observed for the intermittent jet screech produced by the current baseline nozzle. Once the presence and nature of the jet screech has been ascertained, the frequency associated with the statistical mode $(Mo = 1)$ may then reveal the jet screech frequency as demonstrated earlier.

It should be noted that the present findings also highlight a key limitation of the schlieren-based POD technique, in that it does not have the capability to discern whether the jet screech intermittency is related to the absence/attenuation of the jet screech SPL or due to a shift of the jet screech frequency. Nonetheless, since the neighbouring data points are very scattered across different Strouhal numbers as shown in Figure 7.11(i), it seems unlikely for the jet screech frequency to have shifted by such a large extent and the more likely explanation is that the jet screech amplitude is time-dependent. Lastly, it is further speculated that the proposed method identifies jet screech when the SPL values are high (i.e. loud jet screech), and the occurrence of St=0.25 in the 61 out of 199 PSDs (see Figure 7.11(a)) may be related to the acoustic measurements which display higher SPL levels of the jet screech.

7.3.2 Summary

The possibility of using schlieren-based POD as a tool to detect and characterize the frequency of an intermittent jet screech problem has been demonstrated. The acoustic literature indicate that the jet screech frequency remains constant over all measured polar angles, while the BSAN peak and turbulent mixing noise spectra are dependent upon the measured polar angles. This indicates that the time-resolved schlieren-based POD can only be applied for jet screech identification and frequency characterization, since POD modes cannot be further decomposed in terms of wave directivity. High-speed schlieren images were captured with particular attention to the turbulent flow structures located within the first 5D from the nozzle origins and extra care was taken to avoid capturing the acoustic waves. POD was performed on these images, and the PSD of the first POD mode peaked at precisely the acoustically-measured screech

frequency of St=0.25. This suggests the existence of a correlation between POD filtered turbulent structures and jet screech. However, the results are contingent upon the sample size, subsampling frequency and even the image samples. This contingency was found to be due to the intermittency of the jet screech itself, confirmed by the short-time POD analysis of the schlieren images as well as the acoustic measurements performed independently by another researcher.

The short-time POD analysis is proposed as a robust method that can characterize the nature and presence of the jet screech using the parameters $F(Mo = 1)$ and $F(Mo = 1) \Big/ F(Mo = 2)$, while the frequency associated with the statistical mode $(Mo = 1)$ reveals the screech frequency if present. For the baseline nozzle which exhibits intermittent jet screech, $F(Mo = 1)$ is relatively higher at 30.7% as compared to the next highest frequency of occurrence, $F(Mo = 2)$, at 4%. For the 30° bevelled nozzle where the jet screech is intermittent and partially mitigated based on the lower SPL from the near-field noise spectra, $F(Mo = 1)$ is low at 10.1% and at least 1.5 times that of $F(Mo = 2)$, at 6%. For the 60° bevelled nozzle where jet screech was no longer present, the value of $F(Mo = 1)$ is the lowest at 7.5% and comparable to $F(Mo = 2)$ at 6%. As a stand-alone approach, schlieren-based POD technique is capable of characterizing the nature and frequency of jet screech. Nonetheless, further studies on jets that display steady screech, intermittent screech and lack of screech tone are required to verify the suitability of using $F(Mo = 1)$ as a parameter for characterizing the presence and nature of jet screech, as well as to validate that the frequency associated with the statistical mode $(Mo = 1)$ correctly reveals the screech frequency when screech is present. When used in conjunction

with acoustic measurements, the technique allows a direct link between the turbulent structures and jet screech tone to be established.

Chapter 8 Conclusions

The current research problems associated with supersonic jets include poor understanding of supersonic jet noise, lack of experimental results particularly for nonconventional nozzles, and the limitations of existing experimental techniques which deters extensive studies on optimal supersonic jet nozzle designs. As such, the following research objectives were formulated to address these issues:

(1) Develop a schlieren-based 3D shock wave reconstruction technique that can avoid the need to measure a prior fluid property.
(2) Demonstrate the capability of the 3D shock wave reconstruction technique by extending it to analyse highly complex and asymmetric shock structures in supersonic impinging bevelled jets.
(3) Develop a schlieren-based velocimetry technique which does not rely on seeding particles and is able to offer higher spatial and temporal resolution as compared to existing PIV techniques.
(4) Develop a data-driven schlieren-based flow diagnostics technique for supersonic jet screech studies.
(5) Provide experimental data for supersonic jets produced by nonconventional nozzles.

In this thesis, a novel 3D shock wave reconstruction technique based on schlieren imagery and voxel-based visual hull reconstruction concepts was presented in Chapter 4. The proposed technique is able to directly reconstruct shock waves without the need to measure the global velocity or density field. The study focuses

on moderately under-expanded bevelled jets which produced stable and asymmetric shock structures that allow images at different view angles to be captured at different time instances. Coupled with the use of an in-house developed semi-synthetic camera calibration technique, multiple camera calibration issues commonly faced by tomographic techniques in asymmetric test cases can be avoided while simultaneously providing very precise camera parameters in the miniature shock wave reconstruction application. The reconstructed shock waves are highly accurate and provided quantitative geometrical information to further complement shock structure visualizations. The average error associated with the key geometrical parameters is 2.5% and the nominal cubic voxel resolution of the reconstructed shock wave is 0.044 mm. As such, the technique developed here has the advantage of low hardware requirements, low computation time, ease of implementation, and high-resolution and accurate reconstructed 3D shock waves. Due to these traits, it is particularly well-suited for nozzle optimization studies. The study presented in Chapter 4 addresses research objective (1) while simultaneously providing additional experimental data of shock systems produced by bevelled circular nozzles (research objective (5)). For future work, neural networks can be used to further improve the feature extraction process in the image post-processing procedures. This has been identified to be the largest source of error and machine learning has the potential to outperform the current edge detection and manual spline fitting methods. The reconstruction technique can also be applied to a wider range of problems that it is well-suited for, such as the optimization of multi-shock designs at supersonic inlet or the study of shock geometries in hypersonic flows.

The effects of bevelled nozzles on standoff shocks produced by moderately under-expanded supersonic impinging jets were studied in Chapter 5. This was motivated by the lack of research focusing on flow control of impinging jets using nonconventional nozzles, despite the possibility of manipulating the flow and shock characteristics associated with the impingement behaviour favourably. The properties of the standoff shock are known to be a strong function of the NPR and separation distance based on the existing literature. Hence, these parameters were varied in a systematic manner, and both traditional 2D schlieren and the novel 3D shock wave reconstruction techniques were performed on the standoff shock. The results revealed that the bevelled nozzles are effective in introducing asymmetry to the geometry of the standoff shock, alter its stability characteristics, and change its relative position to the impingement plate. The position and strength of the reflection point with respect to the standoff shock was observed to have a strong influence on the standoff shock properties, and this is postulated to be due to its adverse pressure gradient creating a localized suction effect on the standoff shock. The study presented in Chapter 5 addresses research objective (2) by making use of the novel 3D reconstruction technique stemming from research objective (1). At the same time, additional experimental data of shock systems produced by impinging bevelled circular nozzles are presented (research objective (5)). For future work, velocity, pressure and acoustic measurements can be performed to ascertain the presence of the stagnation bubble, reveal the plate pressure distribution and quantify the noise levels associated with changes observed in the standoff shock. These additional quantitative data can also be used to reaffirm the physical mechanisms proposed in the current study.

Schlieren image velocimetry based on an in-house optical flow algorithm (i.e. SIVOF) was presented in Chapter 6. The development of SIVOF was focused on two main aspects; obtaining the optimal schlieren images for optical flow analysis, and development of the optical flow model and minimization methods for the in-house optical flow algorithm. A systematic study was performed to determine the optimal image spatial resolution, exposure time and framing rates. The optimal spatial resolution and exposure time were observed to be easily achieved based on sample schlieren images, while the optimal framing rate was found to be difficult to achieve even with the use of ultrahigh-speed Photron SAX2 or Phantom v2512 cameras. In terms of the optical flow algorithm, modern minimization methods such as GNC, robust penalty functions and multi-resolution schemes were incorporated with an optical flow model which made use of a second order div-curl regularizer that is more physically meaningful in the current application. This resulted in the in-house SIVOF technique outperforming a competitive open source optical flow algorithm during the synthetic schlieren image validation test. Finally, SIVOF was applied to over-expanded baseline and 30° bevelled jets, and the results were compared with traditional 2D PIV. Sharper and clearer vortical structures were observed from the SIVOF results and an embedded shear layer behind a Mach disk was successfully resolved, which clearly demonstrates the advantage of having a higher spatial resolution. The study presented in Chapter 6 addresses research objective (3). For future work, the double-camera schlieren setup can be further refined and employed to provide optimal images for more accurate SIVOF results. The optical flow algorithm can be further improved by making use of the time-resolved velocity fields as an additional constraint to regularize the OFCE, resulting in more physically

meaningful results. More importantly, high-fidelity numerical results or ground truths need to be created by experts in the SIV field and made publicly available. This will allow novel SIV methods to be properly validated and benchmarked, which is necessary for serious development of SIV methods.

A new approach to identify and characterize intermittent jet screech based on time-resolved schlieren-based POD is presented in Chapter 7. Time-resolved schlieren imaging of turbulent flow structures were performed for moderately under-expanded supersonic jets emanating from a circular baseline and two bevelled nozzles. POD was performed on the images and the spectral analysis on the time coefficients of the first POD mode revealed a peak amplitude at precisely the acoustically-validated screech frequency of St=0.25 for the baseline jet. This suggests a correlation between the POD filtered turbulent flow structures and the screech tone. Short-time POD was performed to robustly identify the presence and characterize the type of intermittent jet screech based on the proposed parameter of $F(Mo = 1)$. If screech is indeed present, the frequency associated with the statistical mode ($Mo = 1$) can then reveal its frequency. The study presented in Chapter 7 addresses research objective (4) by proposing a new image-based experimental technique for aeroacoustics studies, and research objective (5) by shedding further light onto the phenomenon of jet screech intermittency. For future work, studies on jets that display steady, intermittent and lack of screech tone are required in order to verify the suitability of the proposed parameters. Time-resolved schlieren can also be conducted with acoustic measurements simultaneously in order to correlate the results and reveal further insights onto the phenomenon of jet screech intermittency.

List of Publications

Journals

1. **Lim, H.D**., Ding J., and Shi, S., New, T.H., *Proper orthogonal decomposition analysis of near-field coherent structures associated with V-notched nozzle jets*. **Experimental Thermal and Fluid Science**, 2020. **112**: p. 109972.

2. **Lim, H.D**., New, T.H., Mariani, R., Cui, Y.D., *Effects of bevelled nozzles on standoff shocks in supersonic impinging jets*. **Aerospace Science and Technology**, 2019. **94:** p. 105371.

3. Wei, X.F., Mariani, R., Chua, L.P., **Lim, H.D**., Lu, Z.B., Cui, Y.D., New T.H., *Mitigation of under-expanded supersonic jet noise through stepped nozzles.* **Journal of Sound and Vibration**, 2019. **459**: p. 114875.

4. Mariani, R., Zang, B., **Lim, H.D.**, Vevek, US., New, T.H., and Cui, Y.D., *A comparative study on the use of calibrated and rainbow schlieren techniques in axisymmetric supersonic jets.* **Flow Measurement and Instrumentation**, 2019. **66**: p. 218-228.

5. Wu, J., **Lim, H.D.**, Wei, X.F., New, T.H., and Cui, Y.D., *Flow characterization of supersonic jets issuing from double-beveled nozzles.* **Journal of Fluids Engineering**, 2019. **141**(1): p. 011202.

6. Zang, B., Vevek, U S., **Lim, H.D.**, Wei, X.F., and New, T.H., *An assessment of OpenFOAM solver on RANS simulations of round supersonic free jets.* **Journal of Computational Science**, 2018. **28**: p. 18-31.

7. **Lim, H.D.**, New, T.H., Mariani, R., and Cui, Y.D., *Visual hull based 3D reconstruction of shocks in under-expanded supersonic bevelled jets.* **Experimental Thermal and Fluid Science**, 2018. **99**: p. 458-473.

Conferences

1. Mariani, R., **Lim, H.D**., Vevek, U.S., Zang, B., New, T.H. and Cui, Y.D., *A preliminary study on the implementation of rainbow schlieren with a single-mirror system*, in ***32nd International Symposium on Shock Waves (ISSW32)***. 2019: Singapore.

2. Ding, J., **Lim, H.D**., Sheikh, S., Shengming, X., Shi, S., and New, T.H., *Volumetric measurement of a supersonic jet with single-camera light-field*

PIV, in ***19th International Symposium on the Application of Laser and Imaging Techniques to Fluid Mechanics***. 2018: Lisbon, Portugal.

3. **Lim, H.D**., New, T.H., and Cui, Y.D., *A semi-synthetic camera calibration method for 3D reconstruction of shocks in supersonic jets*, in ***19th International Symposium on the Application of Laser and Imaging Techniques to Fluid Mechanics***. 2018: Lisbon, Portugal.

4. Mariani, R., **Lim, H.D**., Zang, B., Vevek, U.S., New, T.H., and Cui, Y.D., *A comparison of calibrated and rainbow schlieren in axisymmetric supersonic jets*, in ***19th International Symposium on the Application of Laser and Imaging Techniques to Fluid Mechanics***. 2018: Lisbon, Portugal.

5. Mariani, R., **Lim, H.D**., Vevek, U.S., Zang, B., Cui, Y.D., and New, T.H., *On the application of calibrated schlieren for the analysis of axisymmetric and asymmetric supersonic jets*, in ***11th Pacific Symposium on Flow Visualization and Image Processing***. 2017: Kumamoto, Japan.

6. **Lim, H.D**., New, T.H., Cui, Y.D., and Shi, S., *Time-resolved optical flow of supersonic bevelled nozzles*, in ***31st International Symposium on Shock Waves (ISSW31)***. 2017: Nagoya, Japan.

7. **Lim, H.D**., Zang, B., Cui, Y.D., and New, T.H., *Supersonic PIV measurements of over-expanded beveled jets*, in ***12th International Symposium on Particle Image Velocimetry***. 2017: Busan, Korea.

8. Wu J., **Lim, H.D.**, Wei, X., New, T.H., Cui, Y.D., and Wang, Q., *An Experimental Investigation on Supersonic Jets Issuing from Beveled Nozzles*, in ***14th Asian Symposium on Visualization (ASV14), 2017 ASV Conference***. 2017: Beijing, China.

9. **Lim, H.D**., Wu, J., Wei, X., New, T.H., Cui, Y.D., and Shi, S., *Challenges of optical flow analysis in supersonic jets*, in ***55th AIAA Aerospace Sciences Meeting***. 2016: Grapevine, Texas, USA.

10. **Lim, H.D**., Wu, J., New, T.H., and Shi, S., *Optical flow technique for supersonic jet measurements*, in ***18th International Conference on Fluid Dynamics and Thermodynamics***. 2015: London, United Kingdom.

References

1. Glezer, A. and M. Amitay, *Synthetic jets.* Annual Review of Fluid Mechanics, 2002. **34**(1): p. 503-529.

2. Gutmark, E. and F. Grinstein, *Flow control with noncircular jets.* Annual Review of Fluid Mechanics, 1999. **31**(1): p. 239-272.

3. Jambunathan, K., E. Lai, M. Moss, and B. Button, *A review of heat transfer data for single circular jet impingement.* International Journal of Heat and Fluid Flow, 1992. **13**(2): p. 106-115.

4. Tam, C.K., *Supersonic jet noise.* Annual Review of Fluid Mechanics, 1995. **27**(1): p. 17-43.

5. Crow, S.C. and F. Champagne, *Orderly structure in jet turbulence.* Journal of Fluid Mechanics, 1971. **48**(3): p. 547-591.

6. Brown, G.L. and A. Roshko, *On density effects and large structure in turbulent mixing layers.* Journal of Fluid Mechanics, 1974. **64**(4): p. 775-816.

7. Schlichting, H. and K. Gersten, *Boundary-layer theory*. 2003: Springer Science & Business Media.

8. Gutmark, E. and C.M. Ho, *Preferred modes and the spreading rates of jets.* Physics of Fluids, 1983. **26**(10): p. 2932-2938.

9. Michalke, A., *On spatially growing disturbances in an inviscid shear layer.* Journal of Fluid Mechanics, 1965. **23**(3): p. 521-544.

10. Mohan, N.D., K. Prakash, and N. Panchapakesan, *Mixing augmentation by multiple lobed jets.* American Journal of Fluid Dynamics, 2015. **5**(2): p. 55-64.

11. Winant, C.D. and F.K. Browand, *Vortex pairing: the mechanism of turbulent mixing-layer growth at moderate Reynolds number.* Journal of Fluid Mechanics, 1974. **63**(2): p. 237-255.

12. Hussain, A.F., *Coherent structures and turbulence.* Journal of Fluid Mechanics, 1986. **173**: p. 303-356.

13. Back, L.D. and V. Sarohia, *Pressure pulsations on a flat plate normal to an underexpanded supersonic jet.* AIAA Journal, 1978. **16**(6): p. 634-636.

14. Franquet, E., V. Perrier, S. Gibout, and P. Bruel, *Free underexpanded jets in a quiescent medium: a review.* Progress in Aerospace Sciences, 2015. **77**: p. 25-53.

15. Ginzburg, I., B. Semiletenko, V. Terpigor'ev, and V. Uskov, *Some singularities of supersonic underexpanded jet interaction with a plane obstacle.* Journal of Engineering Physics, 1970. **19**(3): p. 1081-1084.

16. Lamont, P.J. and B.L. Hunt, *The impingement of underexpanded, axisymmetric jets on perpendicular and inclined flat plates.* Journal of Fluid Mechanics, 1980. **100**(3): p. 471-511.

17. Mitchell, D.M., D.R. Honnery, and J. Soria, *The visualization of the acoustic feedback loop in impinging underexpanded supersonic jet flows using ultra-high frame rate schlieren.* Journal of Visualization, 2012. **15**(4): p. 333-341.

18. Panda, J., *Shock oscillation in underexpanded screeching jets.* Journal of Fluid Mechanics, 1998. **363**: p. 173-198.

19. Powell, A., *The sound‐producing oscillations of round underexpanded jets impinging on normal plates.* The Journal of the Acoustical Society of America, 1988. **83**(2): p. 515-533.

20. Venkatakrishnan, L., *Density measurements in an axisymmetric underexpanded jet by background-oriented schlieren technique.* AIAA Journal, 2005. **43**(7): p. 1574.

21. Powell, A., *On the mechanism of choked jet noise.* Proceedings of the Physical Society. Section B, 1953. **66**(12): p. 1039.

22. Powell, A., *On the noise emanating from a two-dimensional jet above the critical pressure.* The Aeronautical Quarterly, 1953. **4**(2): p. 103-122.

23. Harper-Bourne, M. and M.J. Fisher, *The noise from shock waves in supersonic jets.* AGARD CP-131, 1974.

24. Tam, C.K. and H. Tanna, *Shock associated noise of supersonic jets from convergent-divergent nozzles.* Journal of Sound and Vibration, 1982. **81**(3): p. 337-358.

25. Raman, G., *Advances in understanding supersonic jet screech: Review and perspective.* Progress in Aerospace Sciences, 1998. **34**(1-2): p. 45-106.

26. Tam, C.K., *Stochastic model theory of broadband shock associated noise from supersonic jets.* Journal of Sound and Vibration, 1987. **116**(2): p. 265-302.

27. Wu, J. and T.H. New, *An investigation on supersonic bevelled nozzle jets.* Aerospace Science and Technology, 2017. **63**: p. 278-293.

28. Tam, C.K., J.M. Seiner, and J. Yu, *Proposed relationship between broadband shock associated noise and screech tones.* Journal of Sound and Vibration, 1986. **110**(2): p. 309-321.

29. Gutmark, E., K. Schadow, and K. Yu, *Mixing enhancement in supersonic free shear flows.* Annual Review of Fluid Mechanics, 1995. **27**(1): p. 375-417.

30. Papamoschou, D. and A. Roshko, *The compressible turbulent shear layer: an experimental study.* Journal of Fluid Mechanics, 1988. **197**: p. 453-477.

31. Papamoschou, D., *Structure of the compressible turbulent shear layer.* AIAA Journal, 1991. **29**(5): p. 680-681.

32. Lele, S. *Direct numerical simulation of compressible free shear flows*. in *27th Aerospace Sciences Meeting*. 1989.

33. Papamoschou, D. and A. Bunyajitradulya, *Evolution of large eddies in compressible shear layers.* Physics of Fluids, 1997. **9**(3): p. 756-765.

34. Murakami, E. and D. Papamoschou, *Eddy convection in coaxial supersonic jets.* AIAA Journal, 2000. **38**(4): p. 628-635.

35. Papamoschou, D., *Mach wave elimination in supersonic jets.* AIAA Journal, 1997. **35**(10): p. 1604-1611.

36. Papamoschou, D., *Mixing Enhancement using Axial Flow*. AIAA paper, 2000. **93**: p. 2000.

37. Papamoschou, D. and A. Johnson, *Unsteady Phenomena in Supersonic Nozzle Flow Separation.* AIAA Paper, 2006. **3360**: p. 2006.

38. Papamoschou, D., A. Zill, and A. Johnson, *Supersonic flow separation in planar nozzles.* Shock Waves, 2009. **19**(3): p. 171-183.

39. Wlezien, R. and V. Kibens, *Passive control of jets with indeterminate origins.* AIAA Journal, 1986. **24**(8): p. 1263-1270.

40. Wlezien, R. and V. Kibens, *Influence of nozzle asymmetry on supersonic jets.* AIAA Journal, 1988. **26**(1): p. 27-33.

41. Wu, J., H.D. Lim, X. Wei, T.H. New, and Y.D. Cui, *Flow characterization of supersonic jets issuing from double-beveled nozzles.* Journal of Fluids Engineering, 2019. **141**(1): p. 011202.

42. Lim, H.D., T.H. New, R. Mariani, and Y.D. Cui, *Visual hull based 3D reconstruction of shocks in under-expanded supersonic bevelled jets.* Experimental Thermal and Fluid Science, 2018. **99**: p. 458-473.

43. Rice, E.J. and G. Raman. *Supersonic jets from bevelled rectangular nozzles*. in *Winter Annual Meeting of the ASME Symposium on Flow Acoustics Interaction and Fluid Control*. 1993. New Orleans, Louisiana.

44. Rice, E. and G. Raman. *Mixing noise reduction for rectangular supersonic jets by nozzle shaping and induced screech mixing*. in *15th Aeroacoustics Conference*. 1993.

45. Raman, G., *Screech tones from rectangular jets with spanwise oblique shock-cell structures.* Journal of Fluid Mechanics, 1997. **330**: p. 141-168.

46. Samimy, M., J.H. Kim, and P. Clancy. *Supersonic jet noise reduction and mixing enhancement through nozzle trailing edge modifications*. in *35th Aerospace Sciences Meeting and Exhibit*. 1997.

47. Vinze, R., M.D. Limeye, and S.V. Prabhu, *Influence of the elliptical and circular orifices on the local heat transfer distribution of a flat plate impinged by under-expanded jets.* Heat and Mass Transfer, 2017. **53**(4): p. 1439-1455.

48. Wernet, M.P., *Application of tomo-PIV in a large-scale supersonic jet flow facility.* Experiments in Fluids, 2016. **57**(9): p. 144.

49. Papamoschou, D., *A two-spark schlieren system for very-high velocity measurement.* Experiments in Fluids, 1989. **7**(5): p. 354-356.

50. Settles, G.S., *Schlieren and shadowgraph techniques: visualizing phenomena in transparent media*. 2012: Springer Science & Business Media.

51. Settles, G.S. and M.J. Hargather, *A review of recent developments in schlieren and shadowgraph techniques.* Measurement Science and Technology, 2017. **28**(4): p. 042001.

52. Atcheson, B., W. Heidrich, and I. Ihrke, *An evaluation of optical flow algorithms for background oriented schlieren imaging.* Experiments in Fluids, 2009. **46**(3): p. 467-476.

53. Hayasaka, K., Y. Tagawa, T. Liu, and M. Kameda, *Optical-flow-based background-oriented schlieren technique for measuring a laser-induced underwater shock wave.* Experiments in Fluids, 2016. **57**(12): p. 179.

54. Raffel, M., *Background-oriented schlieren (BOS) techniques.* Experiments in Fluids, 2015. **56**(3): p. 1-17.

55. Hargather, M.J., M.J. Lawson, G.S. Settles, and L.M. Weinstein, *Seedless velocimetry measurements by schlieren image velocimetry.* AIAA Journal, 2011. **49**(3): p. 611-620.

56. Sourgen, F., F. Leopold, and D. Klatt, *Reconstruction of the density field using the colored background oriented schlieren technique (CBOS).* Optics and Lasers in Engineering, 2012. **50**(1): p. 29-38.

57. Venkatakrishnan, L. and G. Meier, *Density measurements using the background oriented schlieren technique.* Experiments in Fluids, 2004. **37**(2): p. 237-247.

58. Atcheson, B., I. Ihrke, W. Heidrich, A. Tevs, D. Bradley, M. Magnor, and H.-P. Seidel. *Time-resolved 3d capture of non-stationary gas flows*. in *ACM Transactions on Graphics (TOG)*. 2008. ACM.

59. Nicolas, F., V. Todoroff, A. Plyer, G. Le Besnerais, D. Donjat, F. Micheli, F. Champagnat, P. Cornic, and Y. Le Sant, *A direct approach for instantaneous 3D density field reconstruction from background-oriented schlieren (BOS) measurements.* Experiments in Fluids, 2016. **57**(1): p. 13.

60. Le Sant, Y., V. Todoroff, A. Bernard-Brunel, G. Le Besnerais, F. Micheli, and D. Donjat. *Multi-camera calibration for 3DBOS*. in *17th International Symposium on Applications of Laser Techniques to Fluid Mechanics*. 2014.

61. Furukawa, Y. and J. Ponce, *Accurate camera calibration from multi-view stereo and bundle adjustment.* International Journal of Computer Vision, 2009. **84**(3): p. 257-268.

62. Torr, P.H. and A. Zisserman. *Feature based methods for structure and motion estimation*. in *Workshop on Vision Algorithms*. 1999. Springer.

63. Dyer, C.R., *Volumetric scene reconstruction from multiple views*, in *Foundations of Image Understanding*. 2001, Springer. p. 469-489.

64. Slabaugh, G., R. Schafer, T. Malzbender, and B. Culbertson. *A survey of methods for volumetric scene reconstruction from photographs*. in *Volume Graphics 2001*. 2001. Springer.

65. Fua, P., *A parallel stereo algorithm that produces dense depth maps and preserves image features.* Machine Vision and Applications, 1993. **6**(1): p. 35-49.

66. Zhang, Z., R. Deriche, O. Faugeras, and Q.-T. Luong, *A robust technique for matching two uncalibrated images through the recovery of the unknown epipolar geometry*. Artificial Intelligence, 1995. **78**(1): p. 87-119.

67. Torr, P.H. and A. Zisserman. *Feature Based Methods for Structure and Motion Estimation*. in *International Workshop on Vision Algorithms*. 1999. Springer.

68. Lowe, D.G., *Distinctive image features from scale-invariant keypoints.* International Journal of Computer Vision, 2004. **60**(2): p. 91-110.

69. Rothwell, C.A., A. Zisserman, D.A. Forsyth, and J.L. Mundy, *Planar object recognition using projective shape representation.* International Journal of Computer Vision, 1995. **16**(1): p. 57-99.

70. Bay, H., A. Ess, T. Tuytelaars, and L. Van Gool, *Speeded-up robust features (SURF).* Computer Vision and Image Understanding, 2008. **110**(3): p. 346-359.

71. Bay, H., T. Tuytelaars, and L. Van Gool. *Surf: speeded up robust features*. in *European Conference on Computer Vision*. 2006. Springer.

72. Wang, Q. and Y. Zhang, *High speed Stereoscopic Shadowgraph Imaging and its Digital 3D Reconstruction.* Measurement Science and Technology, 2011. **22**(6): p. 065302.

73. Ng, W.B. and Y. Zhang, *Stereoscopic imaging and reconstruction of the 3D geometry of flame surfaces.* Experiments in Fluids, 2003. **34**(4): p. 484-493.

74. Baumgart, B.G., *Geometric modeling for computer vision*. 1974, DTIC Document.

75. Laurentini, A., *The visual hull concept for silhouette-based image understanding.* IEEE Transactions on pattern analysis and machine intelligence, 1994. **16**(2): p. 150-162.

76. Matusik, W., C. Buehler, R. Raskar, S.J. Gortler, and L. McMillan. *Image-based visual hulls*. in *Proceedings of the 27th Annual Conference on Computer Graphics and Interactive Techniques*. 2000. ACM Press/Addison-Wesley Publishing Co.

77. Baker, S., D. Scharstein, J. Lewis, S. Roth, M.J. Black, and R. Szeliski, *A database and evaluation methodology for optical flow.* International Journal of Computer Vision, 2011. **92**(1): p. 1-31.

78. Horn, B.K. and B.G. Schunck. *Determining optical flow*. in *1981 Technical Symposium East*. 1981. International Society for Optics and Photonics.

79. Brox, T., A. Bruhn, N. Papenberg, and J. Weickert, *High accuracy optical flow estimation based on a theory for warping*, in *Computer Vision-ECCV 2004*. 2004, Springer. p. 25-36.

80. Barron, J.L., D.J. Fleet, and S.S. Beauchemin, *Performance of optical flow techniques.* International Journal of Computer Vision, 1994. **12**(1): p. 43-77.

81. Heitz, D., E. Mémin, and C. Schnörr, *Variational fluid flow measurements from image sequences: synopsis and perspectives.* Experiments in Fluids, 2010. **48**(3): p. 369-393.

82. Corpetti, T., D. Heitz, G. Arroyo, E. Memin, and A. Santa-Cruz, *Fluid experimental flow estimation based on an optical-flow scheme.* Experiments in Fluids, 2006. **40**(1): p. 80-97.

83. Corpetti, T., É. Mémin, and P. Pérez, *Dense estimation of fluid flows.* IEEE Transactions on Pattern Analysis and Machine Intelligence, 2002. **24**(3): p. 365-380.

84. Liu, T. and L. Shen, *Fluid Flow and Optical Flow.* Journal of Fluid Mechanics, 2008. **614**: p. 253-291.

85. Ruhnau, P., A. Stahl, and C. Schnörr, *Variational estimation of experimental fluid flows with physics-based spatio-temporal regularization.* Measurement Science and Technology, 2007. **18**(3): p. 755.

86. Heitz, D., P. Héas, E. Mémin, and J. Carlier, *Dynamic consistent correlation-variational approach for robust optical flow estimation.* Experiments in Fluids, 2008. **45**(4): p. 595-608.

87. Ruhnau, P., T. Kohlberger, C. Schnörr, and H. Nobach, *Variational optical flow estimation for particle image velocimetry.* Experiments in Fluids, 2005. **38**(1): p. 21-32.

88. Brox, T. and J. Malik, *Large Displacement Optical Flow: Descriptor Matching in Variational Motion Estimation.* Pattern Analysis and Machine Intelligence, IEEE Transactions on, 2011. **33**(3): p. 500-513.

89. Sun, D., S. Roth, and M.J. Black. *Secrets of optical flow estimation and their principles*. in *Computer Vision and Pattern Recognition (CVPR), 2010 IEEE Conference on*. 2010. IEEE.

90. Black, M.J. and P. Anandan, *The robust estimation of multiple motions: parametric and piecewise-smooth flow fields.* Computer Vision and Image Understanding, 1996. **63**(1): p. 75-104.

91. Memin, E. and P. Perez. *A multigrid approach for hierarchical motion estimation*. in *Computer Vision, 1998. Sixth International Conference on*. 1998. IEEE.

92. Heitz, F., P. Perez, and P. Bouthemy, *Multiscale minimization of global energy functions in some visual recovery problems.* CVGIP: Image Understanding, 1994. **59**(1): p. 125-134.

93. Blake, A. and A. Zisserman, *Visual reconstruction*. Vol. 2. 1987: MIT press Cambridge.

94. Wedel, A., T. Pock, C. Zach, H. Bischof, and D. Cremers, *An improved algorithm for TV-L1 optical flow*, in *Statistical and Geometrical Approaches to Visual Motion Analysis*. 2009, Springer. p. 23-45.

95. Rudin, L.I., S. Osher, and E. Fatemi, *Nonlinear total variation based noise removal algorithms.* Physica D: Nonlinear Phenomena, 1992. **60**(1-4): p. 259-268.

96. Sun, D., S. Roth, and M.J. Black, *A quantitative analysis of current practices in optical flow estimation and the principles behind them.* International Journal of Computer Vision, 2014. **106**(2): p. 115-137.

97. Lumley, J.L., *The structure of inhomogeneous turbulent flows.* Atmospheric Turbulence and Radio Wave Propagation, 1967.

98. Sirovich, L., *Turbulence and the dynamics of coherent structures. I. Coherent structures.* Quarterly of Applied Mathematics, 1987. **45**(3): p. 561-571.

99. Berkooz, G., P. Holmes, and J.L. Lumley, *The proper orthogonal decomposition in the analysis of turbulent flows.* Annual Review of Fluid Mechanics, 1993. **25**(1): p. 539-575.

100. Van Oudheusden, B., F. Scarano, N. Van Hinsberg, and D. Watt, *Phase-resolved characterization of vortex shedding in the near wake of a square-section cylinder at incidence.* Experiments in Fluids, 2005. **39**(1): p. 86-98.

101. Semeraro, O., G. Bellani, and F. Lundell, *Analysis of time-resolved PIV measurements of a confined turbulent jet using POD and Koopman modes.* Experiments in Fluids, 2012. **53**(5): p. 1203-1220.

102. Shim, Y.M., R.N. Sharma, and P.J. Richards, *Proper orthogonal decomposition analysis of the flow field in a plane jet.* Experimental Thermal and Fluid Science, 2013. **51**: p. 37-55.

103. Zang, B. and T.H. New, *On the wake-like vortical arrangement and behaviour associated with twin jets in close proximity.* Experimental Thermal and Fluid Science, 2015. **69**: p. 127-140.

104. Weitao, B., S. Yasuhiko, O. Koji, and M. Haruki, *Time-resolved proper orthogonal decomposition of the near-field flow of a round jet measured by dynamic particle image velocimetry.* Measurement Science and Technology, 2003. **14**(8): p. L1.

105. Malla, B., D. Cuppoletti, J. Kastner, and E. Gutmark. *Proper orthogonal decomposition on a subsonic jet exhausted from an axisymmetric nozzle and chevron nozzles with varying penetration*. in *49th AIAA Aerospace Sciences Meeting including the New Horizons Forum and Aerospace Exposition*. 2011.

106. Sampath, R. and S. Chakravarthy, *Proper orthogonal and dynamic mode decompositions of time-resolved PIV of confined backward-facing step flow.* Experiments in fluids, 2014. **55**(9): p. 1792.

107. Lengani, D., D. Simoni, M. Ubaldi, and P. Zunino, *POD analysis of the unsteady behavior of a laminar separation bubble.* Experimental Thermal and Fluid Science, 2014. **58**: p. 70-79.

108. Berry, M.G., M.Y. Ali, A.S. Magstadt, and M.N. Glauser, *DMD and POD of time-resolved schlieren on a multi-stream single expansion ramp nozzle.* International Journal of Heat and Fluid Flow, 2017. **66**: p. 60-69.

109. Higham, J., W. Brevis, and C. Keylock, *Implications of the selection of a particular modal decomposition technique for the analysis of shallow flows.* Journal of Hydraulic Research, 2018: p. 1-10.

110. Wan, C. and S. Yu, *Investigation of air tab's effect in supersonic jets.* Journal of Propulsion and Power, 2011. **27**(5): p. 1157-1160.

111. Zhang, Z., *A flexible new technique for camera calibration.* IEEE Transactions on Pattern Analysis and Machine Intelligence, 2000. **22**(11): p. 1330-1334.

112. Tordoff, B., *Carving a dinosaur*. 2016, MATLAB Central File Exchange.

113. Fleuret, F., T. Li, C. Dubout, E.K. Wampler, S. Yantis, and D. Geman, *Comparing machines and humans on a visual categorization test.* Proceedings of the National Academy of Sciences, 2011. **108**(43): p. 17621.

114. Thorpe, S.J., *Image processing by the human visual system*, in *EurographicSeminars (Tutorials and Perspectives in Computer Graphics).* 1991, Springer Berlin Heidelberg: Berlin, Heidelberg. p. 309-341.

115. Huang, C., W.T. Nichols, D.T. O'Brien, M.F. Becker, D. Kovar, and J.W. Keto, *Supersonic jet deposition of silver nanoparticle aerosols: Correlations of impact conditions and film morphologies.* Journal of Applied Physics, 2007. **101**(6): p. 064902.

116. Kim, D. and J. Lee, *Influence of shock structure on heat transfer characteristics in supersonic under-expanded impinging jets.* International Journal of Thermal Sciences, 2019. **141**: p. 62-71.

117. Schnurr, N., J. Williamson, and J. Tatom, *An analytical investigation of the impingement of jets on curved deflectors.* AIAA Journal, 1972. **10**(11): p. 1430-1435.

118. Tsutsumi, S., T. Ishii, K. Ui, S. Tokudome, and K. Wada, *Study on acoustic prediction and reduction of epsilon launch vehicle at liftoff.* Journal of Spacecraft and Rockets, 2014. **52**(2): p. 350-361.

119. Balakrishnan, P. and K. Srinivasan, *Impinging jet noise reduction using non-circular jets.* Applied Acoustics, 2019. **143**: p. 19-30.

120. Donaldson, C.D. and R.S. Snedeker, *A study of free jet impingement. Part 1. Mean properties of free and impinging jets.* Journal of Fluid Mechanics, 1971. **45**(2): p. 281-319.

121. Donaldson, C.D., R.S. Snedeker, and D.P. Margolis, *A study of free jet impingement. Part 2. Free jet turbulent structure and impingement heat transfer.* Journal of Fluid Mechanics, 1971. **45**(3): p. 477-512.

122. Henderson, B., J. Bridges, and M. Wernet, *An experimental study of the oscillatory flow structure of tone-producing supersonic impinging jets.* Journal of Fluid Mechanics, 2005. **542**: p. 115-137.

123. Kalghatgi, G.T. and B.L. Hunt, *The occurrence of stagnation bubbles in supersonic jet impingement flows.* The Aeronautical Quarterly, 1976. **27**(3): p. 169-185.

124. Alvi, F.S., J.A. Ladd, and W.W. Bower, *Experimental and computational investigation of supersonic impinging jets.* AIAA Journal, 2002. **40**(4): p. 599-609.

125. Krothapalli, A., E. Rajkuperan, F. Alvi, and L. Lourenco, *Flow field and noise characteristics of a supersonic impinging jet.* Journal of Fluid Mechanics, 1999. **392**: p. 155-181.

126. Henderson, B. and A. Powell, *Experiments concerning tones produced by an axisymmetric choked jet impinging on flat plates.* Journal of Sound and Vibration, 1993. **168**(2): p. 307-326.

127. Henderson, B., *The connection between sound production and jet structure of the supersonic impinging jet.* The Journal of the Acoustical Society of America, 2002. **111**(2): p. 735-747.

128. Lim, H.D., T.H. New, R. Mariani, and Y.D. Cui, *Effects of bevelled nozzles on standoff shocks in supersonic impinging jets.* Aerospace Science and Technology, 2019. **94**: p. 105371.

129. Gummer, J.H. and B.L. Hunt, *The impingement of a uniform, axisymmetric, supersonic jet on a perpendicular flat plate.* The Aeronautical Quarterly, 1971. **22**(4): p. 403-420.

130. Carling, J.C. and B.L. Hunt, *The near wall jet of a normally impinging, uniform, axisymmetric, supersonic jet.* Journal of Fluid Mechanics, 1974. **66**(1): p. 159-176.

131. Semiletenko, B. and V. Uskov, *Empirical formulas for locating shock waves in a jet impinging on a barrier at right angles.* Journal of Engineering Physics, 1972. **23**(3): p. 1122-1126.

132. Liu, T., A. Merat, M. Makhmalbaf, C. Fajardo, and P. Merati, *Comparison between optical flow and cross-correlation methods for extraction of velocity fields from particle images.* Experiments in Fluids, 2015. **56**(8): p. 1-23.

133. Thielicke, W. and E. Stamhuis, *PIVlab–towards user-friendly, affordable and accurate digital particle image velocimetry in MATLAB.* Journal of Open Research Software, 2014. **2**(1).

134. Suter, D. *Motion estimation and vector splines*. in *Computer Vision and Pattern Recognition, 1994. Proceedings CVPR'94., 1994 IEEE Computer Society Conference on*. 1994. IEEE.

135. Thurow, B.S., N. Jiang, J.-H. Kim, W. Lempert, and M. Samimy, *Issues with measurements of the convective velocity of large-scale structures in the compressible shear layer of a free jet.* Physics of Fluids (1994-present), 2008. **20**(6): p. 066101.

136. Suzuki, T. and S.K. Lele, *Shock leakage through an unsteady vortex-laden mixing layer: application to jet screech.* Journal of Fluid Mechanics, 2003. **490**: p. 139-167.

137. Raman, G., *Cessation of screech in underexpanded jets.* Journal of Fluid Mechanics, 1997. **336**: p. 69-90.

138. Norum, T., *Screech suppression in supersonic jets.* AIAA Journal, 1983. **21**(2): p. 235-240.

139. Tam, C.K., H. Shen, and G. Raman, *Screech tones of supersonic jets from bevelled rectangular nozzles.* AIAA Journal, 1997. **35**(7): p. 1119-1125.

140. Viswanathan, K. and M. Czech, *Adaptation of the beveled nozzle for high-speed jet noise reduction.* AIAA Journal, 2011. **49**(5): p. 932-944.

141. Viswanathan, K., *Nozzle shaping for reduction of jet noise from single jets.* AIAA Journal, 2005. **43**(5): p. 1008-1022.

142. Callender, B., E.J. Gutmark, and S. Martens, *Far-field acoustic investigation into chevron nozzle mechanisms and trends.* AIAA Journal, 2005. **43**(1): p. 87-95.

143. Burak, M.O., B. Gustafsson, B. Malla, and E.J. Gutmark. *Screech noise characterization using dynamic mode decomposition and shadowgraph imagery*. in *22nd AIAA/CEAS Aeroacoustics Conference*. 2016.

144. Berry, M.G., A.S. Magstadt, M.Y. Ali, C.J. Ruscher, M.N. Glauser, and S.P. Gogineni. *Time-resolved schlieren POD and aft deck pressure correlations on complex supersonic jet nozzles*. in *55th AIAA Aerospace Sciences Meeting*. 2017.

145. Berry, M.G., A.S. Magstadt, and M.N. Glauser, *Application of POD on time-resolved schlieren in supersonic multi-stream rectangular jets.* Physics of Fluids, 2017. **29**(2): p. 020706.

146. Jaunet, V., E. Collin, and J. Delville, *POD-Galerkin advection model for convective flow: application to a flapping rectangular supersonic jet.* Experiments in Fluids, 2016. **57**(5): p. 84.

147. Edgington-Mitchell, D.M., O. Amili, D.R. Honnery, and J. Soria. *Measuring shear layer growth rates in aeroacoustically forced axisymmetric supersonic jets*. in *21st AIAA/CEAS Aeroacoustics Conference*. 2015.

148. Tam, C.K., *Dimensional analysis of jet noise data.* AIAA journal, 2006. **44**(3): p. 512-522.

149. Wei, X.F., R. Mariani, L.P. Chua, H.D. Lim, Z.B. Lu, Y.D. Cui, and T.H. New, *Mitigation of under-expanded supersonic jet noise through stepped nozzles.* Journal of Sound and Vibration, 2019. **459**: p. 114875.

Appendix

A1. Time-series schlieren images

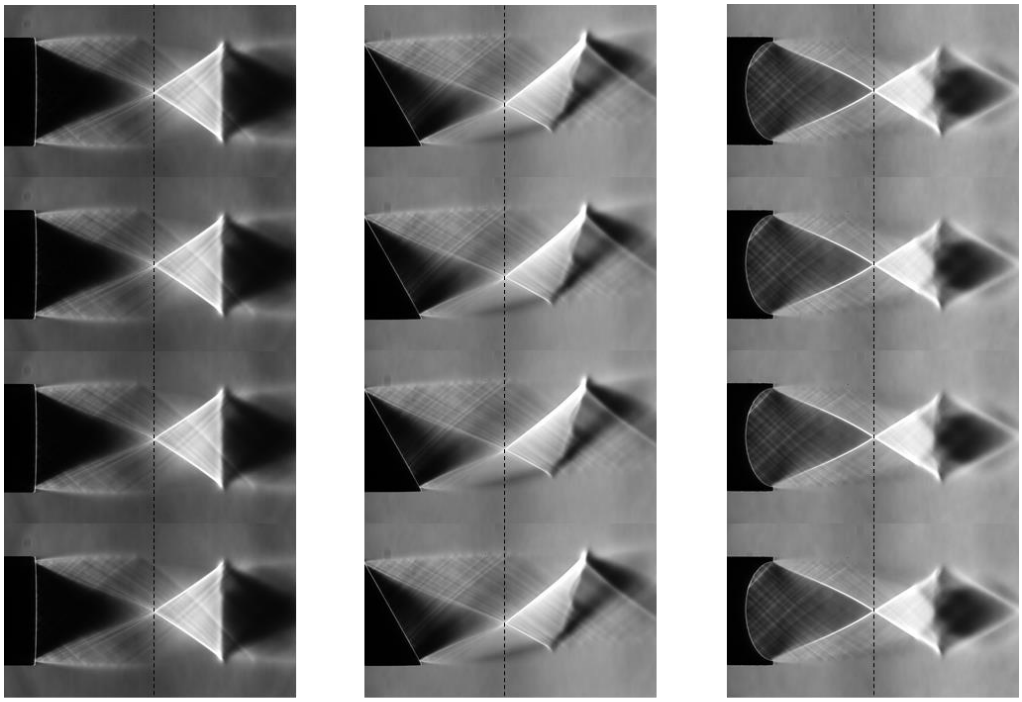

A1.1: Time-series of schlieren images captured at 1000 FPS and image exposure time of over 400 μs for the (a) baseline, (b) bevelled and (c) double-bevelled jet at NPR=5.

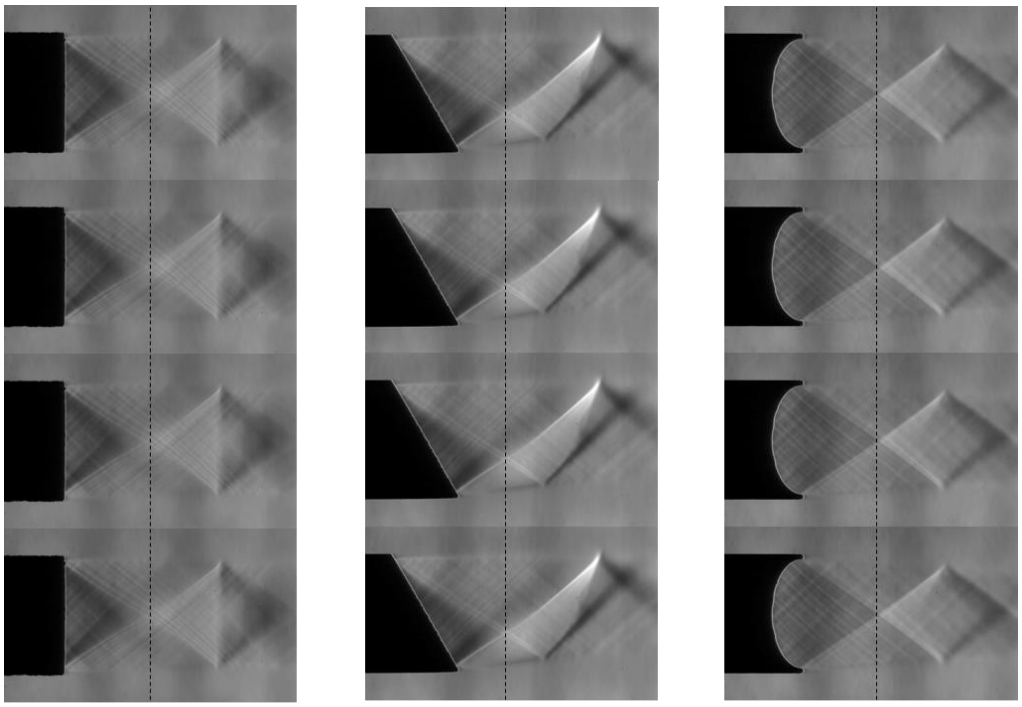

(a) (b) (c)

A1.2: Time-series of schlieren images captured at 1000 FPS and image exposure time of over 400 μs for the (a) baseline, (b) bevelled and (c) double-bevelled jet at NPR=4. Note that the brightness of these images has been enhanced.

A2. Pseudo-code of in-house optical flow algorithm

- Pre-process images with structure-texture decomposition
- Build image pyramids with image smoothing and sub-sampling
- From quadratic to fully robust penalty function (GNC) do
    - From coarsest to finest image pyramid resolution do
        - for ii=1:warping_iterations
            - Warp images using uv estimate and bi-cubic interpolation.
            - Compute image derivatives (I_x, I_y, I_t).
            - $\widetilde{uv} = uv,\ duv = 0$
            - for jj=1:linearization_iterations
                - Alternate minimize (du, dv), ξ and ζ.
                    - IRLS 1 – solve (du, dv) and z_D
                    - IRLS 2 – solve ξ and z_ξ
                    - IRLS 3 – solve ζ and z_ζ
                - Update duv
            - end
            - Update $uv = \widetilde{uv} + duv$
        - end
        - uv = up-sample(uv);
    - end
- end